ABSTRACT

Title of dissertation: Synchronization of High-Dimensional
                           Dynamical Systems

                           Elizabeth Anne Rogers, Doctor of Philosophy, 2005

Dissertation directed by: Professor Rajarshi Roy
                           Department of Physics

There are many examples of high-dimensional systems in nature. Often these systems behave in synchrony even though they possess a large number of degrees of freedom. Far fewer of these types of systems exist in the laboratory, and even fewer techniques exist with which to analyze them. As experimental capability increases, and more high-dimensional laboratory systems are fabricated, universal tools must be developed to observe and analyze the dynamics of these systems. This thesis will present experiments and analysis of two high-dimensional systems, coupled fiber ring lasers and a liquid crystal spatial light modulator with optoelectronic feedback.

Two identically constructed mutually coupled erbium doped fiber ring lasers were studied and were found to synchronize at very low coupling strengths. Synchronization error was characterized as a function of coupling strength. Optical frequency-locking and hopping as a result of the mutual coupling was also observed. Methods for detecting the leader and follower laser as well as role switching, a form of spontaneous symmetry-breaking, were developed. These include a spatiotemporal representation of the intensities within each ring laser and the use of Karhunen-Loeve decomposition. A delay-differential equation model was developed and the numerical simulations were in agreement with the experiment. Chaotic communication was achieved in this system with bit rates of 125

MHz, limited by the detection speed.

A liquid crystal spatial light modulator (SLM) was also studied. When used as a dynamic holographic grating, this device allowed the fabrication of a variety of reshaped laser beams, including multiple Gaussian beams, optical billiards, and propagating Bessel beams. When configured in an optoelectronic feedback loop, the SLM displays spatiotemporal chaos and using the auxiliary system method, we have achieved generalized synchronization of this system. The space-time patterns as well as the transients to synchronization have been characterized as a function of the bias voltage across the liquid crystal. The analysis techniques used in this thesis can be applied to other high-dimensional systems.

Synchronization of High-Dimensional
Dynamical Systems

by

Elizabeth Anne Rogers

Dissertation submitted to the Faculty of the Graduate School of the
University of Maryland, College Park in partial fulfillment
of the requirements for the degree of
Doctor of Philosophy
2005

Advisory Commmittee:

Professor Rajarshi Roy, Chair/Advisor
Professor J. Robert Dorfman
Professor Wendell T. Hill, III
Professor Daniel P. Lathrop
Professor Edward Ott

to my bf d_0, m & d, and d & j xoxo

ACKNOWLEDGMENTS

I owe many thanks to all of the people who have helped to make my graduate school experience one of the most special times of my life. First, I would like to thank my thesis advisor, Professor Rajarshi Roy, for being my mentor over the last 4 years. I could never have hoped to find a better person to guide me on this journey. In addition, I am grateful for the help of Jordi Garcia-Ojalvo on the model and understanding the dynamics of the ring laser. I would also like to thank my thesis committee, Professor Dan Lathrop, Professor Edward Ott, Professor Wendell T. Hill, III, and Professor Bob Dorfman for all of their help and advice along the way. I would also like to thank Professor Wolfgang Losert for including me in some of his experiments.

I owe a tremendous debt of gratitude to my labmates and collaborators over the last four years, Dave DeShazer, Ryan McAllister, Bhaskar Kubchandani, Christian Silva, Wing-Shun Lam, Min-Young Kim, Will Ray, Tony Franz, and Atsushi Uchida from our lab, Narapuron Chattrapiban (Tor) and David Coffield from Dr. Hill's Lab, and Matt Fergusun from Dr. Losert's lab. I have learned an enormous amount from each of them and I thank them for all of their help on all of my experiments as well as their friendship. Our collaborators in the ABLE group, specifically Dr. Ira Schwartz, Dr. Leah Chock, and Dr. Joan Aron, have been very helpful both in my work in physics and in the daunting task of figuring out what to do next year. I have really enjoyed working with them and look forward to continued collaborations. I would also like to thank my summer students Rita Kalra and Adam Cohen for all of their hard work over the summers. I owe a great

deal of thanks to the rest of the IREAP staff for their invaluable help, especially Don Martin for his technical assistance, Ed Condon for all of his computer help and water, Dottie Brosius for her help with LaTex and Jane Hessing in the Physics department for all of her help over the last 4 years.

An extra special thanks is owed to the members and honorary members of the Mechanics Pirates Cove, Santiago, D_0, Nick, Chad, Patrick, Manolis, Dan', Guido, and Mike. YARRRRRR!!!!! I would like to thank the members of Dan Lathrop's group for providing excellent lunch company and the members of Dr. Losert's group for hawaiian shirt day and teaching me how to play texas hold'em.

I would like to thank my Mom and Dad for being so wonderful and for teaching me that there is no greater thing in life than an education, and also that 2 and 2 is 22. I thank my brothers, Danny and Jonny, for "Keeping it real" and not letting me take graduate school or myself too seriously, and my puppies, Ricky and Lucy, for never letting me forget what's really imporant in life, playing bally and frisbee on the beach.

Lastly, I would like to thank my best friend and soon to be husband, Dan Dakin, for his friendship and help along the way, and espcially for reading this entire thesis. He has made my graduate school experience extra special.

TABLE OF CONTENTS

LIST OF TABLES

LIST OF FIGURES

Chapter 1

Introduction

1.1   High-Dimensional Chaotic Systems

Nature provides us with many complex systems that have a large number of degrees of freedom, or, in other words, are high-dimensional. Examples of these systems are biological, as in the dynamics of neural networks, or physical as in turbulent flows in rivers and the atmosphere. Often these systems do not lend themselves to the type of quantitative study that we are accustomed to in physics. It is difficult to observe all of the degrees of freedom of these high-dimensional systems and therefore to develop adequate analysis tools and models.

These difficulties exist in laboratory experiments with many degrees of freedom, as well. While there are plenty of examples of high-dimensional laboratory systems, there are not many universal analysis techniques. Turbulent flows is a popular area of study in high-dimensional nonlinear systems, and many analysis techniques have been developed specifically for these experiments[1]. Networks of oscillators is a popular technique used to understand high-dimensional systems[2, 3], however connecting more than a few oscillators proves to be difficult both experimentally and numerically[3]. Multimode laser systems in optoelectronic feedback loops and doped fiber optic ring lasers also exhibit high-dimensional dynamics[4, 5].

As our observational tools and data recording devices become more capable, it is now possible to obtain long data sets encompassing many different time scales in these high-dimensional experiments. This adds another layer to the data analysis problem. This

problem is inherent in doped fiber ring lasers, which fluctuate on multiple time scales. Due to their long length, the intracavity intensity dynamics of ring lasers can be resolved by a photodetector, and oscilloscopes can record data over a long period of time. Therefore, the cavity periodicity, short time scale fluctuations, and an additional coupling periodicity appear in a single data set making it difficult to analyze using traditional chaotic analysis techniques.

High-dimensional dynamical systems can display various types of synchronization, depending on the type of coupling, the coupling strength and the number of degrees of freedom that can be coupled between the systems. For example, it is often easier to achieve identical synchronization in systems with many degrees of freedom using mutual coupling than it is through unidirectional coupling. This is the case in coupled erbium doped fiber ring lasers. However, this leads to the question of which system is leading the dynamics and which system is following them. While statistical measures are being developed for this purpose[67], this thesis will explore several other methods for determining leader and follower in mutually coupled laser dynamics.

Liquid crystals provide a means for studying spatially extended high-dimensional dynamical systems. In this system it is impossible to record and feed back all of the degrees of freedom. This system does not display identical synchronization, but displays generalized synchronization. We will present a characterization of the spatiotemporal chaos displayed by a liquid crystal spatial light modulator and the generalized synchronization that it displays.

It is important to develop tools with which to study high-dimensional dynamical systems because most systems that occur naturally have many degrees of freedom. Controllable laboratory experiments with many degrees of freedom are vital to the develop-
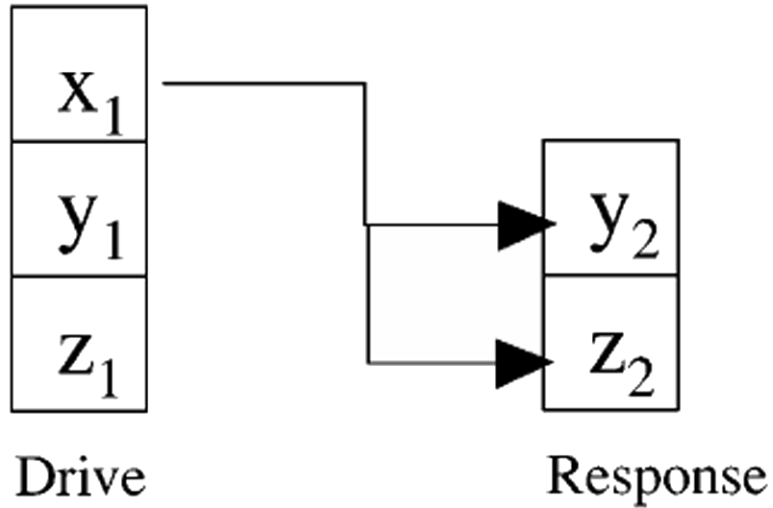
Figure 1.1: Synchronization scheme, where the drive synchronizes to the response[11].

ment of these tools. These techniques have wide ranging applications from the modeling of neurons and disease spread[2] to the eventual control of swarming sensors[6].

One way to control high-dimensional dynamical systems is through synchronization. By studying how systems synchronize and the type of synchronization that can be achieved with different systems, we can learn which degrees of freedom are important for control of the system. Once these are determined, algorithms for computationally feasible models may be developed based on what is learned from the synchronization experiments[7].

1.2 Synchronization

Pikovsky, Rosenblum and Kurths describe synchronization as "an adjustment of rhythms of oscillating objects due to a weak interaction."[8] Synchronized systems do not have to be chaotic. In fact, one of the first documented cases of synchronization was in the pendula of clocks[8], which are certainly not chaotic. The idea of synchronization of chaos is somewhat counterintuitive. Chaotic dynamics depend very sensitively on the initial conditions[9, 10] and they should not be able to be controlled by another chaotic system. Throughout

$$y(t) = F(x(t))$$
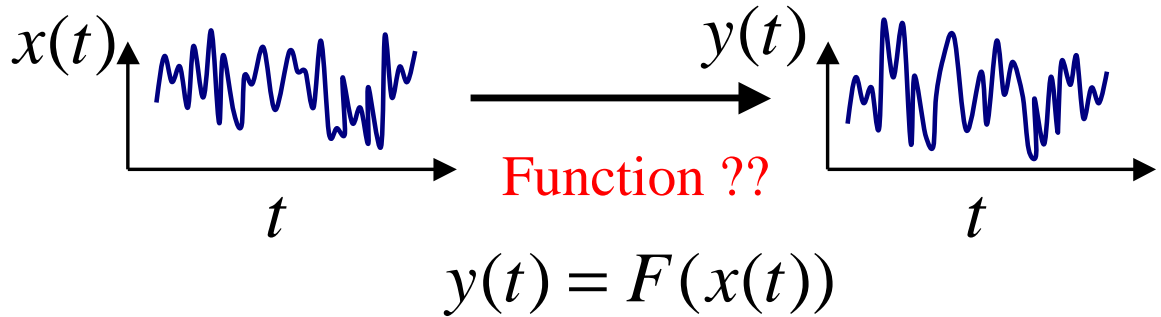
Figure 1.2: Schematic for generalized synchronization where there is a functional relationship between the drive and response signals[15].

the 1980's to 1990, several groups predicted the ability of two identical chaotic systems to synchronize their dynamics[12, 13, 14]. Pecora and Carroll showed numerically that if the chaotic output from a sufficient number of degrees of freedom replace some of the degrees of freedom in a second, identical, system, the two systems may display similar chaotic dynamics[14]. This methodology is shown in Fig. 1.1. Since 1990, various other schemes for synchronization have been developed and many are outlined in Ref. [11] and experimental examples of synchronization of chaos have been plentiful.

Depending on the number of degrees of freedom in the two systems and the number of degrees of freedom that can be coupled between the systems, it is possible to achieve different kinds of synchronization. The easiest type of synchronization to detect is **identical** synchronization, as presented in Ref. [14]. Two time series are identically synchronized if they display similar chaotic outputs at the same time. It is also possible to obtain **phase** synchronization, where the phase of the chaotic signals are synchronized[9], or **lag** synchronization, where the chaotic dynamics are synchronized with a time offset. The final type of synchronization that will be considered is **generalized** synchronization, where there exists a functional relationship between the drive and response signal, as outlined in Fig. 1.2[8, 9].
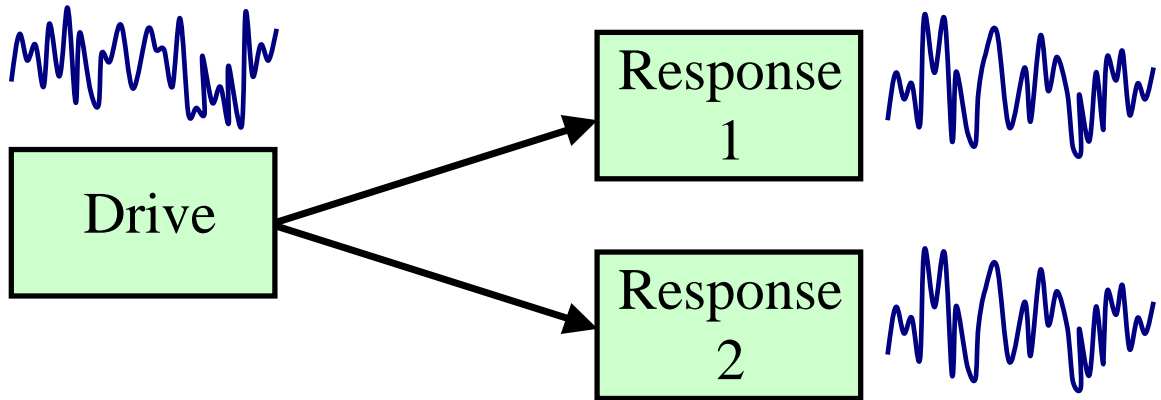
Figure 1.3: Schematic for generalized synchronization detected using the auxiliary method. Note that the drive signal is not synchronized to the response but that the response signals are synchronized to each other[15].

Generalized synchronization may be the most difficult type of synchronization to detect because the drive and response signals do not look the same. There are however, several ways to identify generalized synchronization. One way is to find the functional relationship between the drive and response signal, which is often difficult for experimental systems. Another way is through the auxiliary method for detection which offers a more useful experimental alternative. In this method, outlined in Fig. 1.3, two identical response systems are constructed and driven by the drive system. If the two response systems display identical dynamics after transients, it is concluded that the drive and response system are generally synchronized[16, 17, 18, 19].

1.3 Coupling Schemes

Often the type of synchronization that is achieved depends on the coupling scheme. Experiments on synchronization most often involve unidirectional coupling because it may be useful for chaotic communications[20]. In this configuration, there is a drive system that forces the receiver system to follow its dynamics. Cuomo and Oppenheim proposed that

synchronized chaotic waveforms could be used as a carrier for communications[20]. Since the carrier is chaotic, the signals cannot be intercepted and decoded without a system that is identical to the one that created the original carrier. This application has led to many types of laser chaos synchronization schemes in which unidirectional coupling was employed.

Though unidirectional coupling is the most popular way to achieve synchronization of chaos, mutual coupling may provide an easier way to synchronize. With mutual coupling, systems with many degrees of freedom influence each other, allowing them to operate in a state different from the state of the two isolated systems. This allows the threshold coupling strength for synchronization to be lower than it would be with unidirectional coupling and the synchronization to be robust against perturbations. It also allows high-dimensional systems that may not synchronize with unidirectional coupling to achieve identical synchronization.

1.4   Analysis Techniques

Since synchronization has traditionally been demonstrated in low-dimensional systems, the analysis techniques have been focused there as well[21]. However, these tools are not adequate for determining some properties of coupled high-dimensional chaotic systems. As an example, consider the coupled fiber laser system that will be described in this thesis. In this system there are over 15,000 longitudinal modes propagating in each laser cavity. Standard measurement techniques allow us to measure the overall intensity output of the laser, but does not allow us to resolve the intensity outputs of each individual mode. When two lasers are mutually coupled, the question of which modes are most influential in the synchronization of the dynamics is not easily answerable using established methods. This

is, however, an important fundamental question. Knowing which modes synchronize first (or at lower coupling strengths) and how many have to be synchronized before we see synchronization of the overall intensity patterns could help to develop methods for the control of chaos in complex biological systems and large networks.

1.5 Organization of Thesis

This thesis addresses the phenomena of synchronization of high-dimensional chaotic systems through the exploration of coupled systems with many degrees of freedom. We also develop tools with which to analyze these systems, ultimately providing new ways to understand and control high-dimensional dynamical systems. In the next three chapters, we will explore the background on and applications of the experimental systems that create high-dimensional dynamics. The following four chapters discuss a fiber ring laser experiment, new methods for analyzing this type of high-dimensional experiment, and a possible application of this system. Chapter 9 will describe a controllable spatiotemporal chaotic system and the types of synchronization that it displays. Finally the last chapter will present a conclusion and discussion of future work.

Chapter 2

Solutions to Maxwell's Equations; Laser Modes and Bessel Beams

This thesis will approach high dimensional dynamics through the study of lasers. There-fore, it is instructive to understand some background on lasers and the form of the emitted electromagnetic radiation. A typical laser cavity consists of an active medium between two spherical mirrors. The active medium can be a semiconductor where the radiation comes from excited electrons, a gas of ions where the light is emitted by excited ions, or a solid state crystal where excited ions emit light but are trapped in the crystal. A few guides on basic types of lasers and the theory behind their operation can be found in Ref. [22, 23]. In all of these types of lasers, two spherical mirrors keep the emitted light within the cavity so that it can be amplified by stimulated emission from the active medium. Generally one of the mirrors has a considerably smaller reflectivity so that some of the light can leave the cavity, and this is the light we observe as laser radiation. Typically the aperture and the transverse cavity dimensions are small compared to cavity dimension along the direction of propagation, which is very important in determining the shape of the electromagnetic wave that propagates from the cavity.

2.1 Maxwell's Equations and Fundamental Laser Modes

Classically, electromagnetic waves are described by the wave equation, derived from Maxwell's Equations, which is (in the absence of free charges and currents) [24]:

$$\nabla^2 \mathbf{E} - \mu\epsilon \frac{\partial \mathbf{E}}{\partial t} = 0, \tag{2.1}$$

where $\epsilon = \epsilon_0 * \epsilon_r$ and $\mu = \mu_0 * \mu_r$, and μ_r and ϵ_r are the magnetic permeability and dielectric constant in the medium. The wavenumber is defined as $k = \omega\sqrt{\epsilon\mu}$ and in an absorbing or amplifying medium, the gain obeys the equation, $\epsilon_r = 1 + \chi\prime(\omega) - i\chi\prime\prime(\omega)$ [25].

We now look for solutions to the wave equation for the electric field. The most well known solution to the wave equation is a plane wave, $\mathbf{E}(\mathbf{r}, t) = \exp[i(\mathbf{k} \cdot \mathbf{r} - \omega t)]\hat{e}$. Plane waves, however, only exist when the source of the electromagnetic wave has an infinite aperture. The electromagnetic radiation reaching the earth from the sun is approximated by a plane wave. Obviously, this approximation will not work for laser beams.

To describe laser radiation, we must look for an approximate solution to Eq.(7.2) that obeys the spherical mirror boundary conditions, that is localized around the direction of propagation and varies slowly with time in the direction of propagation. Therefore, we look for solutions of the form

$$\mathbf{E}_0 = E(x, y, z) \exp(i(\omega t - \mathbf{k}(r) \cdot \mathbf{r}))\hat{e}, \tag{2.2}$$

where the wavenumber, $\mathbf{k}$ is a function of $\mathbf{r}$. If we plug Eq.(2.2) into E1.(7.2) we find that

$$\nabla^2 E(x, y, z) + \mathbf{k}^2(\mathbf{r})E(x, y, z) = 0, \tag{2.3}$$

which is called the Helmholtz equation. We must find the appropriate expression for $E(x, y, z)$ so that Eq.(2.2) satisfies all of the laser boundary conditions. We assume a solution of the form $E(x, y, z) = \psi(x, y, z)e^{-ikz}$ where the intensity, $\psi^2(x, y, z)$, is localized around the direction of propagation, the z direction in this case. If we substitute the expression for E into Eq.(2.3), we find a new expression

$$\frac{\partial^2 \psi}{\partial x^2} + \frac{\partial^2 \psi}{\partial y^2} + \frac{\partial^2 \psi}{\partial z^2} - 2ik\frac{\partial \psi}{\partial z} = 0. \tag{2.4}$$

The condition that the field varies slowly along the direction of propagation, otherwise known as the paraxial approximation, allows us to set $\frac{\partial^2 \psi}{\partial z^2}$ equal to zero. So the equation
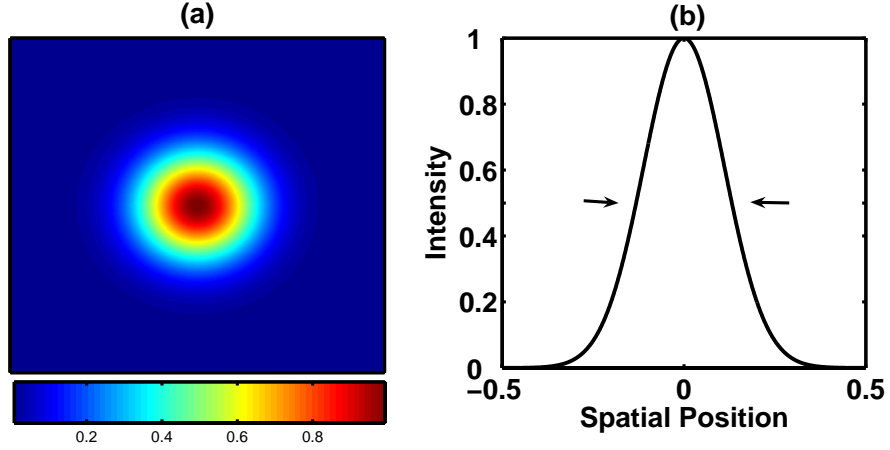
Figure 2.1: Gaussian profile. (a) is a two dimensional Gaussian profile. (b) is a slice from the center of (a). The arrows indicate the $1/e^2$ point.

becomes

$$\frac{\partial^2 \psi}{\partial x^2} + \frac{\partial^2 \psi}{\partial y^2} - 2ik\frac{\partial \psi}{\partial z} = 0 \tag{2.5}$$

We assume a solution of the form

$$\psi(x, y, z) = \exp[-i(P(z) + \frac{k}{2q(z)}r^2)] \tag{2.6}$$

where $r^2 = x^2 + y^2$. This solution produces the Gaussian intensity profiles that most lasers emit. In order for this to satisfy Eq.(2.5), we find that

$$\frac{dq}{dz} = 1 \quad \text{and} \tag{2.7}$$

$$\frac{dP}{dz} = \frac{i}{q(z)}. \tag{2.8}$$

In this representation, $P(z)$ is called the phase shift factor and $q(z)$ is called the beam parameter. Since these are not observable parameters, would like to relate them to the physical observables $R(z)$ and $w(z)$. $w(z)$ is the spot size, or the distance from the propagation axis at the point z where the intensity has fallen to $1/e^2$ of its peak value on

10

axis, as shown in Fig. 2.1. $R(z)$ is the radius of curvature of the phase front at the point z. The beam parameter is related to $R(z)$ and $w(z)$ through

$$\frac{1}{q} = \frac{1}{R} - \frac{i\lambda}{w^2\pi}. \tag{2.9}$$

If we call w_0 the minimum spot size, we can show that

$$w^2(z) = w_0^2[1 + (\frac{\lambda z}{\pi w_0^2})^2], \text{ and } R(z) = z[1 + (\frac{\pi w_0^2}{\lambda z})^2] \tag{2.10}$$

With these relationships, we can derive the expression

$$E(r, z) = \frac{w_0}{w} \exp[-i(kz - \Phi) - r^2(\frac{1}{w^2} - \frac{ik}{2R})]. \tag{2.11}$$

This equation represents the full spatial dependence of the Gaussian beam, where $\Phi = \tan^{-1}(\lambda z/\pi w_0^2)$. A complete derivation can be found in Ref. [25]. The solution derived above is the zero order mode and is called the fundamental, or TEM$_{00}$ Gaussian mode. The surfaces of constant phase are Gaussian, and this is the mode normally seen emitted by the laser.

2.2 Higher Order Modes

The higher order modes present in the resonator depend on the symmetry of the cavity. Cylindrically symmetric cavities can support modes called a Laguerre-Gaussian modes. In order to derive the higher order mode equation, we need to assume a more general solution for the spatial field distribution amplitude, $\psi(x, y, z)$. In this case we propose a solution of the form

$$\psi = g(\frac{r}{w}) \exp[-i(P(z) + \frac{k}{2q(z)}r^2 + l\phi)], \tag{2.12}$$

where

$$g = (\sqrt{2}\frac{r}{w})^l \cdot L_p^l(2\frac{r^2}{w^2}) \tag{2.13}$$

11
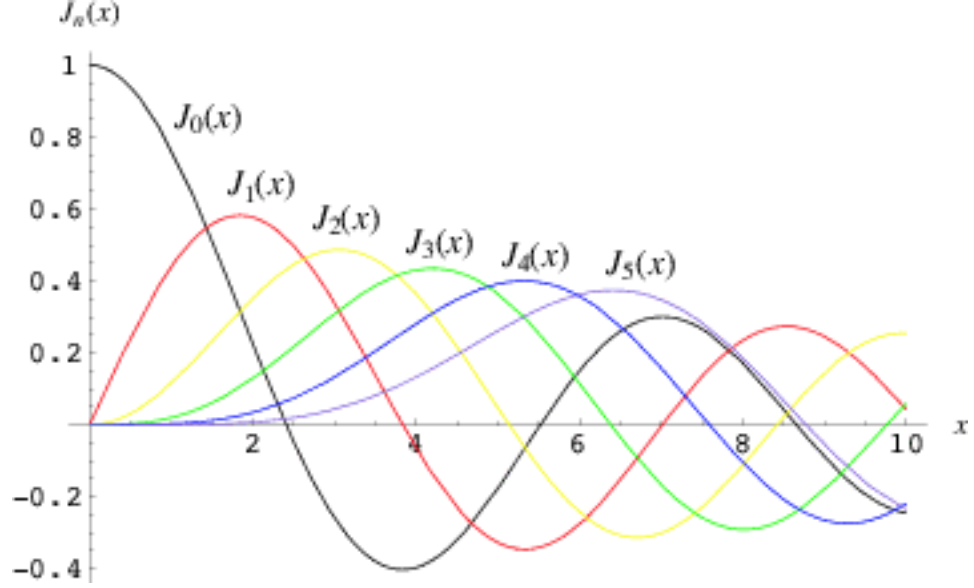
Figure 2.2: Bessel functions of order n.

and L_p^l is an associated Laguerre polynomial. These modes are designated as TEM$_{pl}$. For the $l = p = 0$ case $L_0^0 = 1$ and we recover the Gaussian mode derived in the previous section, hence the designation as the TEM$_{00}$ mode. The $l, p = 0, 1$ mode, or the TEM$_{01}$ mode, is frequently called a donut mode because it propagates with a dark spot in the center, which diffracts as the beam propagates [25].

2.3   Another Solution to Maxwell's Equations; Bessel Beams

A second solution to Maxwell's Equations was discovered in the late 1980's by J. Durnin [26]. It is his derivation we will follow here. We again begin with the wave equation, Eq.(7.2) and we assume a propagating wave solution of the form

$$E(x, y, z \geq 0) = \exp[i(\beta z - wt)] \int_0^{2\pi} A(\phi) \exp[i\alpha(x \cos \phi + y \sin \phi)]d\phi, \qquad (2.14)$$

where $\alpha^2 + \beta^2 = (w/c)^2$ and $A(\phi)$ is an arbitrary complex function. If β is real, then we can show that the solution is nondiffracting, meaning that the intensity does not depend

12

on the distance of propagation, z. If $A(\phi)$ is independent of ϕ, then Eq.(2.14) becomes

$$E(\mathbf{r}, t) = \exp[i(\beta z - wt)] \int_0^{2\pi} \exp[i\alpha(x\cos\phi + y\sin\phi)]\frac{d\phi}{2\pi} = \exp[i(\beta z - wt)]J_0(\alpha\rho), \quad (2.15)$$

where $\rho^2 = x^2 + y^2$ and J_0 is the zero order Bessel function of the first kind [26]. If $\alpha = 0$ the solution is a plane wave, but for $0 < \alpha \leq \frac{w}{c}$, the solution is a nondiffracting zero order Bessel function. If we assume that $A(\phi) = \exp(in\phi)$, Eq.(2.15) becomes

$$E(\mathbf{r}, t) = \exp[i(\beta z - wt)]J_n(\alpha\rho), \quad (2.16)$$

and now includes all orders of Bessel functions [27]. An illustration of Bessel functions can be found in Fig. 2.2.

2.4 Bessel Beams and Holography

Like the plane wave solution described in section 2.1, Durnin's Bessel beam solution to Maxwell's equations assumes an infinite aperture. In 1989, Vasara *et al.* derived the same solution using similar approximations as were made in the derivation of the Gaussian beam and describe the effects of finite apertures on the solution. This is very important because any laboratory fabrication of Gaussian beams require the use of finite apertures. Vasara *et al.* derives the finite aperture assuming Bessel beam generation through holography [27]. If we have a hologram of radius R, characterized by the complex amplitude function

$$t(\rho, \phi) = A(\phi)\exp[i(\frac{2\pi\rho}{\rho_0})] \quad \rho \leq R \quad (2.17)$$

$$t(\rho, \phi) = 0 \quad \rho > R \quad (2.18)$$

where $A(\phi)$ is the same complex function as in Eq.(2.14) and the parameter α from Eq.(2.15) equals $(2\pi)/(\rho_0)$. Using the assumption that $A(\phi) = \exp(in\phi)$, the complex amplitude function within the aperture as described in Eq.(2.18) becomes

$$t(\rho, \phi) = \exp[i(n\phi + \alpha\rho)]. \quad (2.19)$$

13

We can see the effect of a finite aperture by looking at the intensity of the field after the aperture. The field distribution for the hologram can be calculated using the Fresnel diffraction integral in spherical coordinates

$$U(\rho, \phi, z) = \frac{1}{i\lambda z} \exp[ik(z + \frac{\rho^2}{2z})] \times \int_0^D d\rho' \rho' \exp[ik(\frac{\rho'^2}{2z} - \frac{2\pi\rho'}{\gamma})]$$
$$\times \int_0^{2\pi} d\phi' A(\phi') \exp[-ik\rho\rho' cos(\phi - \phi')/z] \qquad (2.20)$$

where the wavelength, $\lambda = (2\pi)/(k)$ and $\gamma = \rho_0 k$. Following the procedure outlined in Refs. [27, 28], we integrate over $d\phi'$ by first expanding $A(\phi')$ into its Fourier series,

$$A(\phi') = \sum_{n=-\infty}^{\infty} a_n \exp(in\phi) \qquad (2.21)$$

and inserting it into Eq.(2.20), which then becomes

$$U(\rho, \phi, z) = \frac{1}{i\lambda z} \exp[ik(z + \frac{\rho^2}{2z})] \sum_{n=-\infty}^{\infty} a_n \exp(in\phi) \times \int_0^D d\rho' f_n(\rho') \exp[ik\mu(\rho')] \qquad (2.22)$$

where, $a_n = \frac{1}{2\pi} \int_0^{2\pi} A(\phi') \exp(-in\phi') d\phi'$ are the normal Fourier coefficients and

$$f_n(\rho') = 2\pi(-i)^n \rho' J_n(\frac{k\rho\rho'}{z}), \qquad (2.23)$$

$$\mu(\rho') = \frac{\rho'^2}{2z} - \frac{2\pi\rho'}{\gamma}. \qquad (2.24)$$

We look for the critical points of Eq.(2.24), and find a single critical point at $\rho'_c = (2\pi z)/(\gamma)$. From Refs. [27, 28], we know that

$$\int_0^D d\rho' f_n(\rho') \exp[ik\mu(\rho')] \propto \frac{f_n(\rho'_c) \exp[ik\mu(\rho_c)]}{[k\mu''(\rho'_c)]^{\frac{1}{2}}}. \qquad (2.25)$$

Using the critical point calculated above, we see that the right side of Eq.(2.25) is now equal to

$$\frac{4\pi^2 \frac{z}{\gamma}(-i)^n J_n(\frac{2\pi k\rho}{\gamma}) \exp[\frac{-2\pi^2 ikz}{\gamma^2}]}{(\frac{k}{z})^{1/2}} \qquad (2.26)$$

14

which is proportional to $z^{3/2}$. If we combine the results from Eqs.(2.26 and 2.22), and take the square of the magnitude, we obtain an expression for the intensity. Without position independent constant, this expression is of the form

$$I(\rho, \phi, z) \propto z \left| \sum_{n=-\infty}^{\infty} 2\pi(-i)^n a_n \exp(in\phi) J_n(\frac{2\pi k\rho}{\gamma}) \right|^2. \tag{2.27}$$

If we look at the result in Cartesian coordinates it is,

$$I(x, y, z) \propto z \mid U(x, y) \mid^2, \tag{2.28}$$

which shows that the only effect of the finite aperture is a z dependence of the intensity. We can then calculate the maximum diffraction-free propagation distance for the Bessel beam by finding the z value when the critical point is the boundary of the aperture, of radius, R. In this case [27],

$$z_{\text{max}} = \frac{\gamma R}{2\pi} = \frac{\rho_0 R}{\lambda}. \tag{2.29}$$

Therefore, how sharply the beam diffracts at the maximum propagation distance is dependent on the linewidth of the light used. If the linewidth is very narrow, the diffraction occurs very quickly, and once the maximum propagation distance is reach, the Bessel beam dissapears.

We have derived the intensity profiles of the beams emitted by the lasers in the first half of this dissertation, which generate single longitudinal and transverse mode Gaussian profiles within the cavities. We then use holography to change the profile of the beams into new field distributions, both diffracting and nondiffracting.

The second half of this thesis will focus on a laser system in which the laser cavity is extremely long compared to the size of the transverse dimensions. In this situation the laser still generates light with a Gaussian profile, however, due to the long cavity

length, it generates tens of thousands of longitudinal modes, each propagating in a different

polarization state.

Chapter 3

Liquid Crystal Spatial Light Modulators

Nematic liquid crystals have recently infiltrated many aspects of our every day lives. Their presence in displays on clocks, cellular phones, computer monitors and now high-definition televisions leaves one to wonder at how life existed without them. Liquid crystals have been in use in the scientific community far longer than in the commercial world. Liquid Crystal Light Valves (LCLV's) were first created by Hughes Aircraft Company in the late 1970's[29]. These LCLV's were used in the development of the Liquid Crystal Displays (LCDs) listed above, as well as the development of a holographic tool for use in the physical and biological sciences. Due to their nonlinear optical properties, liquid crystals act as a controllable dynamic hologram and have thus become an invaluable tool in the emerging field of biophysics and in experimental atomic physics[30, 31, 32]. This chapter will present background information on the physical and optical properties of liquid crystals and describe how they are used as dynamic phase gratings.

3.1   Types of Liquid Crystals

Liquid crystals (LC's) come in three variates: **thermotropic, lyotropic** and **polymeric**. Thermotropic liquid crystals have been most extensively studied because they are observed in pure compounds and mixtures. They have phase transitions that depend on temperature [33] which are cholesteric shown in Fig.3.1, smectic shown in Fig 3.2, and nematic shown in Fig. 3.3. LCLV's can be composed of an LC in either the **nematic** or smectic-C* phase, also called a **ferroelectric** liquid crystal. Smectic LC molecules lie in planar layers
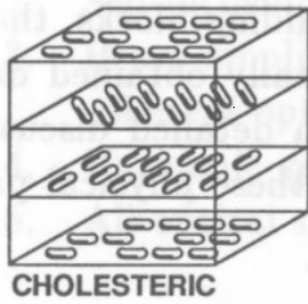
Figure 3.1: Cholesteric phase of thermotropic liquid crystals[33]
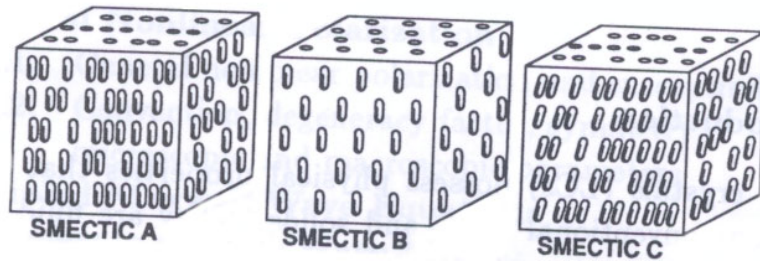
Figure 3.2: Smectic phase of thermotropic liquid crystals.[33]
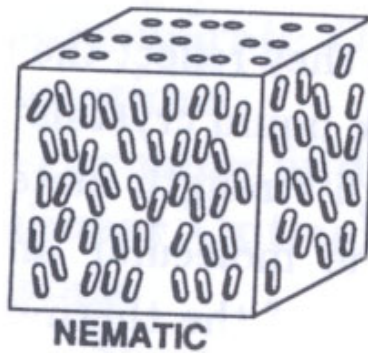
Figure 3.3: Nematic phase of thermotropic liquid crystals[33]

whereas in the nematic phase the molecules are randomly located throughout the volume of the container. In both phases the molecules are usually aligned by the manufacturer along a single symmetry axis called the director. The director orientation is sensitive to local or global external electric, magnetic or optical fields, and is responsible for the index of refraction of the crystal. Therefore, the director reorientation can result in local phase and/or polarization changes of an incident optical beam [33]. For a complete discussion of the properties of the other types of liquid crystals see Ref. [29, 33]. The main difference between ferroelectric and nematic liquid crystals is the molecular dipole response to voltage. The molecules in both types of LC's have a larger dielectric constant in the direction of the long axis than in the direction of the short axis. This leads to induced dipoles at opposite ends of the long axis. Therefore, applied electric fields will cause the molecules to change their orientation and align with the field. Since nematic LC's have only an induced dipole moment, an AC voltage will cause the dipole moment to change direction, and will not result in an overall change in the molecular orientation. Ferroelectric LC molecules posses a permanent dipole moment and therefore will realign depending on the parity of the voltage. It is for this reason that DC voltages must be used to drive ferroelectric liquid crystals. However, DC voltages can induce permanent dipole moments and chemical changes in nematic LC's. Therefore, since modulation in the parity of the source does not effect director alignment, AC signals are used to modulate the orientation of nematic LC's[29].

The director axis in nematic crystals can be aligned in three major ways, **parallel, perpendicular** and **twist**, in order to enhance their nonlinear optical properties. In parallel alignment, the faces of the substrates are coated with a transparent metallic film and then etched, creating microgrooves for alignment of the molecules [33]. When a

19
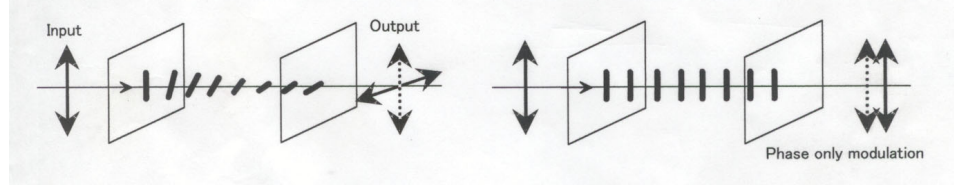
Figure 3.4: Twist and parallel arrangements of liquid crystals[34]

linearly polarized optical field comes in contact with parallel aligned liquid crystals two phenomena may occur depending on the difference between the orientation of the director and the polarization of the light. If the light is polarized parallel to the director, pure phase modulation will occur. However, if the polarization of the light is 45° to the director axis then both phase and polarization modulation occurs [33].

Perpendicular or homeotropic aligned liquid crystals have a director axis that is perpendicular to the face of the cell. Even though both parallel and perpendicular aligned LC's can be used for phase modulation and retardation, there are a few differences in the properties of the crystals and the way they are prepared. Most importantly, whereas simple surface etching is all that is required to align the LC molecules in parallel alignment, for perpendicular alignment a surfactant is needed to keep the molecules aligned. For a complete discussion of the differences between homeotropic and parallel aligned LC's see Ref.[33].

The last type of LC alignment we will discuss is the twist alignment. In the twist alignment, the surfaces are etched as in the parallel alignment, however, the back surface is twisted with respect to the front. This alignment has the unique property to rotate the phase of the light that goes through it. If linearly polarized light is incident on 90°, the polarization axis of the light will rotate by 90° and it will remain polarized [33]. Often, when the LC is used as a reflective grating, since the light passes through twice, the angle

offset between the front and back face is only 45° as show in Fig. 3.4. The liquid crystals used in the experiments described in this thesis are parallel aligned.

Gratings or holograms are created on the liquid crystals by placing localized voltages across the molecules causing director realignment and subsequently a change in the local index of refraction. In all alignments, a threshold voltage across the LC's must be reached before director realignment can be achieved. Once the minimum bias voltage is crossed, director realignment occurs almost linearly with voltage until a damage threshold is reached. This damage threshold depends on the specific type of liquid crystal. When the orientation of the liquid crystal molecules matches the linear polarization of the incident light, this change in director orientation and resulting change in the index of refraction imparts a phase change to be on the incident optical field, creating an interference pattern with little loss in the overall intensity, similar to a glass phase hologram. If the linearly polarized light is not polarized in the same direction as the director, we see an interference pattern coupled with a change in the polarization of the light. When viewed through a polarizer, we will now see both an interference pattern and an overall loss of intensity.

3.2   Liquid Crystal Spatial Light Modulators

The dependence of the birefringence on local external electric fields makes liquid crystals a good choice for an easily controllable phase grating. This is the principle behind a liquid crystal spatial light modulator (SLM). In practice, SLM's are either optically or electrically addressable, meaning that the director axis can be modulated with either an electric voltage or an optical field. As with traditional diffraction gratings, SLM's can be either reflection or transmission holograms. In a reflection grating, the incident optical field passes through the grating, reflects off of an internal mirror and passes through the grating
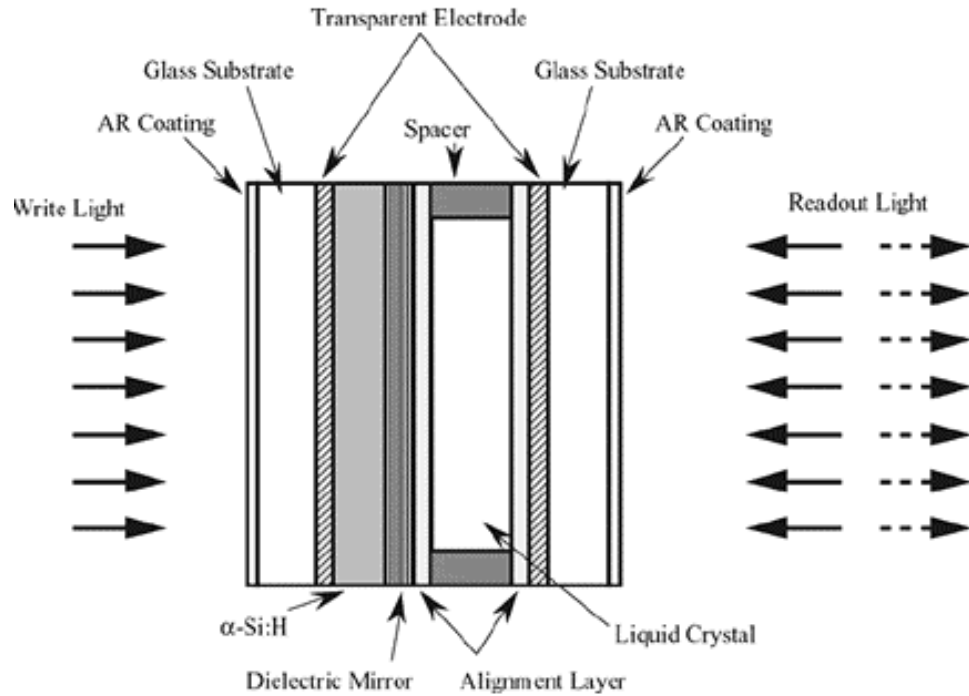
Cross section of the Hamamatsu LC-SLM

Figure 3.5: Picture of the inside of the Hamamatsu PAL-SLM X7550[34]

a second time in the opposite direction. In a transmission hologram, the light makes only one pass through the grating. Transmission hologram liquid crystals typically must have cell volumes greater than reflection gratings because the light only passes through one time. Also, depending on the orientation of the LC molecules relative to the polarization of the incident light, the hologram can act as either a phase or amplitude grating. A full discussion of the polarization and phase effects of liquid crystals can be found in Ref.[33]. All experiments presented here utilize the SLM as a reflection phase grating.

Since the LC used in the experiments described in this thesis was electrically address-able, optically addressed liquid crystals will not be discussed in detail. For a description of optically addressed LC's, see Refs. [33, 41]. In our electrically addressed SLM, the liquid crystal cell is between two transparent electrodes, as shown in Fig. 3.5. The transparent

electrodes provide the voltage across the liquid crystal that tilts the director axis of the molecules. An overall DC bias voltage is placed on the electrodes so that the voltage across the liquid crystals will exceed the threshold. The SLM is computer controlled, which allows for very precise control over the local voltages across the LC molecules. The SLM uses the video graphics array (VGA) output of the computer to make a grayscale pattern on an internal liquid crystal display which is separate from the LC that creates the hologram. An internal laser (the write light) propagates through the LCD onto an array of photoelectrodes. This is shown on the left side of Fig. 3.5. The photoelectrodes place voltages across the LC (on the right side of Fig. 3.5). Since the director reorientation is proportional to the applied voltage, the voltages place a phase grating on the LC similar to the image on the computer. Figure 3.5 illustrates the composition of our SLM. The readout light represents the optical field whose phase is modulated by the SLM. The dielectric mirror prevents interference between the read light and the write light.

3.3   The Hamamatsu PAL-SLM X7550

In the experiments described in the following chapters, a linearly polarized TEM_{00} laser, called the read light, is incident on the SLM in the configuration shown in Fig. 3.6. The desired phase mask is generated on a computer and the SLM takes the value of the red part of the red-green-blue output of the VGA port of the computer. The VGA output from the computer can send a voltage signal with 8-bit dynamic range (256 different values) for each color; therefore, the SLM can apply 256 different phase shifts to the incoming light. Our SLM has an effective area of 2.5 x 2.5 cm and each pixel is therefore $\sim 52 \mu\text{m}^2$. The bias voltage control ranges from 0-5 V, corresponding to phase shifts ranging from 0 to $\sim 4\pi$. It has an oscillation frequency of 1 KHz, but can be adjusted
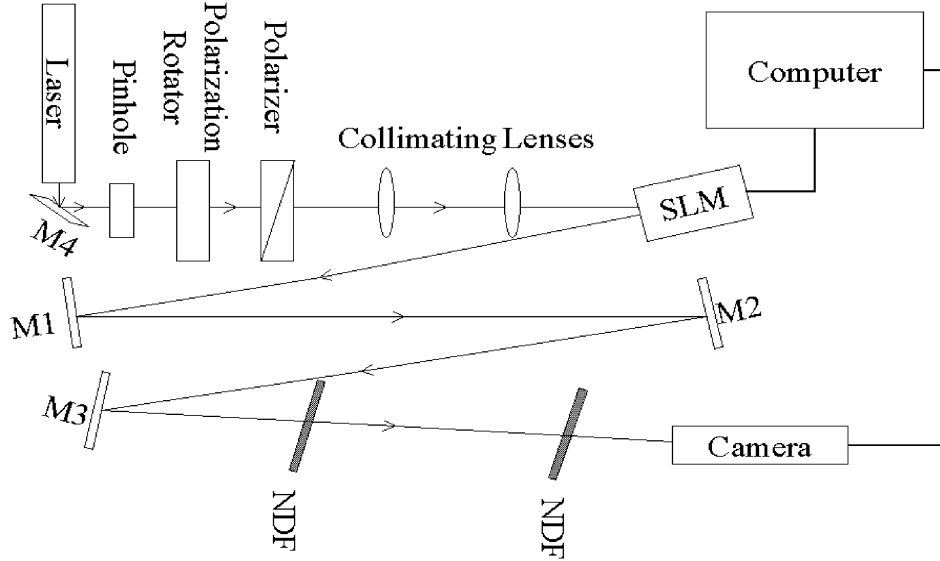
Figure 3.6: Spatial light modulator experimental setup for holography. For Fourier holograms, a lens is inserted between the SLM and the camera so that the focal point of the lens is on the camera.

between 0.83 Hz and 1 MHz. The bias voltage can also be externally modulated using the external control input terminal[34]. The VGA signal is displayed on a pixilated internal LCD, with a resolution of 480 x 480 active pixels. A write light at 533 nm propagates through the LCD and is incident on an array of photoelectrodes. These photoelectrodes are responsible for the voltage modulation across the front end LC creating the phase grating. After reflecting off of the SLM, the read light propagates to a camera through a lens for certain types of holograms. The camera is connected to the computer via a Spiricon camera board and the hologram is viewed on the computer. The camera is a Pulnix TM-72EX charged coupled device camera with 114×180 pixels.

The maximum read light intensity that can be applied to the SLM is dependant on the characteristics of the dielectric mirror that is present in the unit. For the SLM used in the experiments presented in this thesis, the dielectric mirror was broadband. This allows lasers with a wide range of wavelengths to be used with the device, however, the

reflectivity for each wavelength is lower than for a mirror made for a narrower range of wavelengths. If light leaks through the dielectric mirror, it can interfere with the write light and alter the hologram placed on the LC. A 5 W source spread over the entire active area of the SLM can safely be used without causing interference between the read and write light. However, the read light should never be focused to a small spot on the SLM because this could cause damage to the LC[35].

3.4 Applications

The use of the SLM as a dynamic hologram has led to the development of tools that have become very useful in the fields of biological and atomic physics. In biological physics, the SLM can be used to generate holographic optical tweezers[30]. Optical tweezers are a focused beam of light that can be used to trap particles[42]. Because this property works independent of wavelength, these optical tweezers can be used to trap and observe live biological samples. When holography is not used in the production of optical tweezers, a single laser can only be focused to create a single optical tweezer, and, if the trap is to move, the laser must be mechanically moved. Holographic optical tweezers have the advantage of creating multiple Gaussian beams, or optical tweezers, out of a single laser beam through diffraction. While this can be done using a glass phase hologram, it is more efficient to use an SLM because we have more control over the phase shift that is imparted on the light (i.e., more than 2 or 4 phase shift levels may be used in the SLM, while this is extremely difficult in an etched glass hologram). Using a computer controlled SLM allows the optical tweezers to move and change with real time control[30, 43, 44]. In addition to trapping particles with Gaussian beams, particles can be trapped in higher order Laguerre-Gauss modes. These modes have been holographically generated using

glass phase masks[45] as well as using an SLM for biological applications[30].

The generation of multiple Gaussian beams from a single Gaussian beam has applications to atomic physics as well. Recently, holographic traps for single atoms have been demonstrated[31]. These traps offer the same flexibility that holographic tweezers offer, only in atomic physics they must trap much smaller particles. The fabrication of nondiffracting Bessel beams also have applications to atomic physics. For example, these beams can be used to make an all light atom guide, as described in Ref.[32]. The method for generating these beams will be discussed in detail in Chapter 4.

3.5 Chaos and Liquid Crystals

SLM's configured in feedback loops generate a variety of spatiotemporal patterns ranging from hexagonal close packed (HCP) dot structures to so called optical turbulence and chaos[36, 37, 38, 39, 40]. This behavior is caused by nonlinearities in the crystal-electric field interaction or induced by rotations and other transformations as the signal is fed back into the system. Which patterns form depend on the voltages placed across the liquid crystal, the intensity of the write light, and the diffraction length[37]. Our liquid crystal system has a fixed, high intensity write light and generates chaos at the lowest resolvable bias voltage. In order to model this type of feedback system, the SLM is approximated as a Kerr type nonlinearity, although the Kerr slice approach fails to account for the dynamic chaos that can be induced in the liquid crystal[37]. Models that also include saturation and internal threshold effects better agree with experimental observations[38]. A detailed description of the model is presented in Ref.[37].

Once chaos was identified in liquid crystals, systems were constructed to test for synchronization. Identical synchronization has been seen in liquid crystal SLM systems

with optical feedback[41]. In these experiments, the write light intensity was relatively low, causing the patterns generated to be closer to HCP with defects than optical turbulence. This means that the liquid crystal molecules are not subjected to strong voltages and are not forced to reorient themselves greatly[37]. However, in systems such as ours where the write light intensity is strong enough to always produce optical turbulence, the liquid crystals are being forced to reorient themselves at a rate that does not allow them to find a steady state. Therefore, we do not expect to reproduce these results.

Chaotic liquid crystals in a SLM provide a controllable means to develop analysis tools for high-dimensional dynamics because they are controllable. The pixel-by-pixel control allowed by the SLM, gives one the ability to control the movement of the liquid crystal molecules and the connections between them. It is, therefore, possible to create a network using the pixels that control the liquid crystal molecules. These networks could be made to vary over time and space. This would create a laboratory system in which control would be had over the high-dimensional dynamics, large parameter regions could be explored, and analysis tools could be developed. This thesis provides the first step in these types of experiments by characterizing the chaos and then looking for synchronization of chaos when chaotic intensity patterns are recorded and fed back into the SLM system.

Chapter 4

Bessel Beams and Holography

The SLM is a wonderful tool with which to develop holographic techniques for the control of small particles. Holographic optical tweezers are now widely used in biophysical applications because one can trap living cells or microbeads surrounding living cells and study how they move[46]. Another area of development in which the SLM has been particularly useful is in beam reshaping for use in atom optics, both as holograms in a plane and as reshaped propagating beams.

4.1 Holography

4.1.1 Algorithms for Generating Holograms

Many methods have been devised for computer generated holography. Using traditional hologram fabrication techniques, creating phase gratings with more than four different phase shift levels is very difficult. With computer aided holography and the SLM, one can create phase gratings with up to 256 different phase shifts. The desired image can be drawn on the computer and, using one of many different types of algorithms, a grating with which to make the image can be calculated. Ref.[47] has a good description of many of these algorithms. One such type of computer generated hologram is the kinoform[29]. A kinoform is a grating in which it is assumed that the majority of the information about an intensity pattern is carried in the phase of the Fourier coefficients. However, when generating a hologram from an image on a computer, all we know is the intensity. Therefore, we need a way to reconstruct the phase knowing only the intensity. The
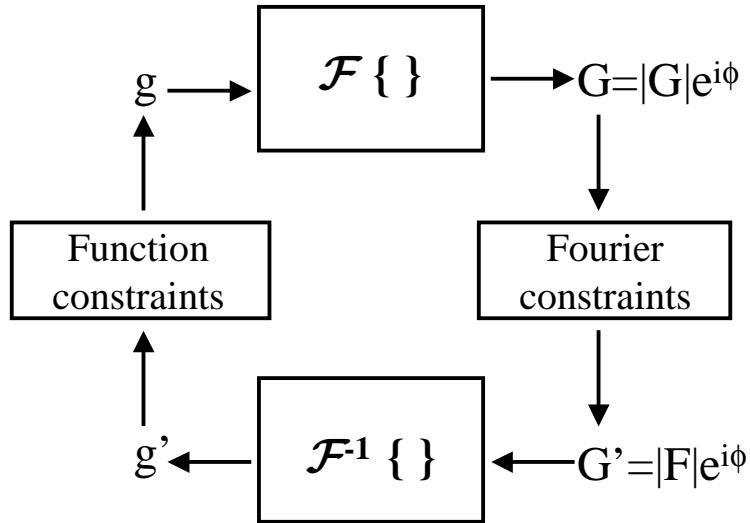
Figure 4.1: Diagram of the Gerchberg-Saxton algorithm. The iteration begins in the upper left corner with the original intensity and a random phase and continues until the resulting image matches the desired image within the requisite error.

Gerchberg-Saxton algorithm for phase reconstruction was developed for the purpose of reconstructing the phases of images when we only know the intensity. It is illustrated in Fig. 4.1. We begin with a known two-dimensional intensity image, $f(x)$, and calculate the two-dimensional discrete Fourier transform (DFT) of the image, whose modulus is $F(u)$. We then construct a function

$$g_k(x) = \mid f(x) \mid \exp[i\theta_k(x)] \tag{4.1}$$

where in the first iteration $(k = 1)$ the phase is random. We then take the DFT of $g_k(x)$ to obtain

$$G_k(u) = \mid G_k(u) \mid \exp[i\phi_k(u)]. \tag{4.2}$$
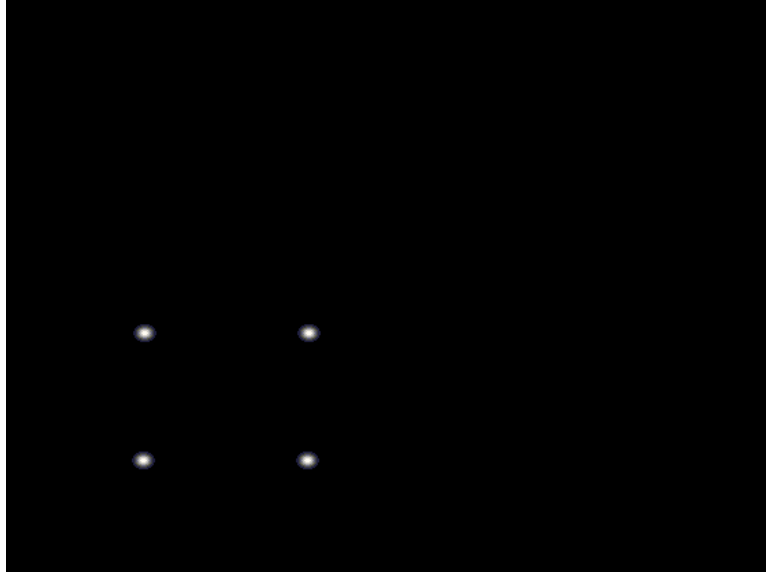
Figure 4.2: The desired intensity pattern, an image of four small Gaussian spots, that is fed into the G-S algorithm to produce a kinoform.

The next step is to replace the modulus of the $G_k(u)$ with the modulus of the DFT of the desired image to yield

$$G'_k =\mid F(u) \mid \exp[i\phi_k(u)]. \tag{4.3}$$

We then take the inverse DFT and obtain a new expression for the field in real space,

$$g'_k(x) =\mid g'_k(x) \mid \exp[i\theta'_k], \tag{4.4}$$

and finally we replace the calculated intensity $\mid g'_k(x) \mid$, with the desired intensity $\mid f(x) \mid$ to obtain an updated expression for g_{k+1},

$$g_{k+1} =\mid f(x) \mid \exp[i\theta_{k+1}]. \tag{4.5}$$

This process is iterated until it achieves a minimum error between the desired image and the calculated image.

In order to generate the phase grating, we begin by creating an image of the final intensity pattern that we would like in the beam. Figure 4.2 shows an image of four
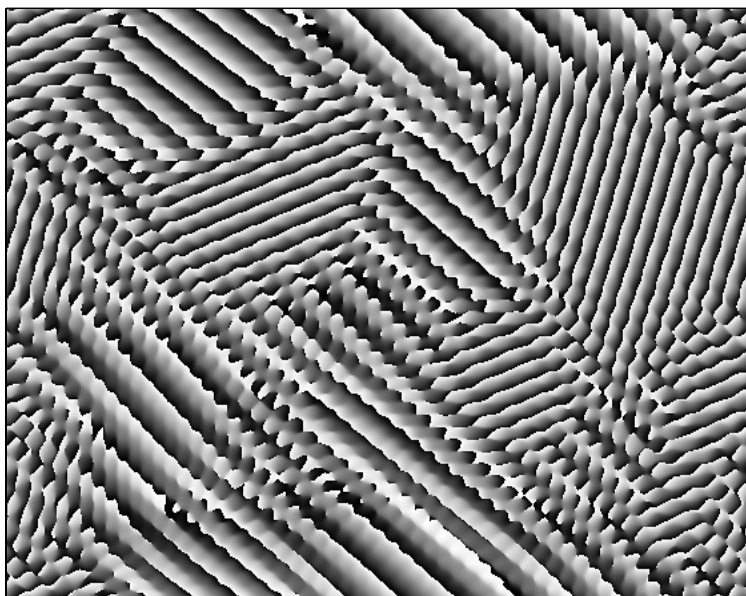
Figure 4.3: A sample kinoform that produces the four small Gaussian spots in a square as shown in Fig. 4.2.

Gaussian spots. From this picture, we calculate the phase using the Gerchberg-Saxton algorithm to calculate the phase angles in real space. We then image the Fourier space phase angles on the computer, as shown in Fig.4.3. This image can either be printed onto a transparency, as an amplitude grating, or placed on the SLM. If it is placed on the SLM it can be made into a purely phase hologram with up to 256 different phase shifts[29, 47, 48].

Since we are creating a hologram using the Fourier phase, the resulting image will only be visible in the Fourier, or far field, plane. This plane is accessible in the laboratory at the focal point of a lens. Therefore, a lens must be inserted after the SLM in the experimental setup in order to view the holographic image created by the kinoform.
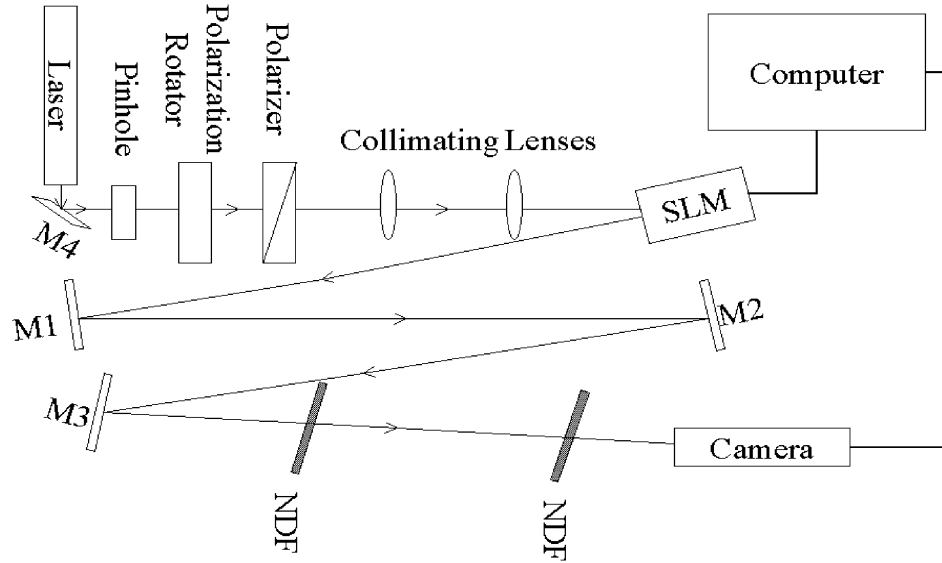
Figure 4.4: Spatial light modulator experimental setup for holography. For Fourier holograms, a lens is inserted between the SLM and the camera so that the focal point of the lens is on the camera.

4.1.2   Multiple Beams

We have created several types of phase-modulated beams using the experimental setup in Fig.4.4. This setup is described in detail in Chapter 2. In their most simple form, the optical tweezers that we have created are multiple Gaussian spots generated from a single Gaussian laser beam. Fig. 4.5 shows arrays of 4, 16, and 32 Gaussian spots generated from a single Gaussian beam. The physical size of the final spots is controlled by the spot size at the focal point of the lens.

The vertical and horizontal symmetry of a square lattice allows the hologram and the inverse hologram to overlay, thus increasing the overall intensity of each spot. It is also possible to obtain equi-intensity Gaussian spots in the shape of a triangle, even though the symmetry does not allow the hologram and the inverse hologram to overlap.

The final holograms, shown in Fig. 4.6, are laser beams reshaped as holographic billiards. These billiards are in the shape of a stadium and a circle and have a step

(a)
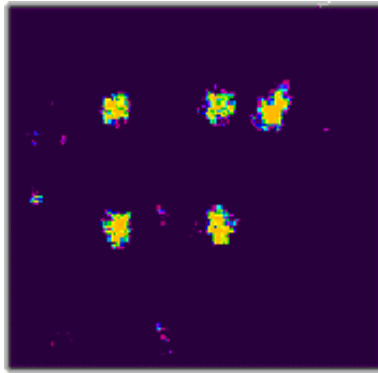
(b)
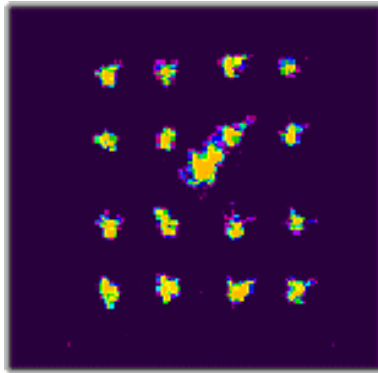
(c)
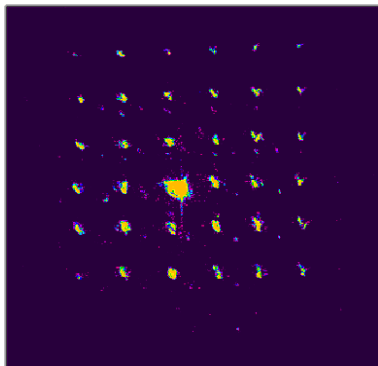
Figure 4.5: Multiple Gaussian beams generated from a single Gaussian. (a) is 4 Gaussian beams with a bright first order diffraction spot on the right side. These are generated from the hologram imaged in Fig.4.3. (b) is 16 and (c) shows 32 equal intensity Gaussian spots generated using the same method.

33
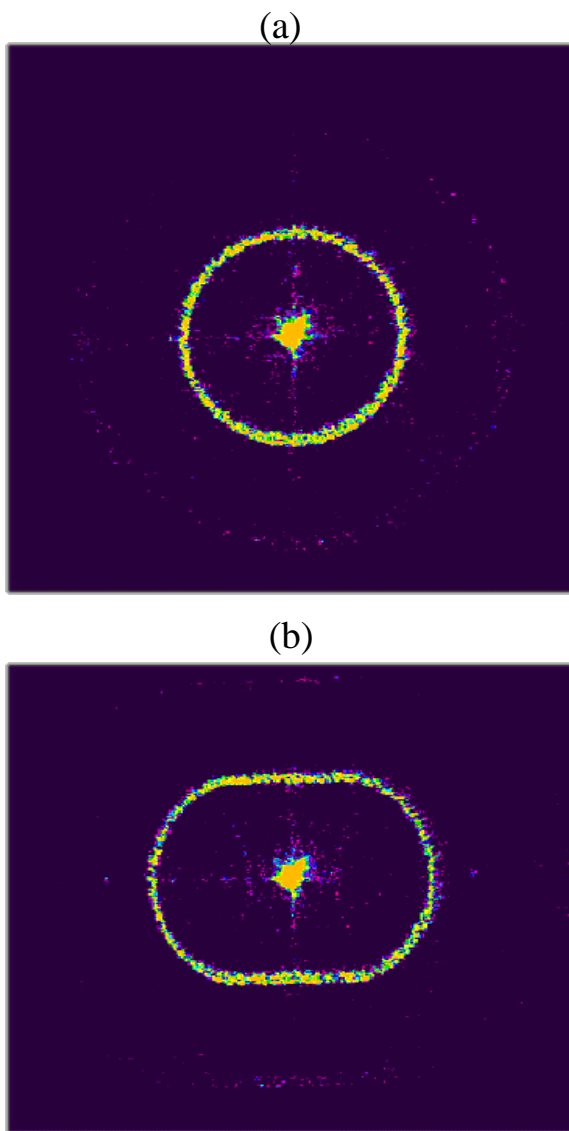
Figure 4.6: (a) Circle and (b) Stadium billiard holograms with a step function intensity profile.

function intensity profile. If a neutral particle is placed in the dark region inside of the billiard with momentum in any direction, the particle will trace all possible paths within the billiard, thus behaving chaoticly.

The center spot in the middle of each hologram is the zero order diffraction beam. In perfect phase holograms the zero order should not be present and all of the light should be diffracted into the first order, reshaped beam. In practice, all of the light is not modulated to form the holographic image and the light that is not diffracted is focused by the lens into a center spot. One reason for this is that the phase shifts do not run equally between 0 and 2π in our experiment. If we knew the exact relationship between the red color level and the phase shift imparted by the LC onto the light, then an algorithm can be written to eliminate the center spot[49].

4.2 Propagating Bessel Beams

4.2.1 Bessel Beam Holograms

In addition to Fourier holograms, we are also able to fabricate holograms that turn Gaussian beams into propagating Bessel beams. According to equation 2.19, the phase of the transmission function is

$$\Psi(\rho, \phi) = n\phi + \frac{2\pi\rho}{\rho_0}, \tag{4.6}$$

where the phase profile resembles that of an axicon (or is cone shaped). The dark center of the Bessel beam is a result of a singularity in the phase at the tip of the axicon, the size of which is controlled by the parameter ρ_0. As the value of ρ_0 increases, the size of the dark core increases as well. In Eq.(4.6), n represents the charge of the Bessel beam and is proportional to the amount of angular momentum around the singularity (it is sometimes referred to as the winding number of the singularity). The intensity profiles of the Bessel
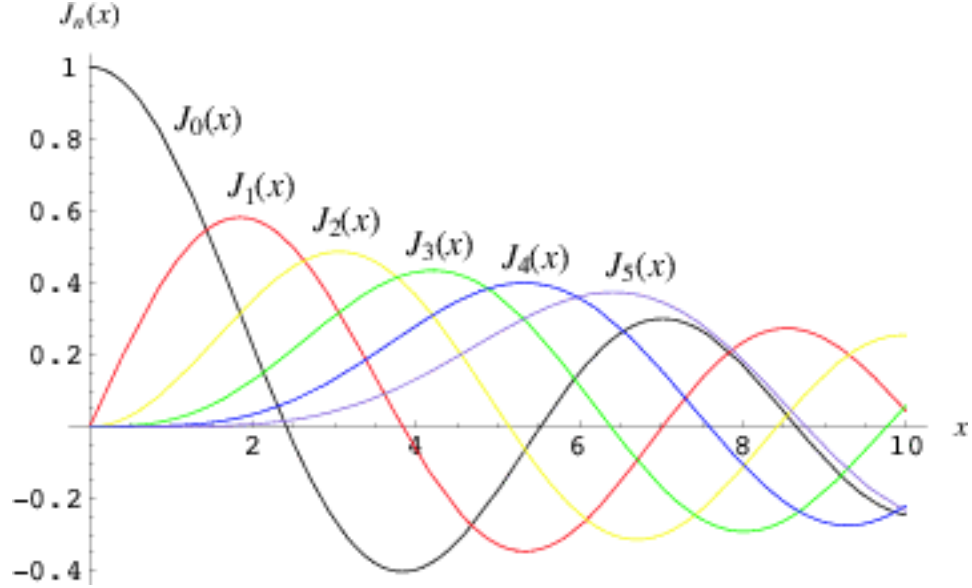
Figure 4.7: Order n Bessel Functions

beams reflect the shape of the 3-dimensional Bessel functions of similar charge.

Figure 4.7 shows a few different orders of Bessel functions while Fig. 4.8 shows typical gratings and the Bessel beams they create. In the hologram, the charge is defined by a closed counterclockwise contour on the phase mask and is equal to the number of net phase discontinuities it crosses[51]. We define the sign of the discontinuity to be positive when the phase jumps from 2π to 0 and negative when the phase jumps from 0 to 2π. By this definition, the charge of the phase masks in Fig. 4.8 and the rest of this thesis is equal to $+2$ and we vary ρ_0.

4.2.2   Parameters and Bessel Beams

The Bessel beams shown in this thesis were generated using the experimental setup described in figure 4.4. The holograms were generated on the computer using Matlab and the phase images were placed on the SLM as described in Section 5.1. One of the advantages of using the SLM to produce these beams is that we are able to generate many

36
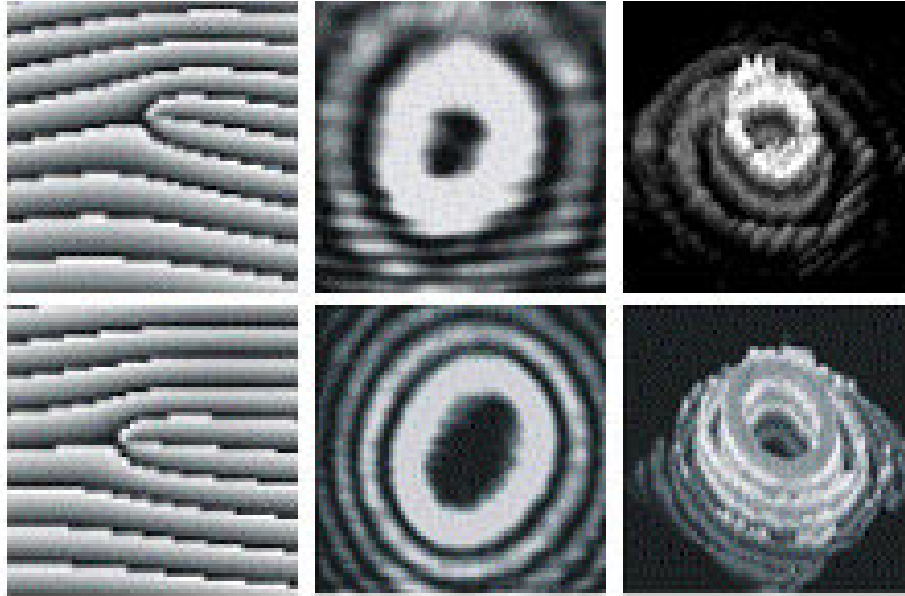
Figure 4.8: The phase masks used to produce two different sizes of the dark core of a Bessel beam using a Bessel function of the first kind of order $n = 2$. The first column consists of the actual phase masks that are generated on the computer and placed on the SLM. The parameter is $\rho_0 = 1.4$ mm for the top, notice the larger amount of deviation from horizontal of the fork at the center of the mask due to the smaller magnitude of ρ_0. This results in a smaller hole. The parameter for the bottom is $\rho_0 = 3.2$ mm resulting in a smaller deflection from horizontal for the singularity of the grating, causing a larger hole. The middle column is a 2-dimensional picture of the Bessel beam generated from the gratings to their left, where the intensity is represented by brightness. The column on the far right is a 3-dimensional image of the hollow beam, where both brightness and height represent intensity.[50]
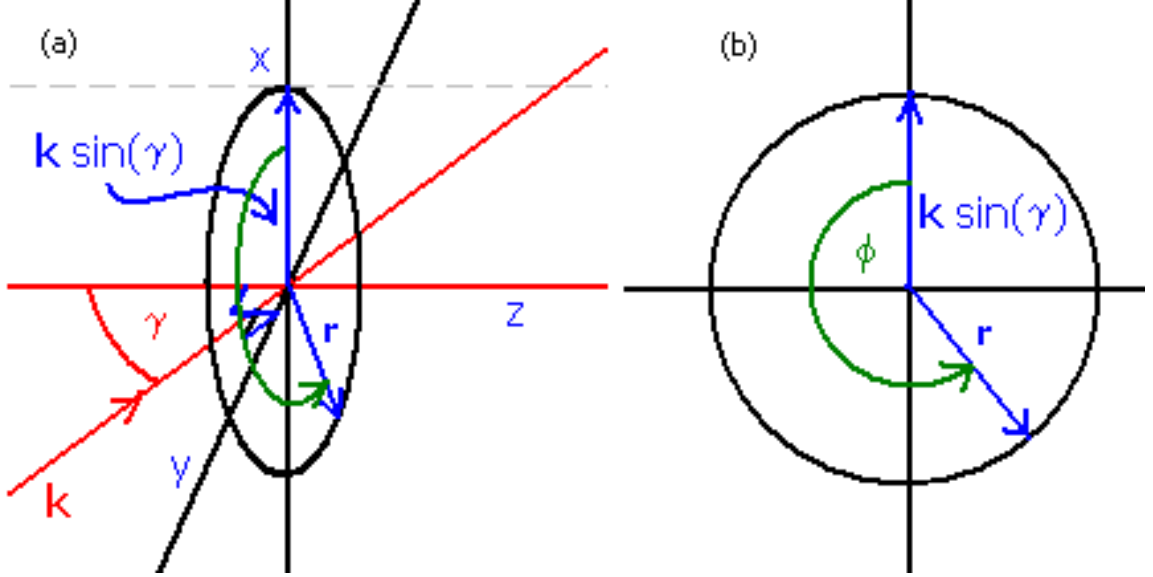
Figure 4.9: Deflection angle diagram. z is the propagation direction. γ is the angle between the reference beam and the line normal to the surface of the SLM.

different holograms and test many different parameter values relatively quickly. We tested approximately 50 different values of ρ_0 ranging from $\rho_0 = 0.1 - 5.0$ mm in steps of 0.1 mm corresponding to core sizes ranging from $1 - 3$ mm. Two different core sizes are shown in Fig. 4.8. In the top row, $\rho_0 = 1.4$ mm while in the bottom row, $\rho_0 = 3.2$ mm. The resolution of each mask was 500×500 pixels for all experiments presented here.

If we take the projection of the read laser beam at an angle to the surface of the SLM onto the normal to the surface of the SLM as shown in Fig. 4.9, we can define a parameter that controls the deflection angle of the read beam after going through the hologram. This addition to the phase term looks like,

$$\mathbf{k} \cdot \mathbf{r} = \frac{2\pi}{\lambda} \rho \sin\gamma \cos\phi = 2\pi\nu\rho\cos\phi \tag{4.7}$$

where $\mathbf{k}$ is the wave number of the read beam, γ is the angle between the reference beam and the line normal to the surface of the SLM, and $\nu = (\sin\gamma)/\lambda$ is the carrier frequency. The $\cos\phi$ term comes from the inner product of $\mathbf{k}$ and $\mathbf{r}$ projected onto the plane of the

grating. In the experiments presented here, $\lambda = 633$ nm. The deflection angle is found to be a linear function of ν. In all experiments described to this point, $\nu = 4.5$ mm^{-1}.

As stated in Chapter 2, the SLM allows us the flexibility to test different phase shift levels. We coded phase profiles between $0 - 2\pi$ with 2, 4, 64 and 256 grayscale levels. Figure 4.10 shows the difference in the intensity profiles of Bessel beams generated with 2 levels (0 and π), and one with 64 different equally spaced levels. The advantage of the 64 level hologram is evident by the Bessel function fit in this figure. The intensity of the first ring of the Bessel beam for the 64 level grating is almost an order of magnitude higher than the first ring of the Bessel beam using a binary mask. The integrated power in the first ring of the 64 level mask is 12.4 times that of the first ring in the binary mask. The full phase profile is now

$$\Psi(\rho, \phi) = (\alpha\rho + n\phi + 2\pi\nu\rho\cos\phi) \bmod 2\pi. \tag{4.8}$$

The bias voltage control of the liquid crystals allows us to control the amount of light in the different orders produced by the grating. The measurements presented herein were made at a bias voltage of approximately 1.88 V, corresponding to approximately a 1.70π phase shift. Figure 4.11 is a photograph of the Bessel beam produced by two different levels of bias voltage. On the left, the bias is not optimized, and we get a significant amount of light in the zero order diffraction beam. This picture was taken at a bias voltage of 1.47 V. On the right, the bias voltage is optimized, at 1.88 V, and almost all of the power is in the first order diffracted beam, while only a small amount remains in the zero order. Therefore, we see that at 0 V, only the zero order beam is seen because no phase shift is being imparted onto the read laser beam. Between 0 and 1.88 V, the power is split between the zero and first order diffracted beams, and as the voltage is increased, more power is transferred into the first order. At 1.88 V the power diffracted into the first
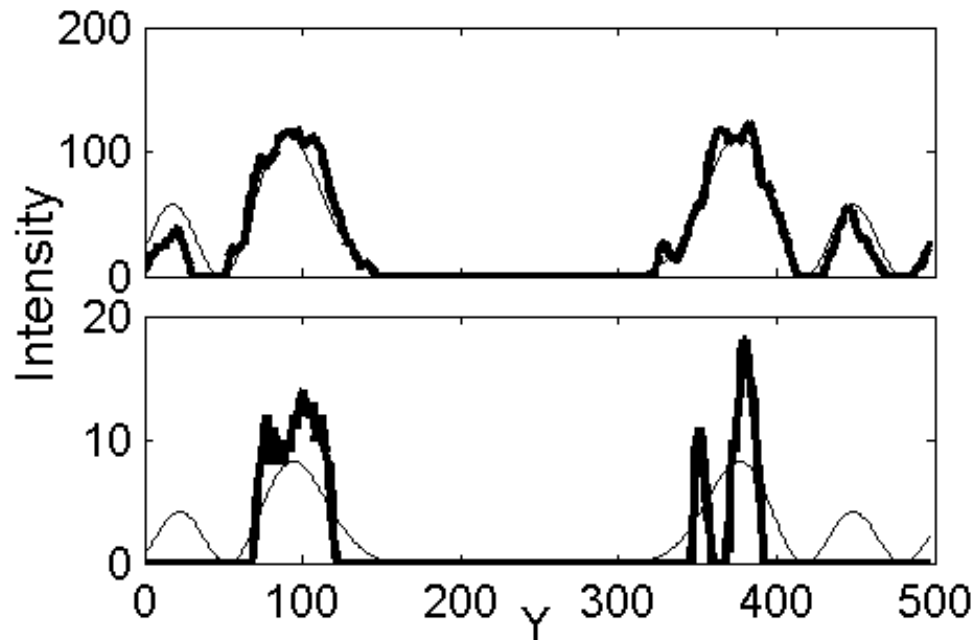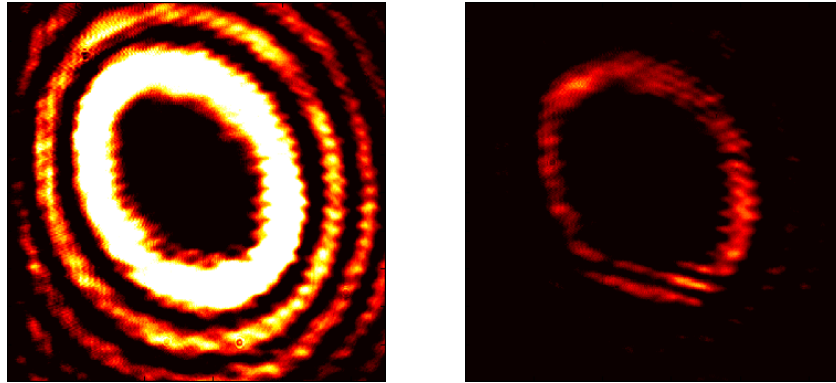
Figure 4.10: A comparison between two nonlinear fits of the Bessel beam (J_7) profiles. The top profile was generated from a 64 level phase grating while the bottom profile was generated using a binary phase grating. The ratio of the power in the first ring obtained from the 64 level grating compared to the binary grating is 12.4. The experimental profiles are denoted by the thick line while the Bessel function fit is denoted by the thin line and the amplitudes of both profiles are in similar units. The scale of the y-axis from 0 to 500 is equal to the length of the CCD on the camera used to take the profile. The same neutral density filter was used for both profiles to eliminate the saturation on the CCD camera.[50]
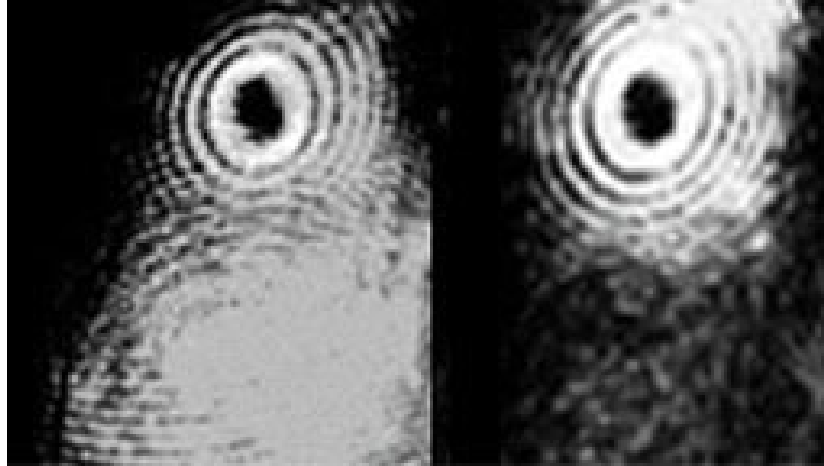
Figure 4.11: Controlling the amount of light by adjusting the bias voltage. On the left, at a bias voltage of 1.47 V, the bias is not optimized, and we get a significant amount of light in the zero order diffraction beam. On the right, the bias voltage is optimized at 1.88 V, and almost all of the power is in the first order diffracted beam, while only a small amount remains in the zero order.[50]

order beam reaches a maximum, giving maximum efficiency. As the voltage is increased further, more orders become apparent, and at 2.26 V, both the first and second order diffraction patterns are clear. If we continue to increase the bias voltage, the second order fades and the first order appears clearly again at approximately 4.65.

4.2.3   Multiple Beams

We also created multiple Bessel beams out of a single Gaussian beam. There are two ways in which to achieve this. The first is to divide the mask into separate masks for each Bessel beam we want to create and tile the masks. This method is flexible because we can use different parameters for each vortex that we create.   Fig. 4.12 shows four tiled Bessel beams. We can also create multiple beams by nesting multiple singularities within a single hologram as shown in Fig. 4.13. These are less flexible because all of the
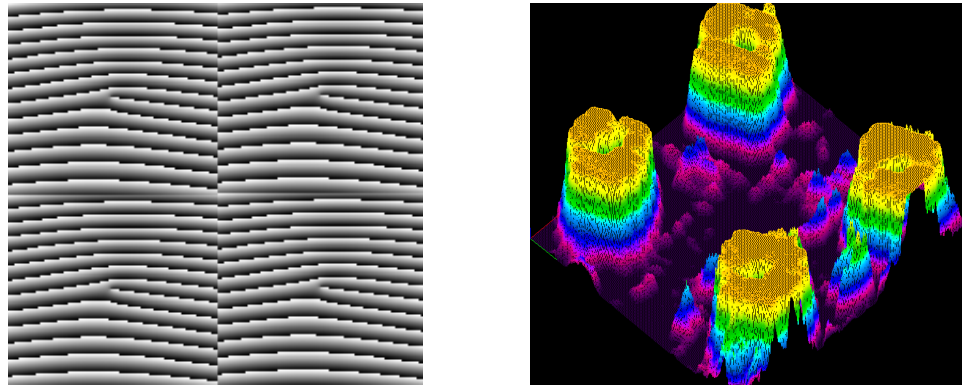
Figure 4.12: Four tiled Bessel beams and the hologram that is used to create them, color and height represents intensity, the center of each beam is hollow (zero intensity), which is not visible due to the tilt of the picture. Note the destructive interference in the center of the 3-dimensional picture.
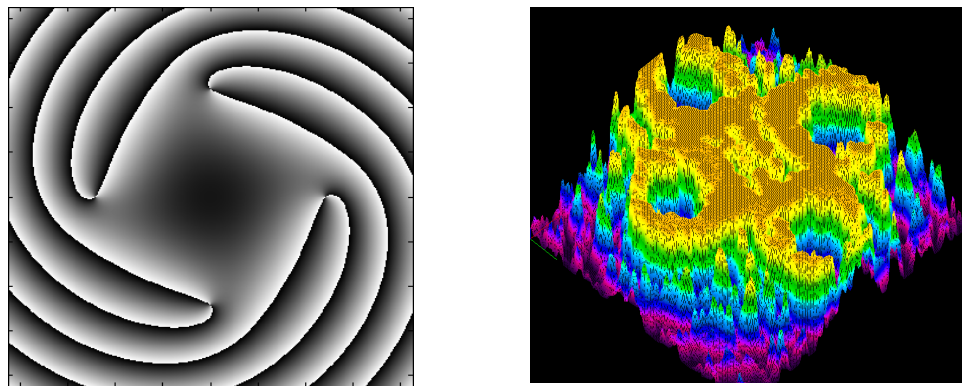
Figure 4.13: Four nested Bessel beams and the hologram that is used to create them, color and height represent intensity, the center of each beam is hollow (zero intensity), which is not visible due to the tilt of the picture. Note the constructive interference in between the Bessel beams.

parameters for each singularity have to be similar.

4.2.4 Propagation Length

As the propagation distance increases, the amount of laser power in the first ring of the Bessel beam increases. Thus, as the beam travels further from the SLM, the singularity in the center becomes better defined. Also, as the beam propagates, the anomalous diffraction patterns diverge away from the center of the first order beam, making the Bessel beam clearer. As shown in Section 2.4, the length that the beam will propagate without diffracting is limited due to the aperture size and goes as

$$z_{max} = \frac{\rho_0 R}{\lambda}.$$
(4.9)

In these experiments, this is approximately equal to 30 m using $\rho_0 = 1.4$ mm, $R = 1.25$ cm, (the radius of our hologram), and $\lambda = 633$ nm.

4.2.5 Conclusions and Applications

The SLM provides us with a means to test a variety of different diffraction gratings. We are able to create Fourier holograms that can produce multiple Gaussian spots in a wide variety of configurations. It also allows us to create Bessel beams out of Gaussian beams with real time control over the size of the singularity and the deflection angle. The spots are stable in time so that particles do not escape. This technology has applications in controlling cold atoms such as the guiding of atoms into traps[32] and atom lithography. Also, using the billiard traps, it may be possible to observe an atom undergoing Brownian motion or moving in a chaotic fashion.

Chapter 5

Erbium Doped Fiber Ring Lasers

With the rise of the telecommunications industry came a rapid development in fiber and fiber amplifier technology. Due to the need to amplify signals as they travel through fiber, Erbium Doped fiber amplifiers (EDFA's) have become readily available for use in industry as well as in the scientific community. Because they can easily be configured as the active medium in a laser cavity, they have been used in optical chaotic communications experiments over the last decade. Erbium doped fiber ring lasers (EDFRL's) are a good choice in chaotic communications because they generally have a large number of parameters that can be varied and a large number of longitudinal modes propagating within the cavity[52, 53, 55]. This makes their dynamics complex and difficult to replicate.

These complex dynamics also make EDFRL's a good tool for studying high-dimensional dynamical behavior that occurs on multiple time scales and developing new analysis techniques for such systems. Since the EDFRL's used in the experiments described in this thesis are composed of EDFA's and passive single mode fiber, this chapter will provide a brief overview of these components as well as a description of the applications of such systems.

5.1   Fiber Characteristics

Optical fiber has been a primary waveguide in optics and communication over the last decade. It has become commonplace in businesses and residential communities as the carrier of information over the Internet and telephone. An optical fiber is called single

44

9 μm Core

Plastic Buffer

125 μm Cladding
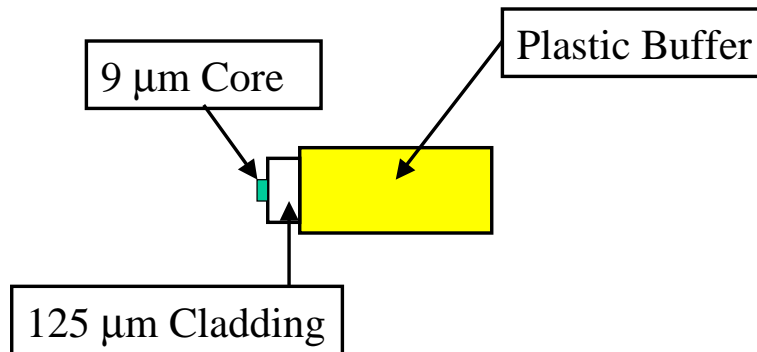
Figure 5.1: Diagram of a single mode nonpolarization maintaining optical fiber.

mode if the size of the core is only big enough to allow a single transverse optical mode to propagate. As shown in Fig.5.1, single mode optical fiber (SMF) consists of a 9 μm fused silica core surrounded by a 125 μm cladding. The light propagates through the core, reflecting off of the cladding with total internal reflection since has a lower index of refraction than the core. A core index of refraction of 1.45 and cladding index of refraction of 1.443 is typical for SMF. For a complete description of how to determine core and cladding size and indices of refraction see Refs.[56, 57].

The optical fiber used in the experiment was nonpolarization maintaining, meaning that the polarization state of the light is affected by the waveguide itself[58, 59]. The polarization rotations that occur in an optical fiber can be explained by treating an optical fiber as a concatenation of randomly oriented optical waveplates. The effects of these waveplates can be expressed as a product of unknown phase shift and rotation matrices, resulting in an arbitrary unitary matrix. The most general form of this matrix, called the

unitary Jones Matrix, takes the form

$$\mathbf{J} = \begin{pmatrix} a & b \\ -b^* & a^* \end{pmatrix} \tag{5.1}$$

where $|a|^2 + |b|^2 = 1$, and is used to describe the transformation of two orthogonal polarization states of the electric field upon traversing the fiber[58]. The birefringence of the fiber, or the orientation of the pretend wave plates, is sensitive to environmental factors such as stresses and temperature. These variations are observed on very slow time scales. Other nonlinear effects of fiber will not be discussed in detail because they are not relevant to the experiments presented in this thesis. However, a full description of the nonlinearities in fiber is presented in Ref.[58].

5.2   Erbium Doped Fiber Amplifiers

Erbium doped fiber amplifiers (EDFA's) have gained tremendous popularity over the last decade in the field of telecommunications. The active lasing ion in these amplifiers is Er^{3+}, a rare earth ion that has transitions at 1.3 and 1.55 μm, the latter of which has minimum losses for propagation within SMF[56].

The energy level diagram of Er is presented in Fig.5.2 which shows both the absorptive and radiative transitions that can take place in the Er^{3+}. Since we would like our amplifier to operate at $\lambda = 1.5\ 5\mu$m, we would like to utilize the $^4I_{13/2} \rightarrow^4 I_{15/2}$ transition. Of the two possibilities for pumping, 1.48μm and 980 nm transition, only the 980 nm allows for the ion to quickly decay into the $^4I_{13/2}$ state by a nonradiative decay process from the $^4I_{11/2}$ excited state, allowing it to efficiently achieve population inversion over the ground state. When pumped with 980 nm light, EDFA's utilize a three level lasing transition whose terminal level is the Er^{3+} ground state. Lasing in this system is catalyzed
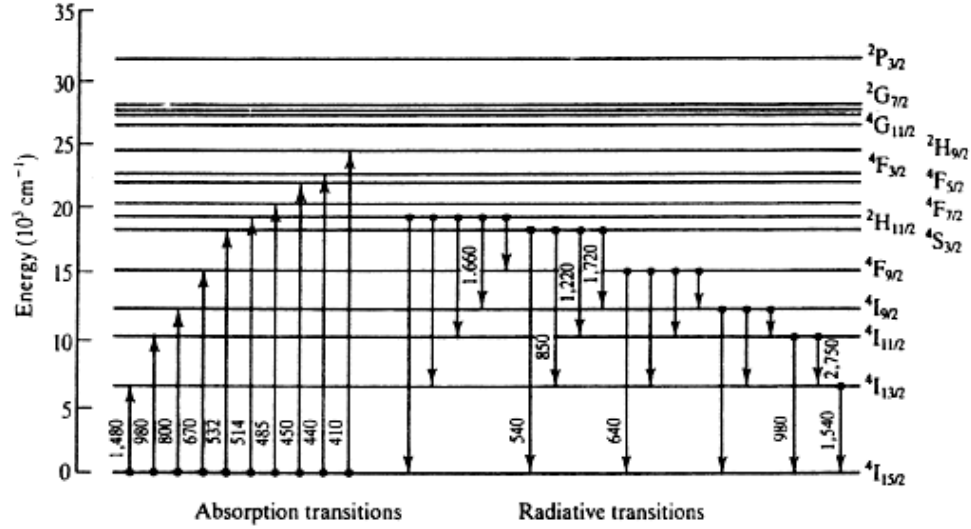
Figure 5.2: Energy level diagram of erbium doped optical fiber[62].

by the long fluorescence lifetime of Er^{3+} ($\tau_f = 10$ ms), which allows the system to achieve a population inversion between the metastable intermediate state and the terminal ground state[60].

EDFA's display a large amount of spectral broadening, even though the radiative transitions occur at quantized energy levels. This broadening is due to effects such as the spin-orbit coupling, electron-electron interactions and most significantly the Stark effect[60, 61], due to interactions with the fused silica host. The Stark effect is seen when the crystalline host material generates local electric fields due to its structure. These fields may break degeneracies in the energy levels of erbium, causing transitions to occur over multiple energy levels. Since these fields can be generated on length scales that are very small, the amplitude of the fields can vary throughout the crystal, causing erbium to lase over a wide range of frequencies. This mechanism allows for substantial broadening of the spontaneous emission spectrum[62]. Figure 5.3 shows a typical erbium spontaneous emission spectrum when pumped with 980 nm light. Though the spectrum is centered around 1540 nm, significant gain is observed in the amplifier between 1525 and 1560 nm[62].
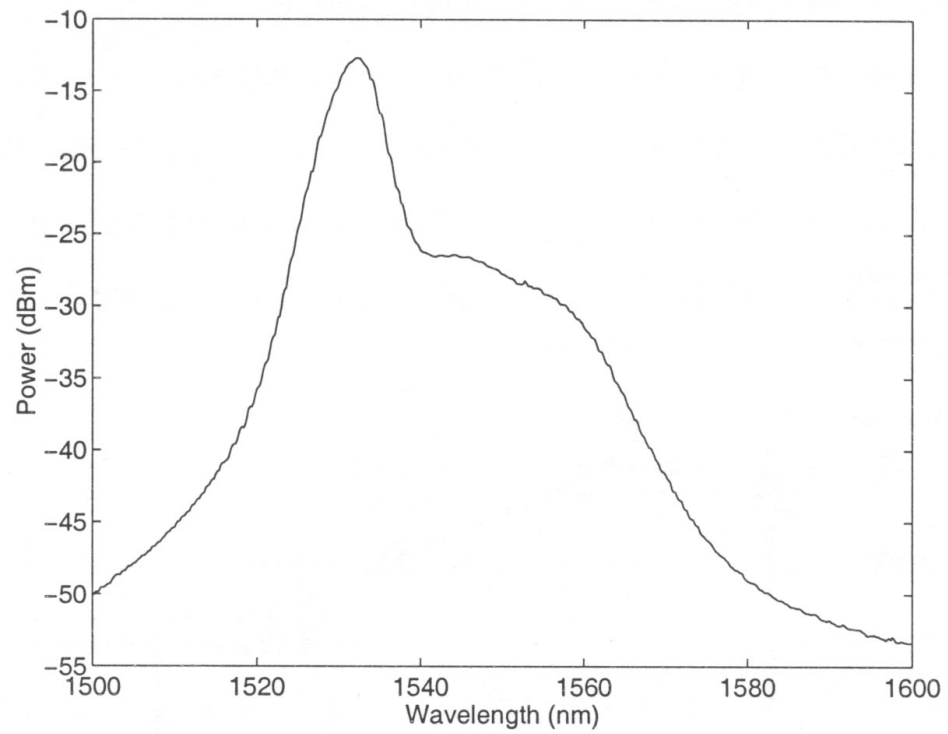
Figure 5.3: Amplified spontaneous emission (ASE) spectrum of erbium doped fiber pumped with 980 nm light[62]
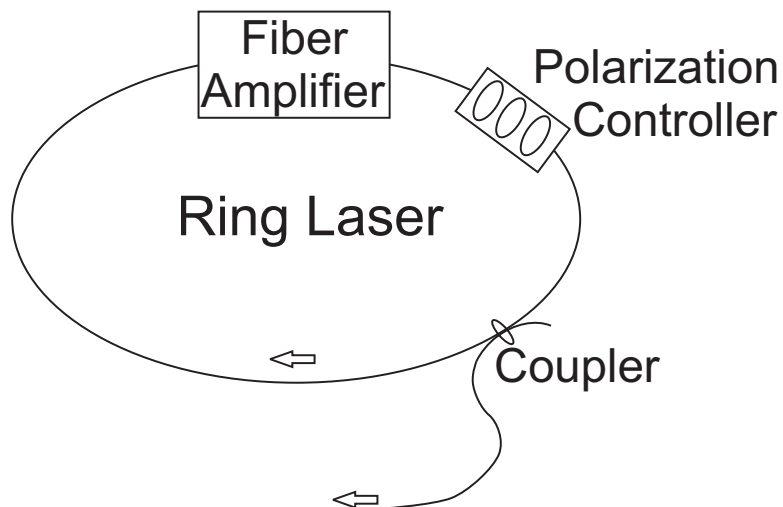
Figure 5.4: Simple erbium doped fiber ring laser setup. The fiber amplifier acts as the active medium of the laser. Light propagates unidirectionally in the ring, and may be coupled out using an evanescent field coupler. The net birefringence of the ring may be adjusted using a polarization controller which changes the number of modes that propagate within the laser[62].

5.3 Erbium Doped Fiber Ring Lasers

Depending on the configuration, erbium doped fiber can act either as an amplifier for coherent light emitted by a separate laser or as a laser itself when placed in a cavity. Doped fiber amplifiers are used as in-line amplifiers in fiber communications channels and Er^{3+} is a popular choice of dopant ion due to its high small-signal gain and noise characteristics[57]. However, the spontaneous emission noise in an EDFA often limits how many amplifiers can be put into a channel. With each addition of an EDFA, there is both an increase in both the signal and the noise level.

Amplified spontaneous emission noise, though a problem for communications, is what allows the erbium doped fiber amplifier to be turned into a laser. In an erbium doped fiber ring laser (EDFRL), the EDFA is connected to passive single mode fiber in a loop as shown in Fig.5.4. The EDFA acts as the active element in the laser and the loop is the cavity. It is often optically pumped at 980 nm using a wave division multiplexing
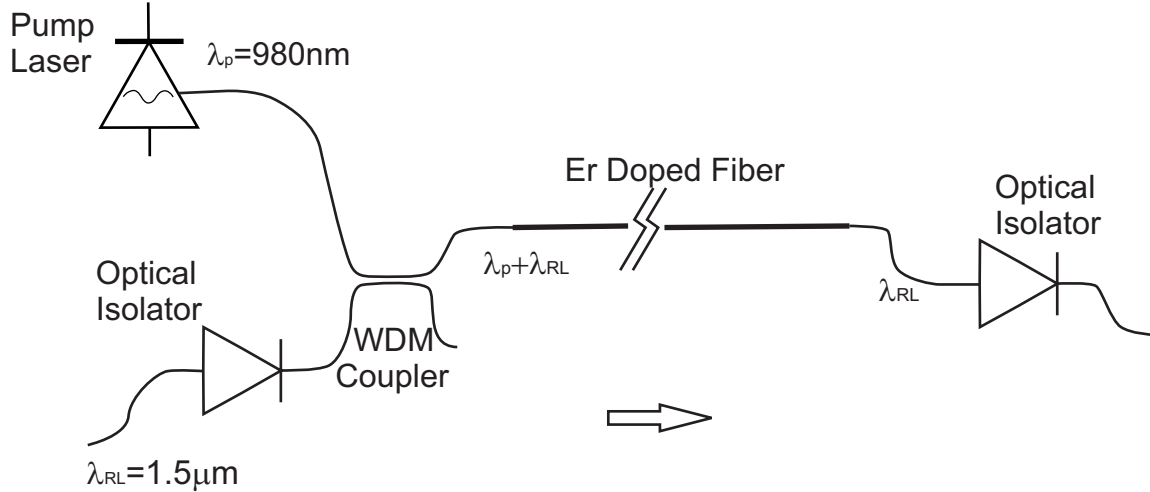
Figure 5.5: Basic component structure of an erbium doped amplifier. A 980 nm pump laser excites the erbium doped fiber. The pump field is injected into the doped fiber using a wave division multiplexing (WDM) coupler. Two Faraday optical isolators enforce the direction of propagation of the lasers in Fig. 5.4.[62]

coupler as shown in Fig.5.5, as it would be in an amplifier configuration, and a fiber isolator is inserted into the ring to ensure unidirectional operation in the experiments presented in this thesis.

Lasing is initiated by the spontaneous emission noise once the amplifier attains population inversion. This noise then travels around the cavity and gets amplified as it passes again through the amplifier. Evanescent field couplers are inserted within the loop to extract a fraction of the laser light.

Since the cavity is composed of single mode fiber, the cavity lengths of EDFRL's can vary from tens of centimeters to tens of meters long. For longer cavities this leads to round trip times on the order of several hundreds of nanoseconds. Therefore we can resolve the dynamics of these lasers on both sub-round trip timescales and over several thousand round trips[61, 58, 63, 64, 5].

Even though we are using single mode fiber which allows only one transverse mode to propagate in the laser, many longitudinal modes can propagate simultaneously through

50
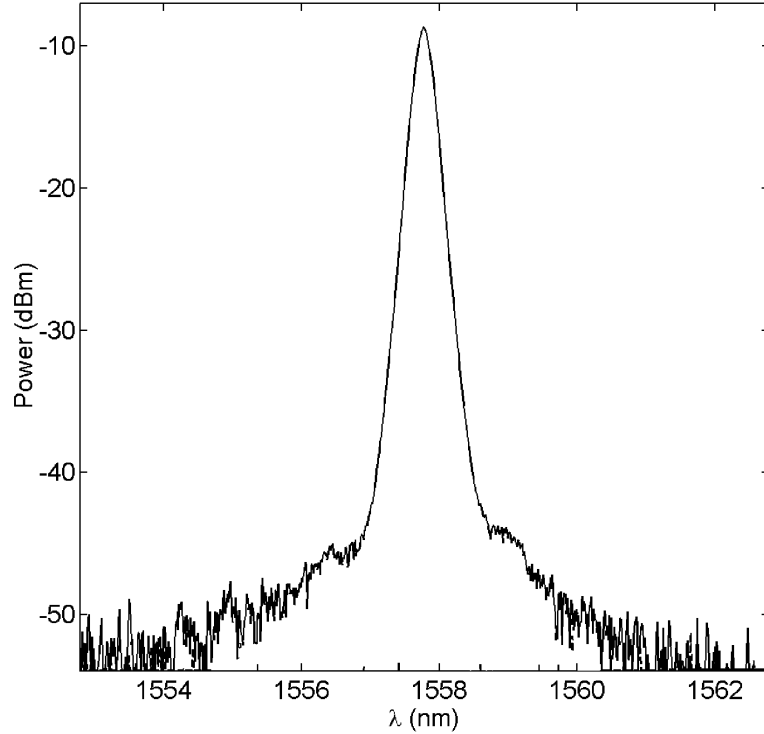
Figure 5.6: Optical spectrum of EDFRL pumped well above threshold. Polarization controllers are tuned to produce a single well defined peak. The full width at half max is $\Delta\lambda = 600$ pm while the longitudinal mode spacing is just 40 fm.

the cavity in different polarization states[55]. The total number of longitudinal modes that can propagate in the cavity depends on the cavity length. Using the polarization controller we are able to tune the net birefringence of the ring cavity, thus restricting the modes that can propagate and thereby controlling the optical frequency and linewidth of the laser. Polarization controllers for fiber ring lasers come in two forms. The first is composed of fiber and uses mechanical stresses on the fiber to induce a local shift in birefringence. A second type is used in the experiments presented in this thesis and consists of three waveplates, $\lambda/4, \lambda/2, \lambda/4$, in that order. The overall birefringence of the cavity is changed by rotating the waveplates and adjusting their relative orientations.

In the configuration described above, the EDFRL operating well above threshold has a much narrower linewidth than the amplified spontaneous emission (ASE) spectrum.

Figure 5.6 is a sample optical spectrum of an EDFRL with a cavity length of ~ 41.5 m pumped well above threshold. Using the polarization controller, the laser can be tuned to have a single well defined peak with an optical linewidth of $\Delta\lambda = 600$ pm FWHM. At this cavity length, we calculate that the mode spacing is only 40 fm.

Because the modes that propagate in the laser are governed by the net birefringence of the cavity, the orientation of the polarization controller can also govern the intensity dynamics of the EDFRL. Depending on the interference between the propagating modes, many different types of dynamics have been seen in EDFRL's, ranging from a relatively steady, nonchaotic output, to self pulsing, to chaos[64]. Injection of light into the cavity from other sources has also been seen to change the intensity dynamics within the ring[65]. In the experiments presented in this thesis, the individual ring lasers are tuned so that they have a steady output, with a very small ratio of noise to DC level and relatively narrow linewidth, $\sim$600 pm.

5.4   Coupled EDFRLs

For communications experiments, unidirectional coupling has been studied in EDFRL systems[52, 53, 54]. In this scheme, the optical field from one ring laser has been injected into the other laser. However, in this scheme, there is no synchronization between the drive and response laser. There are two reasons for this. The first, because synchronization is seen numerically in this type of configuration[66], it is thought that laboratory experiments cannot achieve the coupling strength needed for synchronization. The other explanation involves the destruction of the polarization and phase information by the fiber in the injection lines. It may be that the response laser does not receive enough information about the phase and polarization of the drive laser to synchronize to it. In order to create

a system for communication with unidirectional coupling, the receive laser must be in an open loop configuration, rather than a closed ring. For a complete description of these experiments see Refs.[52, 53, 54].

In the experiments presented in this thesis, the EDFRL's will be mutually coupled. These mutually coupled lasers provide the opportunity to study a high-dimensional dynamical system with very weak coupling that has dynamics on multiple time scales. This could lend insight into natural systems that function this way such as neurons and disease spread[8]. It also allows us to develop tools with which to analyze complex and high dimensional dynamics.

Chapter 6

EDFRL Synchronization

High-dimensional systems with dynamics on multiple time scales are prevalent in nature. As data collection techniques become increasingly able to capture long data sets encompassing many time scales, analysis techniques must be developed for these systems. Though many analysis tools have been developed for low-dimensional systems[21], there are far fewer available for complex high-dimensional systems. In mutually coupled systems it is difficult to determine which system is driving the dynamics or whether the two systems switch in their roles as leader and follower. One example of a recent attempt to develop high-dimensional analysis tools have been through statistical measures [67].

Mutually coupled EDFRL's are an ideal system with which to explore techniques with which to analyze high-dimensional data on multiple time scales[68, 69]. Due to the long cavity length many time scales can be resolved in this system, and the system is tunable over a wide variety of parameters. This chapter will explore several analysis techniques using coupled EDFRL's. These techniques can be extended to other high-dimensional dynamical systems including the spatiotemporal chaos in liquid crystals presented earlier in this thesis[70, 71].

6.1 Experimental Setup

Our EDFRL's consist of approximately 17 m of erbium doped fiber, the active medium, and approximately 29 m of passive single mode fiber, making the total length of both cavities approximately 46 m, within 1 cm of each other. The EDFRL's are pumped with
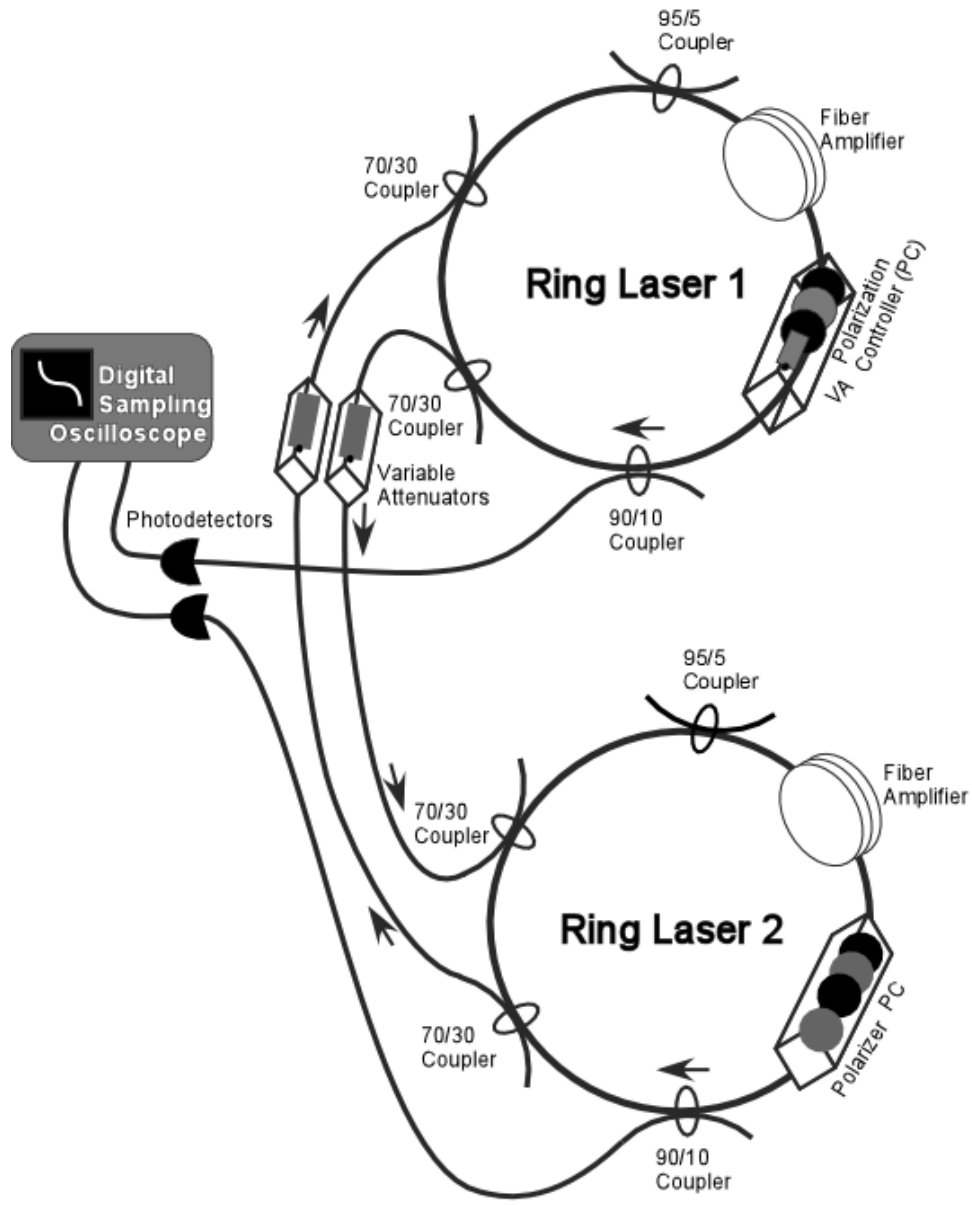
Figure 6.1: Coupled EDFRL's experimental setup. VA is the variable attenuator.[72].

identical 980 nm semiconductor lasers at a pump power of 120 mW, corresponding to approximately 1 mW propagating within each ring. The lasing threshold for our lasers is approximately 20 mW. An optical isolator is inserted within each ring cavity to ensure unidirectional propagation.

As shown in Fig. 6.1, each laser has a Gould 70/30 fiber optic evanescent field coupler that inputs the light from the other laser, and another identical coupler that outputs light to the other laser. The lasers also contain a Gould 90/10 coupler for monitoring and a Gould 95/5 coupler as an extra port for message injection. The ports are placed at the same location in each ring, as shown in Fig. 6.1. The ports of the couplers not in use are angle cleaved to ensure that there are no back reflections and were monitored to make sure that the light was only propagating in the correct direction inside the cavities.

The lasers are connected via two injection lines, which consist of passive single mode optical fiber, one coupler, and a variable attenuator. In this configuration, we have the ability to monitor and control the amplitude of the light injected into the lasers through the coupler and variable attenuator, respectively, and observe it on an oscilloscope. The injection lines are approximately 9 m long, corresponding to a travel time of approximately 45 ns, and again they are matched within 1 cm. Injection line lengths of 200 m and 25 km were also tested.

The electric field intensity of each laser propagates along identical lengths of fiber to a 125 MHz bandwidth NuFocus detector which is connected to a 1 GSample/s LeCroy digital sampling oscilloscope. The output fiber is also connected, through another evanescent coupler, to an optical spectrum analyzer so that we can monitor the optical spectra of the lasers in addition to the intensities.

The coupling strength, κ is defined as the percentage of power in the injection line

relative to the amount of power circulating within the ring. The lowest coupling strength that can be resolved in our system is $\kappa = 0.01\%$. Since each coupling line has its own variable attenuator, we can vary the coupling strength in each line independently. Unless otherwise specified, for the experiments presented here, the coupling strengths were equal in the coupling lines leading to symmetric mutual coupling. The maximum coupling we can achieve in our system is approximately 2.28%, so in all cases the two lasers are weakly coupled. To characterize the changes in intensity, coupling lines of 200 m and 25 km were tested and the propagation error of the intensity was calculated. It was found that the fiber does not change the intensity of the light, but the polarization and phase information cannot be determined by such a measurement.

6.2   Laser Output Characteristics

Once above threshold, the uncoupled ring lasers have a stable output wavelength with small amplitude fluctuations. An intensity time series of both uncoupled lasers can be found in Fig. 6.2, where blue represents the intensity of Laser 1 and red represents the intensity of Laser 2 with an artificial DC intensity offset. Each panel is a zoomed in view of the panel above it. The fluctuations that are present are a result of spontaneous emission in the erbium doped fiber that is amplified and slightly modified each time it passes through the active medium. This process occurs once each round trip, giving it a 220 ns periodicity. However, the amplitude of the fluctuations are not large when compared to the mean value of the emitted light, i.e. these uncoupled lasers are stable. However, if we look at the lasers on a long time scale, we see that there are fluctuations occuring on microsecond time scales due to the slow variation of the fluctuations as they are amplified. The round trip time periodicity is visible in the power spectrum in Fig 6.3, where we see
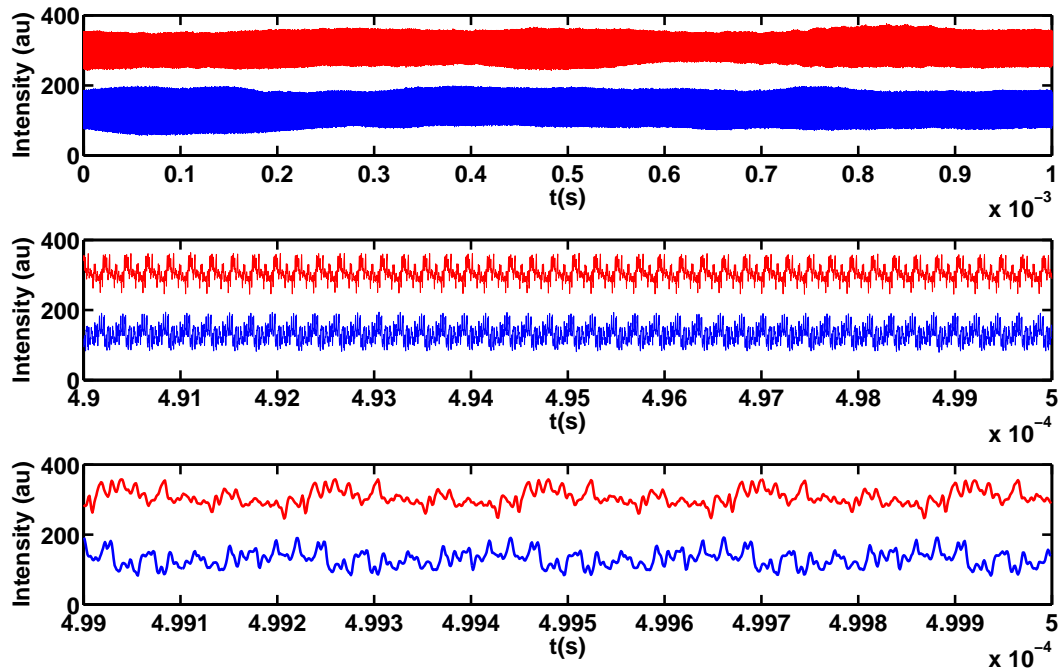
Figure 6.2: Solitary laser intensities as a function of time; blue is Laser 1 and red is Laser 2; the DC offset is artificial. The uppermost panel is 1 ms of the intensity dynamics of the uncoupled ring lasers. The middle panel represents 10 μs of intensity data taken from the center of the upper panel. The bottom panel now represents 1 μs, or $\sim$5 round trips, of intensity data.
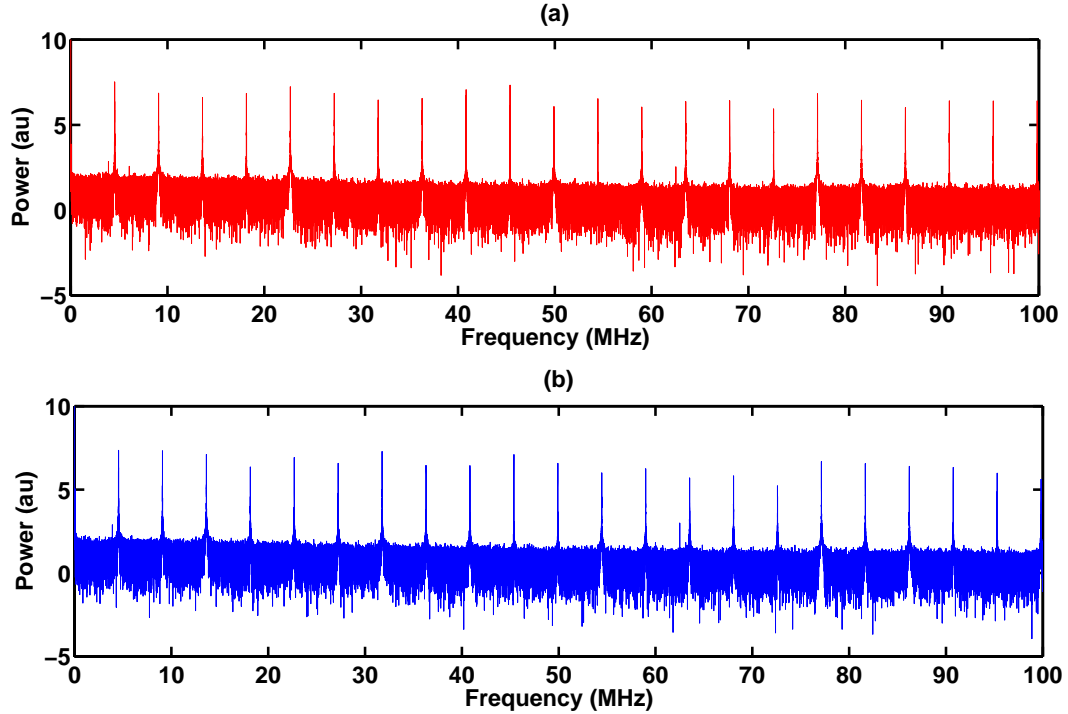
Figure 6.3: Power spectra of the solitary lasers, (a) Laser 2 and (b) Laser 1. Note that the peaks are 4.539 MHz apart, corresponding to the round trip time of the lasers.

a peak every 4.539 MHz.

The same stability can be found in the optical wavelengths of the lasers.   The solid line in Fig. 6.4 shows the optical spectrum of Lasers 1 and 2, where polarization controllers have been used to tune the center wavelength of each laser. The linewidth of the lasers are tuned with the polarization controllers to have a FWHM of ~1 nm. Once tuned, the optical spectrum of the laser remains stable within the precision of the spectrum analyzer.

6.3   Coupled Lasers

Once the lasers are coupled together at the lowest resolvable coupling strength, $\kappa = \sim 0.0114\%$, we see a dramatic change in the characteristics of the intensity fluctuations. Although the mean intensity of the lasers changes very little, the amplitude of the fluctua-
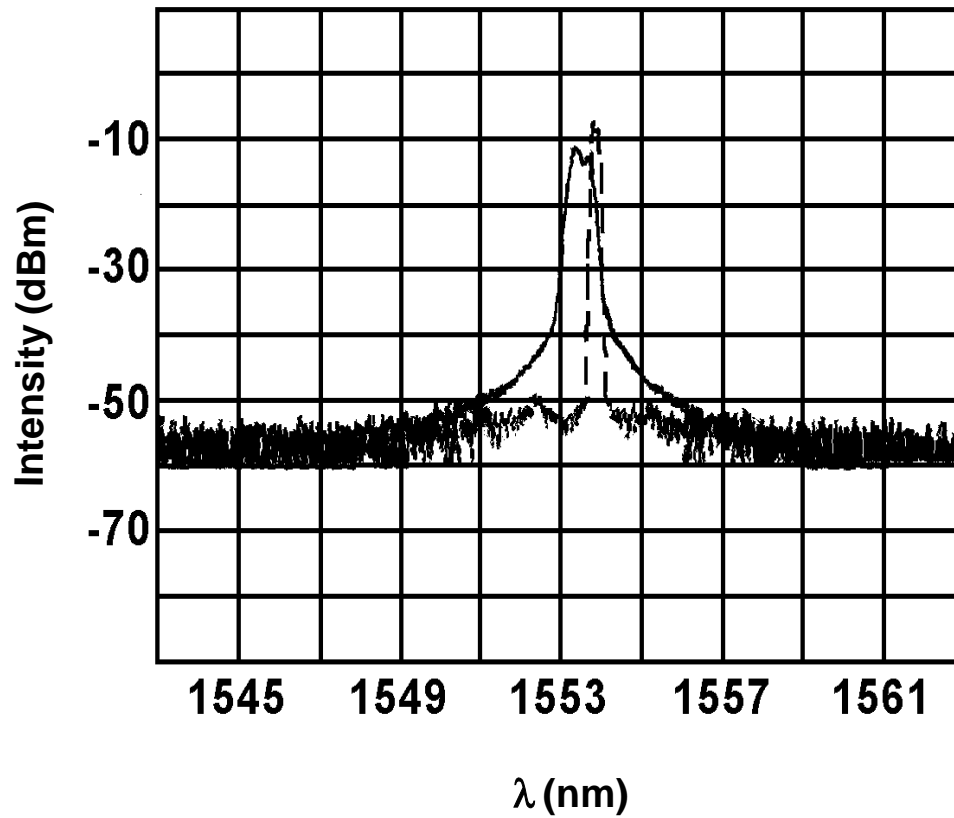
Figure 6.4: The optical spectra. The solid line is the optical spectrum with an FWHM of ~ 1 nm. The dashed line is the optical spectrum of the coupled lasers with a coupling strength of $\sim$2.5% where the linewidth has narrowed to $\sim$0.5 nm.
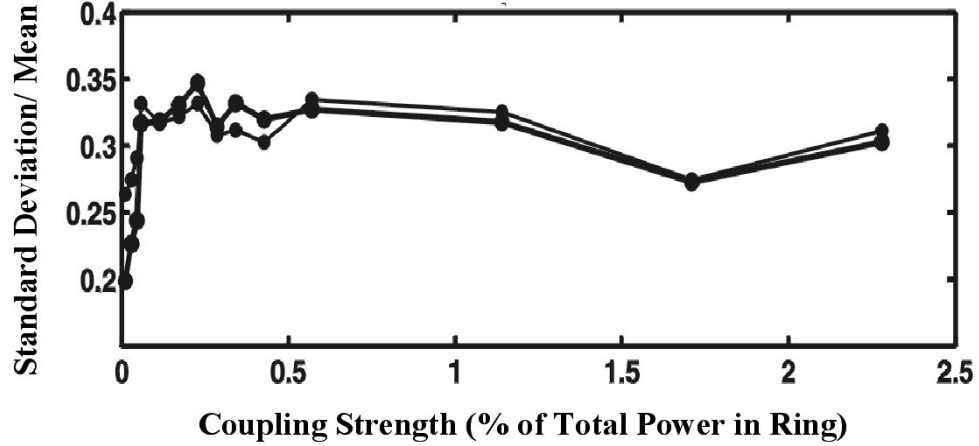
Figure 6.5: The standard deviation divided by the mean intensity as a function of the coupling strength.

tions increases and continue to increase with coupling strength until it reaches a maximum at $\kappa = 0.114\%$, after which it is constant. This can be seen in Fig. 6.5.

Once synchronization is achieved, there is a qualitative change in the intensity fluctuations. In Fig. 6.6, we see the same intensity time series of both lasers with a coupling strength of 2.28% on three different time scales. Although the mean stays constant throughout the time series, the intensity experiences large amplitude fluctuations on short time scales and the same smaller amplitude fluctuations on longer time scales that were visible in the uncoupled lasers. The amplitude of the short time scale fluctuations is a function of the coupling strength.

The optical spectra of the lasers also changes with the introduction of coupling. However, this change does not depend on the coupling strength, as with the intensity fluctuations, but on detuning. When the lasers are coupled, the optical linewidth immediately narrows to below 0.5 nm and, if the detuning is less than approximately 10 nm, they lock at a common wavelength, as shown by the dashed line in Fig. 6.4. In most types of lasers, the cavities are small enough to support only a few longitudinal modes. Since our lasers

61
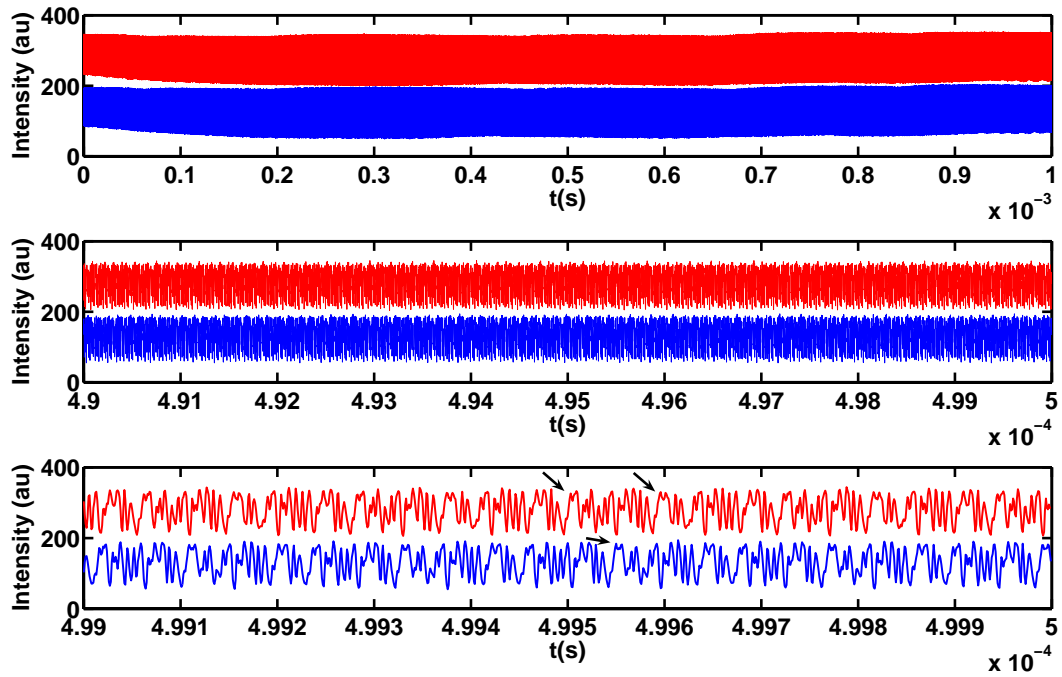
Figure 6.6: Symmetrically mutually coupled laser intensities as a function of time, blue is Laser 1 and red is Laser 2, the offset is artificial and the coupling strength is 2.28%. The uppermost panel is 1 ms of the intensity dynamics of the coupled ring lasers. The middle panel represents 10 μs of intensity data taken from the center of the upper panel. The bottom panel now represents 1 μs, or ~5 round trips, of intensity data.

(a)

(b)
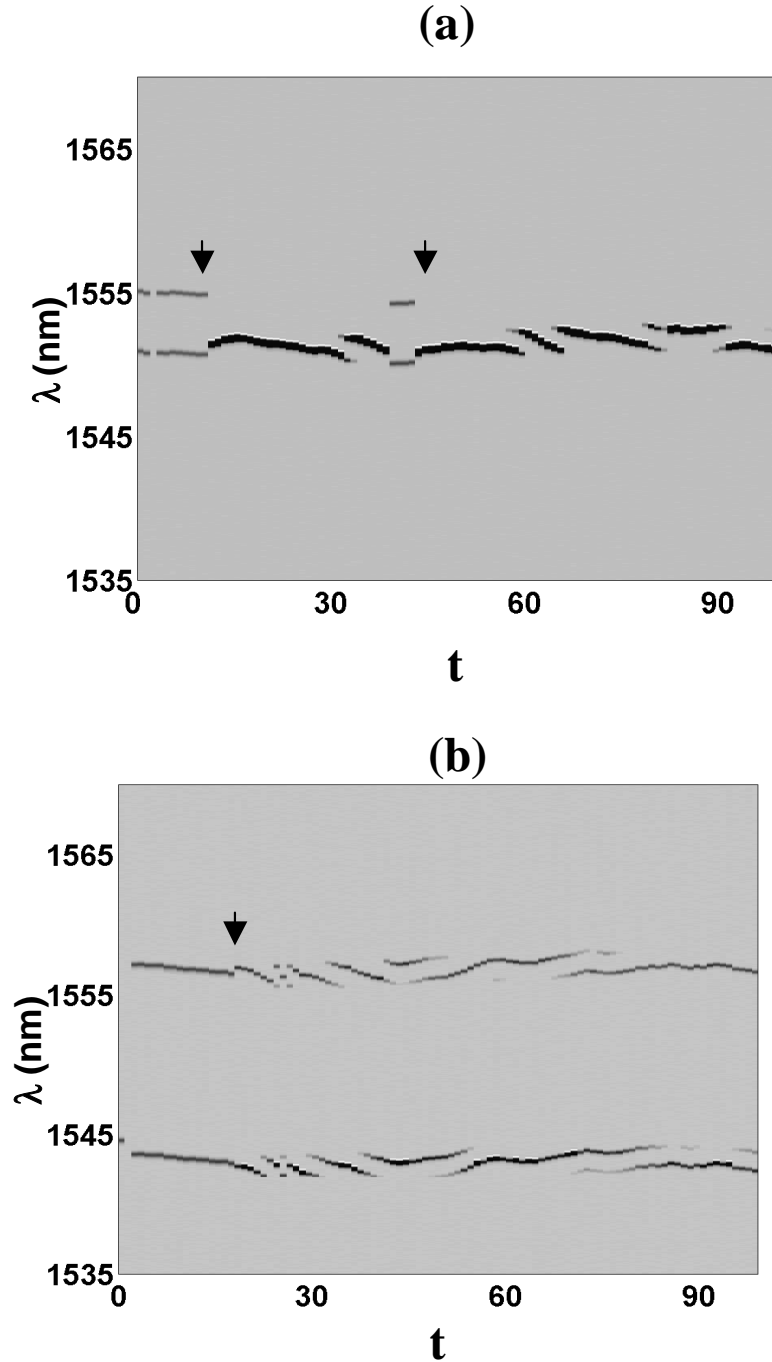
Figure 6.7: The optical spectra. Time is measured in units such that 0-90 is 30 s. The arrows indicate when the two lasers were mutually coupled. Following the arrows, the plot represents the optical spectrum of both lasers. (a) shows the movement of the peak wavelength of the two lasers as they move together and demonstrates the effect of opening and closing the injection lines on the wavelength fluctuations, the initial detuning between the lasers is ~5 nm. (b) shows the lasers moving together even though they do not lock at a single wavelength because the uncoupled lasers were detuned too far away from each other, the initial detuning is ~13 nm. All figures have coupling strengths of approximately 2.5%.

have such a large cavity and can support many modes, we see interesting optical wavelength behavior at large detunings. With detunings greater than approximately 10 nm, the optical linewidth still narrows but the lasers now each lase at both wavelengths, as long as they are both supported by each cavity. Figures 6.4 and 6.7 are the optical wavelength spectrum of the coupled lasers with a coupling strength of approximately 2.5%.

Once the wavelengths lock and the linewidths narrow, we see the common wavelength move very slowly over a range of approximately 2 nm. This drift occurs every time the lasers are coupled and can be seen in Fig. 6.7 where the arrows indicate the times at which they are coupled. When the detuning is less than 10 nm, they find a common wavelength, as shown in Fig. 6.7(a). If the detuning is too large for the lasers to lock at a single wavelength, both wavelengths drift together over their respective 2 nm range, as shown in Fig. 6.7(b). The center wavelength of each laser can be tuned independently.

Asymmetrically coupled lasers have wavelength and intensity fluctuations that behave similarly to symmetrically coupled lasers. However, in unidirectionally coupled ED-FRL's, the drive laser linewidth no longer narrows and the amplitude of the intensity fluctuations does not increase. This is because there is no injection into the drive laser in a unidirectional coupling scheme.

6.4   Synchronization

6.4.1   Average Synchronization Error for Mutual Coupling

The two uncoupled lasers exhibit chaotic intensity fluctuations that are not synchronized when the lasers are uncoupled. This can be seen in Fig. 6.2 where the intensity time series are not the same. However, with sufficient mutual coupling, the lasers synchronize. The two mutually coupled time series shown in Fig. 6.6 are synchronized with a 47 ns offset,
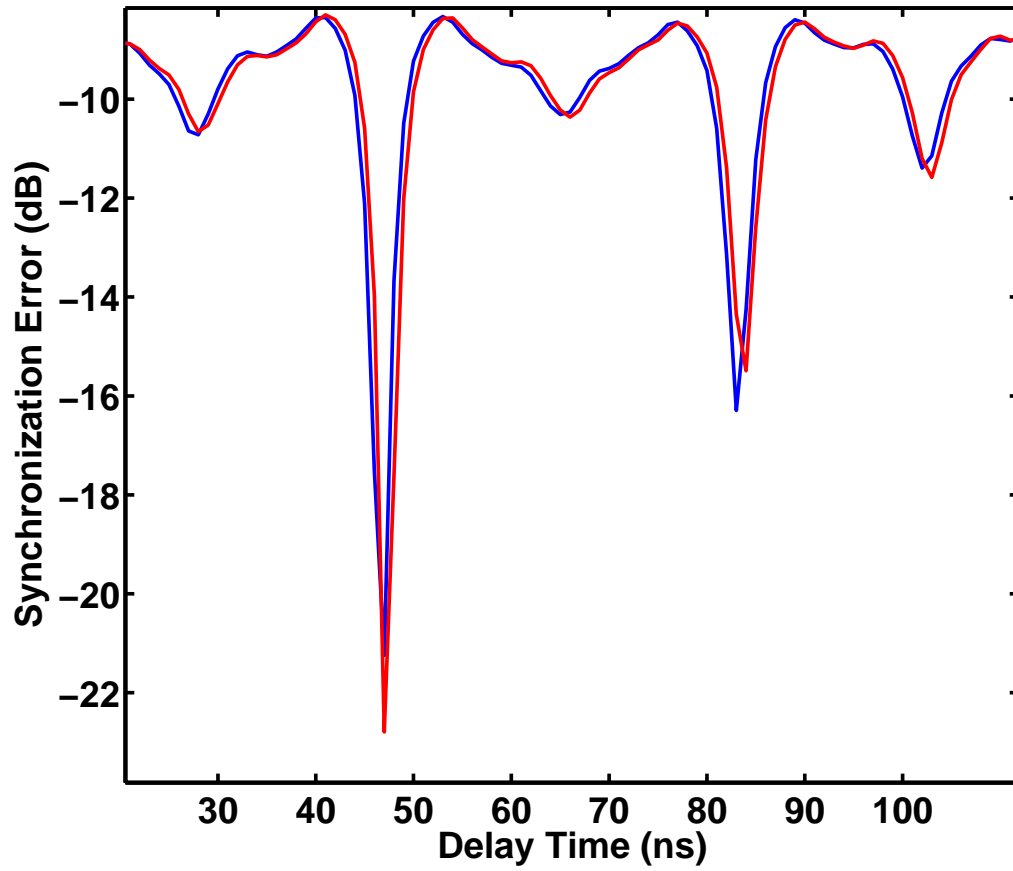
Figure 6.8: Synchronization error as a function of offset for two time series with a coupling strength of $\kappa = 2.28\%$, for Laser 1 leading (blue) and Laser 2 leading (red). The lowest synchronization error is at an offset of 47 ns.
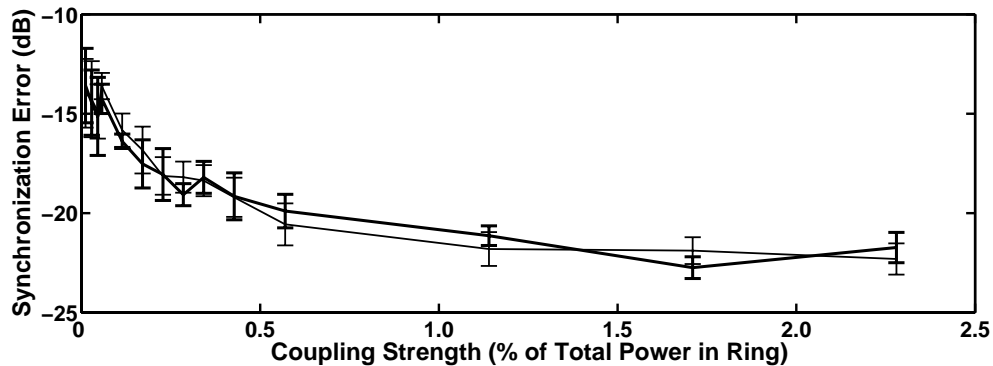
Figure 6.9: Synchronization error versus coupling strength, as averaged over each 1 ms intensity time series. The thin line represents the synchronization error if Laser 1 is leading Laser 2, and the thick curve represents the synchronization error if Laser 2 is leading Laser 1. The error bars represent the standard deviation of the synchronization error calculated for ten intensity time series at each coupling strength[72].

the travel time of light between the lasers, as shown by the arrows. The synchronization error is defined as the difference in intensity between the two chaotic waveforms as

$$\langle e(t) \rangle = 10 \times \log \left\langle \left| I_A^N(t) - I_B^N(t - \tau) \right| \right\rangle, \tag{6.1}$$

where the angle brackets denote time averaging.

$$I_{A,B}^N(t) = \left[I_{A,B}(t) - min(I_{A,B}(t)) \right] / max(I_{A,B}) \tag{6.2}$$

are the normalized intensities of the two lasers and τ is the offset, or travel time, between the lasers. If we average over the entire time series, we can identify a threshold for synchronization as a function of coupling strength. The correct offset is determined by calculating the synchronization error between two time series over a range of offsets. This can be seen in Fig. 6.8, where the global minimum for both Laser 1 leading (blue) and Laser 2 leading (red) occurs at 47 ns.   Figure 6.9 shows the average synchronization error as a function of coupling strength, the thin curve represents the synchronization error if Laser 1 is leading Laser 2 and the thick curve represents the synchronization error if Laser 2 is leading Laser 1, and the averaging occurs over each 1 ms intensity time series.

66

Each point is an average of ten different intensity time series at each coupling strength and the bars represent the standard deviation of the error at each coupling strength. We define two time series to be synchronized if they have a synchronization error of less than -20 dB. Therefore, we see that a coupling strength of $\kappa = 1.14\%$ is the threshold for synchronization in these ring lasers. Though this type of synchronization error analysis is prevalent in one way coupled systems where information about which system leads and lags is obvious, it is insufficient to determine a leader and follower in this type of mutually coupled systems.

6.4.2 Synchronization in Asymmetrically and Unidirectionally coupled EDFRL's

Figure 6.10 shows the average synchronization error for asymmetric coupling with Laser 2 coupling strength held at 0.285% and Laser 2 coupling strength varying between 0.285% and 2.28%. It is now clear that he coupling strength can be used to break the symmetry between leader and follower laser because a clear leader emerges.

Unidirectional coupling does not lead to synchronization for the coupling strengths achieved in this experiment. According to numerical simulations done prior to this thesis, a coupling strength of $\kappa = 2.28\%$ is sufficient to see synchronization between the drive and response EDFRL[66]. However, the models do not take into account the randomization of the polarization and phase of the coupling signal that occurs in the fiber.

Even though the lengths of the optical fiber are matched within 1 cm, all optical fibers contain defects that cause random changes in the birefringence. These defects inherently make each piece of fiber different from all other pieces of fiber so, even though the fiber is matched in length, they are not matched in the small perturbations they inflict on the light propagating through them. These birefringence shifts and environmental
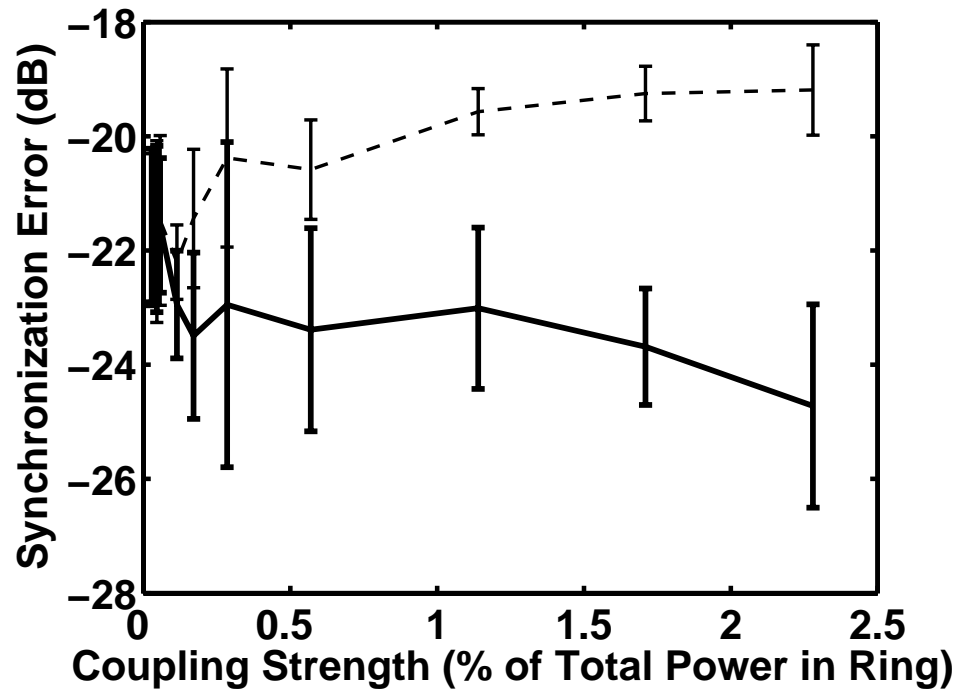
Figure 6.10: Synchronization error versus coupling strength for asymmetric coupling, as averaged over each 1 ms intensity time series. The thin dashed line represents the synchronization error if Laser 1 is leading Laser 2, and the thick curve represents the synchronization error if Laser 2 is leading Laser 1. The error bars represent the standard deviation of the synchronization error calculated for five intensity time series at each coupling strength[72].

factors cause the coherence length in fiber to be very short so as the light propagates through the coupling lines, the polarization and phase of the light changes. This implies that as the light travels through the injection lines between the lasers, the polarization and phase information that it began with has been transformed once the light reaches the other laser. If a device that destroys all of the phase and polarization information, such as an electro-optic modulator, is inserted into the coupling lines, synchronization never occurs in the EDFRL's with mutual coupling. This indicates that synchronization of chaos in EDFRL's depends on maintaining some phase and polarization information. When the lasers are mutually coupled, the lasers are more easily able to adjust to the dynamics of each other, and are therefore, able to achieve synchronization. However, with unidirectional coupling, the response laser is unable to adjust to the dynamics of drive laser and synchronize.

6.4.3 Identifying Leaders and Followers in Mutually coupled EDFRL's; Symmetry Breaking Part I

The dynamics of leader/follower symmetry breaking depend on the mutually coupled system that is being studied. In Ref.[73], the system of mutually coupled semiconductor lasers displays symmetry breaking that depends on the detuning between the two lasers. The symmetry in our system is not broken by detuning since the lasers can support such a large number of modes. We also know that there is no overall leader or follower when the synchronization error is calculated over a long period of time with offsets corresponding to each laser leading.

Therefore, we must look to other methods to identify leader/follower switching events. If instead of averaging the synchronization error over the entire 1 ms time se-

69
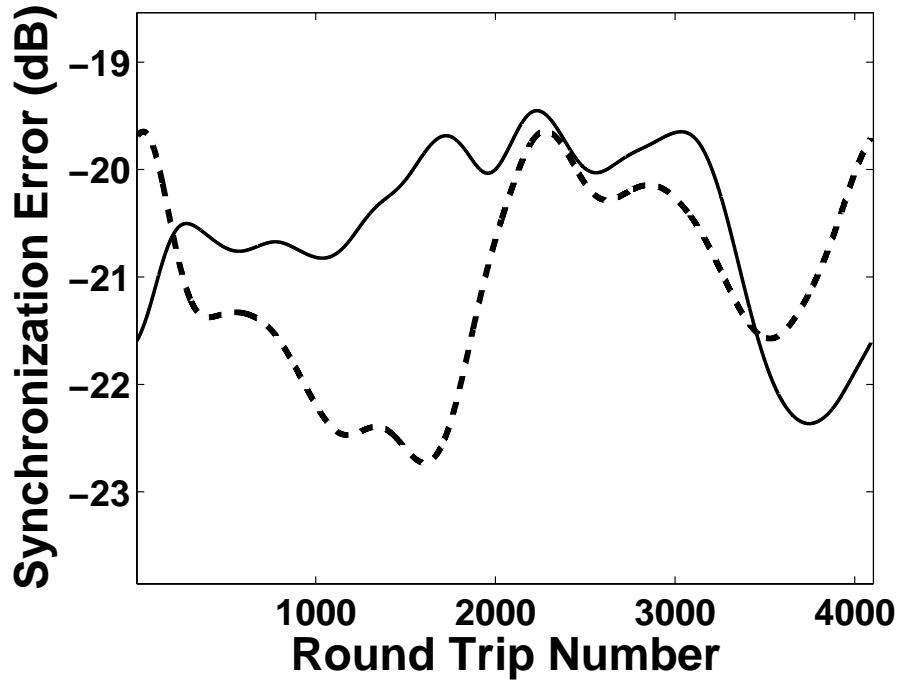
Figure 6.11: Synchronization error for $\kappa = 2.28\%$ as a function of round trip, solid (dashed) line represents the synchronization error if Laser 1 (Laser 2) is leading. No clear leader or follower is determinable.

ries, we average over half of the number of points in each round trip (110 points), which laser is leading may become evident. This synchronization error calculation is shown in Fig. 6.11 for a run where $\kappa = 2.28\%$. Again, the solid line represents the synchronization error if Laser 1 is leading and the dashed line represents the synchronization error if Laser 2 is leading. We see that both synchronization error curves lie almost on top of one another, with a synchronization error range that is $\sim$2 dB. Therefore, this type of analysis does not give us insight into leader/follower switching either.

Thus, we must look for a completely different way to identify the leader and follower laser in our experiment. One of the reasons that the traditional synchronization error analysis fails to identify leader/follower role switching is the distinct separation of time scales inherent in the system. They are separable into, from longest to shortest, the round

trip time of the lasers of ∼221 ns, the travel time between the lasers of ∼45 ns and the subnanosecond fluctuations within each laser. We also collect data at 1 sample/ns for 1 ms. Therefore, we collect a very long time series with fluctuations that occur on many different time scales. One way to detect shifts is to look for sudden changes in the shape of the fast fluctuations, as this is an indicator of a switch in the leader laser. However, since the shape of the fluctuations changes very slowly and the switches may occur over many round trips, they are very difficult to identify from a one dimensional time series. If the separation of time scales can be exploited to rearrange the time series into a two dimensional representation, the switches may become more obvious.

6.5   Two Dimensional Representation

The ability to experimentally resolve the intracavity dynamics of this system allows us to use a spatiotemporal representation of the intensity to study the synchronization, where the temporal position inside a cavity-roundtrip is mapped to its projected spatial position within the cavity[71, 70].   This representation is shown in Fig. 6.12, where the x axis is the normalized spatial position within the ring cavity, each horizontal row corresponds to 221 ns or one round trip. The y axis represents time measured in increments of the round trip number and the color represents intensity. We use the fact that the fluctuations are only slightly modified with each round trip to aid in this mapping. We cannot simply rearrange the one dimensional time series because the round trip is not exactly an integer number of nanoseconds, and therefore the number of points in the round trip will vary each round trip that is collected. Therefore, we must use a correlation function to determine where each round trip begins and how to line it up in the two dimensional plot. To make the alignment easier, we interpolate ten points per collected point using linear interpolation.
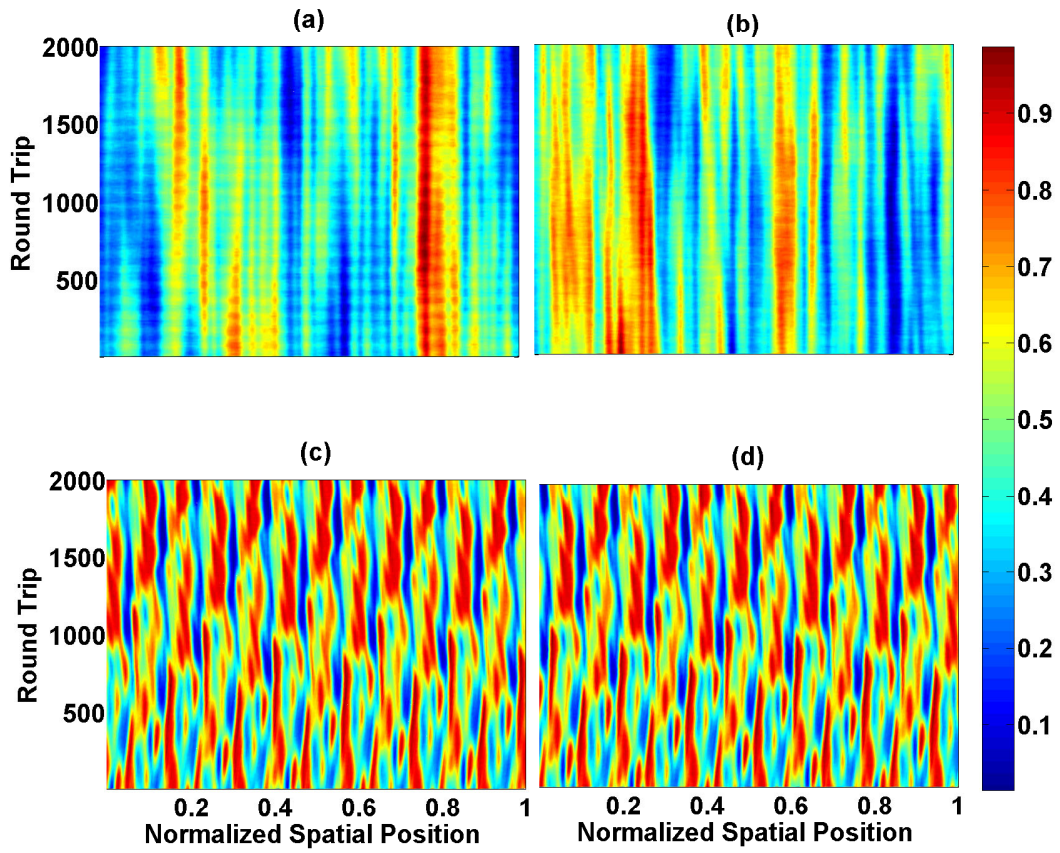
Figure 6.12: Spatiotemporal representation of the experimental time series; the color represents intensity in arbitrary units, the spatial position is normalized to one round trip in the fiber ring. (a) Uncoupled Laser 1 (b) Uncoupled Laser 2 (c) Mutually coupled Laser 1, $\kappa = 2.28\%$ (d) Mutually coupled Laser 2, $\kappa = 2.28\%$[72].

The plots shown in Fig. 6.12 have ten interpolated points per collected points and cover approximately 2000 round trips of each laser[72].

Figures 6.12(a,b) show the two solitary lasers in the absence of coupling. The lasers show qualitatively similar dynamics but they are not synchronized. The only periodicity that we see in the uncoupled lasers corresponds to the round trip time. Figures 6.12(c,d) correspond to the coupled case with $\kappa = 2.28\%$. There is now much more structure in the lasers' dynamics and they are synchronized with an offset. It is evident that there is another periodicity that has emerged as a result of the coupling, an approximately 90 ns periodicity corresponding to twice the travel time between the lasers. We also see that the patterns change at approximately round trip number 500. When the entire time series is plotted in this fashion, we detect another switch at approximately round trip number 2000. Therefore, this representation allows us to readily identify the pattern shifts.

6.6   Identifying Leaders and Followers; Symmetry Breaking Part II

We can use these two dimensional plots to more clearly identify these leader/follower switches. By subtracting the two space-time plots with an offset, we can determine when each laser is leading the dynamics. This is shown in Fig. 6.13, which portrays the subtracted experimental space-time plots, offset so that Laser 1 and Laser 2 are leading, respectively. In this representation, a lack of structure around 0 (green) indicates a good correlation, and the shifts in leader and follower are indicated with arrows. The switches between leader and follower are now clear and in Fig. 6.13, they occur at approximately round trip number 250 and round trip number 1700. The switches are also visible if we look at a plot of the standard deviation of the rows in the subtraction plots as a function of the round trip number, Fig. 6.14. We see a lower standard deviation when the Laser 1

(a)

(b)
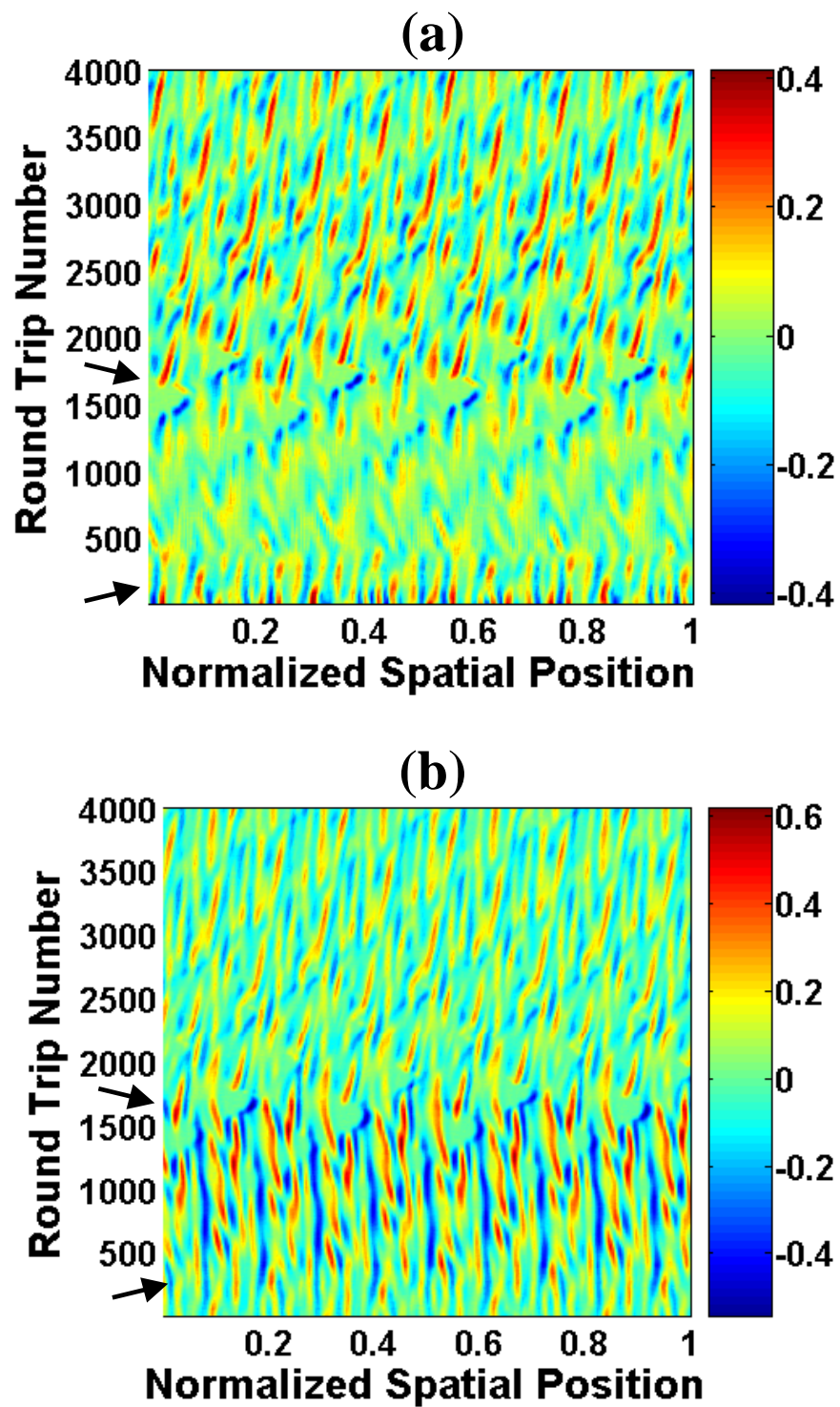
Figure 6.13: (a) and (b) Subtraction of the experimental space-time plots as if Laser 1 and Laser 2 is leading, respectively. The arrows indicate a switch in the leader and follower laser[72].
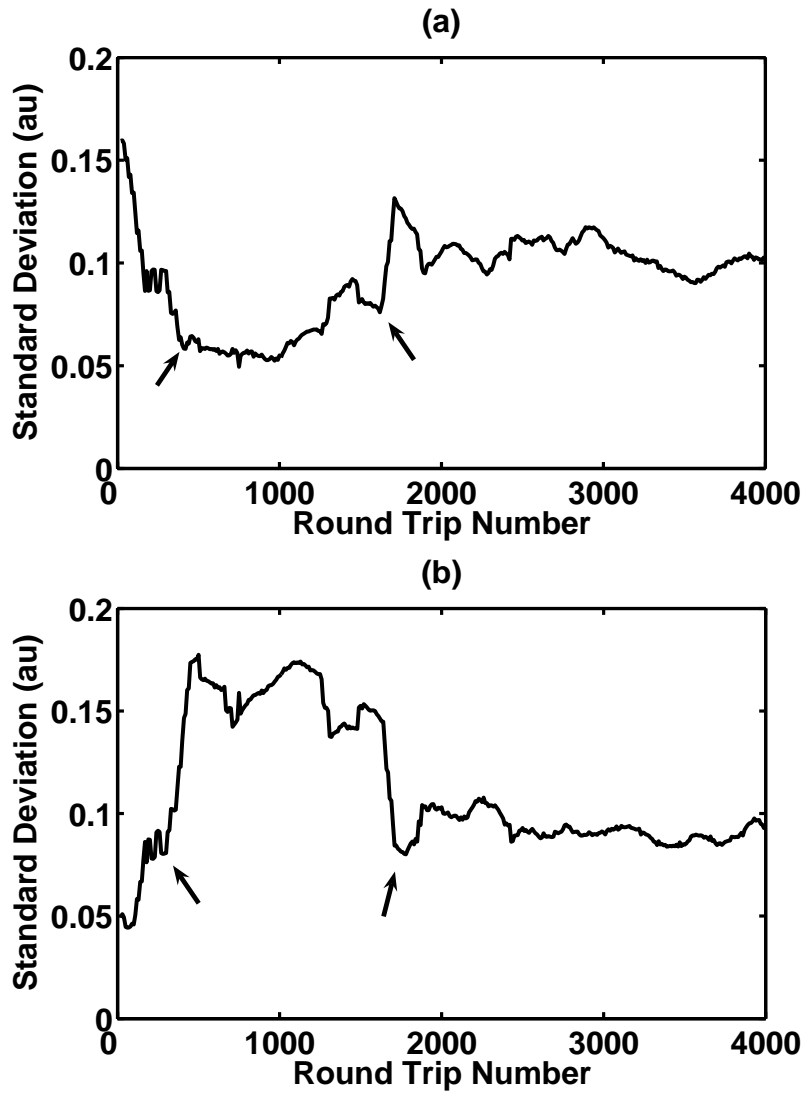
Figure 6.14: (a) and (b) Standard deviation of the rows of the subtraction of the experimental space-time plots in Fig. 6.13, as if Laser 1 and Laser 2 is leading versus the round trip number, respectively. The arrows indicate approximately where a switch in the leader and follower laser occurs[72].
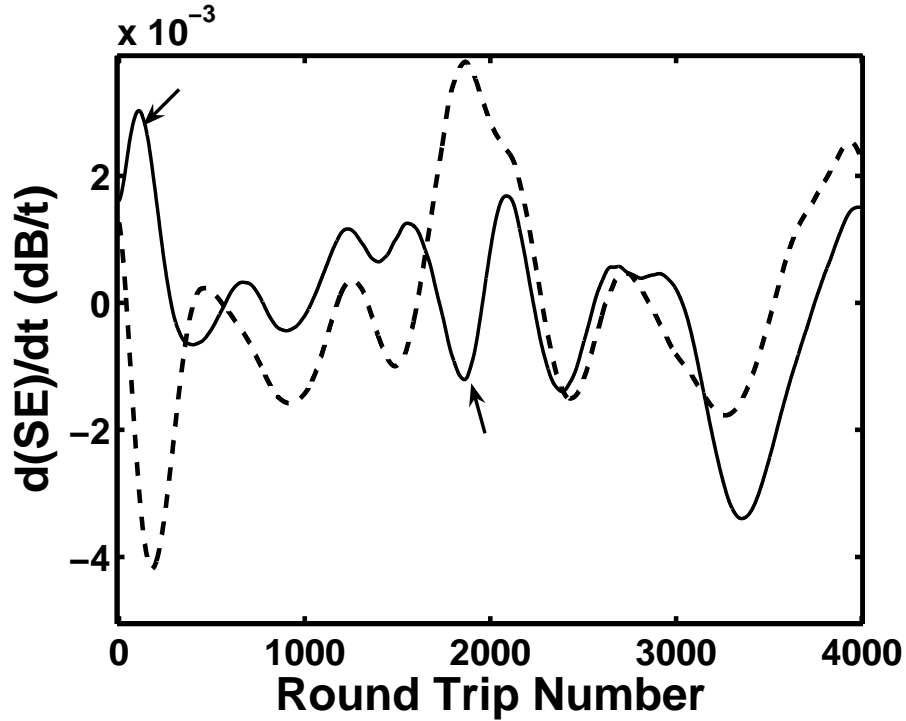
Figure 6.15: The derivative of the synchronization error as a function of round trip. The arrows indicate a switch in the leader and follower laser[72].

is leading in Fig. 6.14(a) than when it is not, and the same is true in Fig. 6.14(b), where we see a lower standard deviation when Laser 2 is leading than when it is not. The arrows indicate approximately where the switch occurs since the switch occurs over many round trips.

If we look back at the synchronization error averaged over every 100 points shown in Fig. 6.11, the role switching is still not visible. However, during such role switching events the two synchronization errors change quickly in opposite directions. In order to detect these changes, we plot in Fig. 6.15 the time derivative of the synchronization error for the two synchronization errors. One can see distinct changes in the behavior of the derivative where we have identified the shifts. The extrema of the derivatives of the two cases are in phase with each other at some times and out of phase with each other at

other times. According to the discussion above, when the extrema of the derivatives of the synchronization error become out of phase, a switch in the leader/follower roles is detected. These points are denoted by arrows in Fig. 6.15.

6.7   Karhunen-Loeve Decomposition

Another method for determining the leader and follower laser is an analysis of the spatiotemporal time series through Karhunen-Loeve (K-L) analysis. An extension of principal mode decomposition, K-L decomposition allows the extraction of the intrinsic modes of a system in space and the study of how these modes vary in time. The modes are found by extracting the eigenenergies of the system and the corresponding eigenfunctions. Time variation of the modes are studied by extracting the temporal coefficients. The K-L method has an advantage over other eigenfunction expansion methods because it takes the least number of modes to represent the dynamics for a given precision[7].

6.7.1   K-L Procedure

The K-L analysis procedure is as follows. Let $u(x,t)$ be the spatiotemporal data matrix to be analyzed.

1. Demean $u(x,t)$, that is, $u(x,t) = u(x_n,t) - \text{mean}(u(x_n,t))$.

2. Compute the covariance matrix, $k(x,x') = \langle u(x,t)u(x',t)\rangle_t$, where the brackets indicate time averaging.

3. Compute the eigenvalues (λ_n) and eigenmodes (ψ_n) of $k(x,x')$ where λ_n is the mean energy of each eigenmode. There will be as many eigenvalues as there are columns in the covariance matrix,N, but all will not be needed for reconstruction of the spatiotemporal time series to a given accuracy.
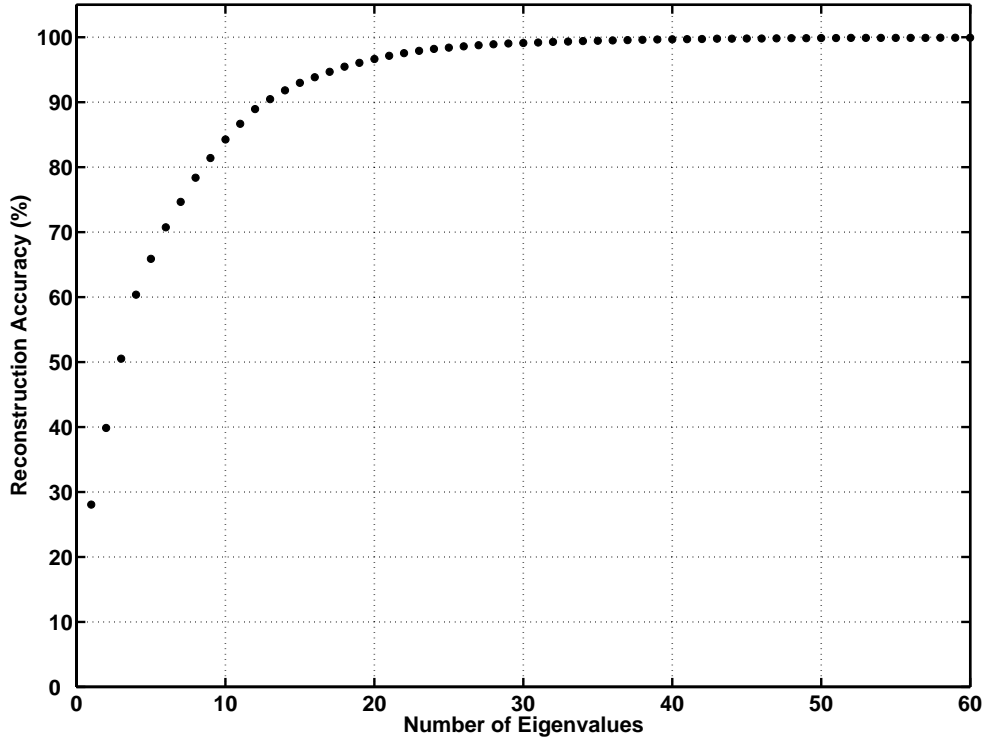
Figure 6.16: Accuracy of the reconstruction of the original spatiotemporal plot versus number of K-L modes used for Laser 1. 13 modes are needed to reconstruct the spatiotemporal time series of Laser 1 with 90% accuracy.

4. Order the eigenmodes in decreasing eigenvalue order so that the eigenmode corresponding to the largest eigenvalue is first, $n = 1$ and the eigenmode corresponding to the smallest eigenvalue is last, $n = N$.

5. Expand $u(x,t) = \sum_n^N \alpha_n(t)\psi_n(x)$ where the temporal coefficients are normalized such that $< \alpha_n(t)\alpha_m(t) >_t = \lambda_n \delta_{nm}$[7].

Figure 6.16 shows the accuracy for reconstruction of the original Laser 1 spatiotemporal time series as the number of eigenmodes that are used increases. This allows the truncation of the expansion for computational simplicity while retaining numerical accuracy. Figures 6.17(a) and 6.18(a) show the first four K-L spatial modes for Figs. 6.12(c)
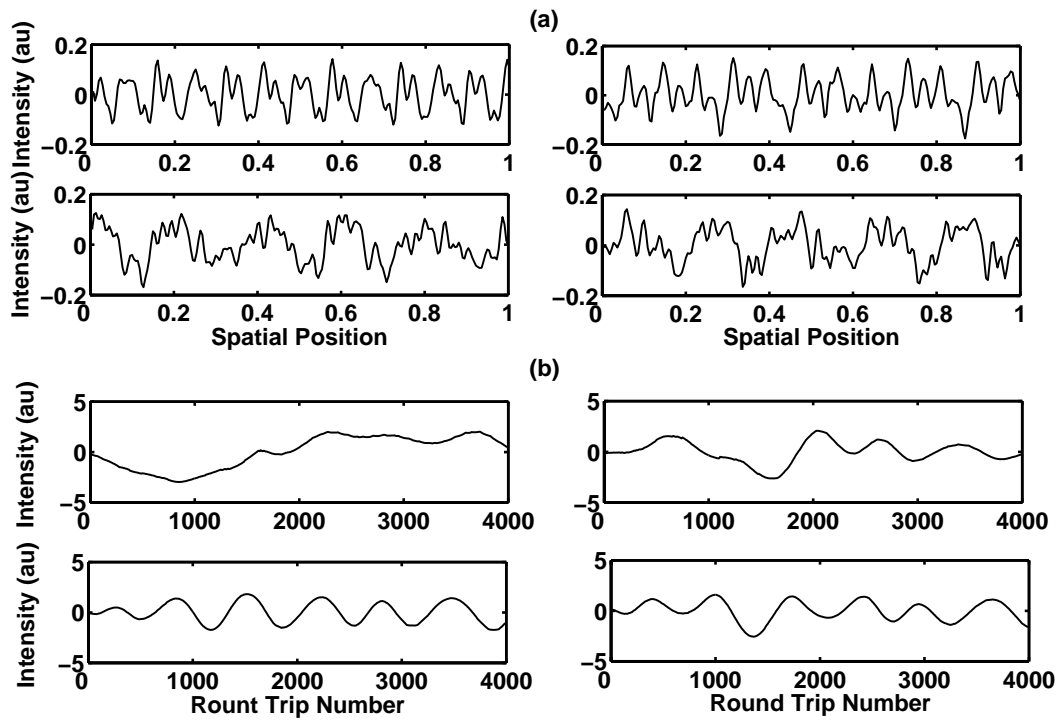
Figure 6.17: (a) First four spatial modes, $\psi(x)$, of the K-L decomposition of Laser 1, (read left to right), (b) first four time coefficients, $\alpha(t)$ of the K-L decomposition of Laser 1, (read left to right).
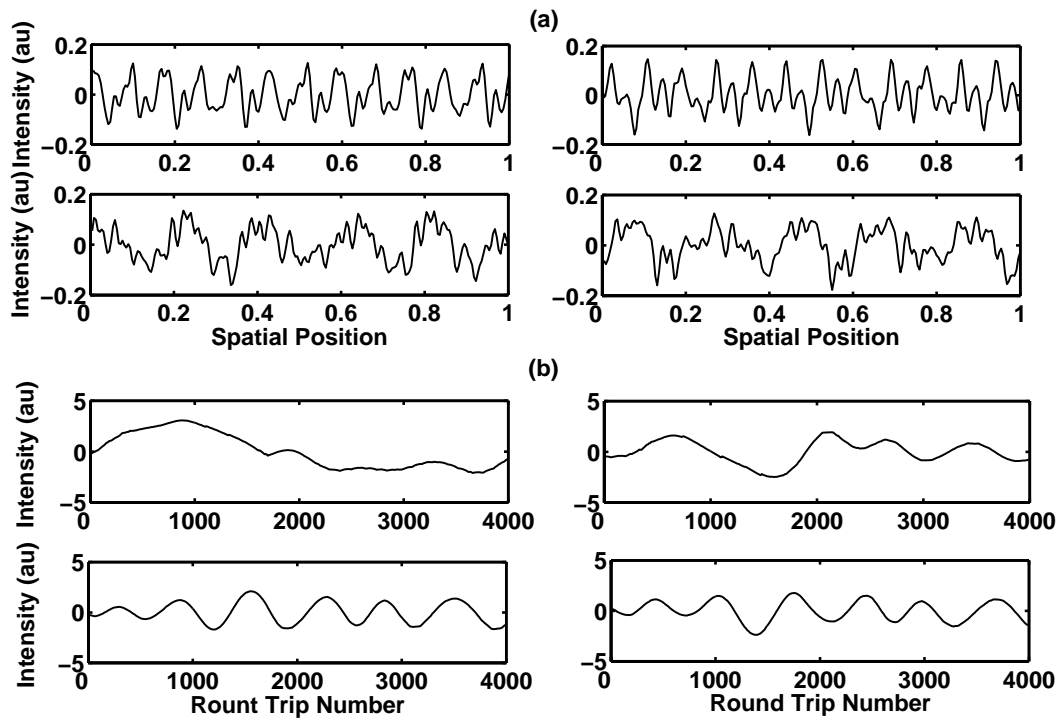
Figure 6.18: (a) First four spatial modes, $\psi(x)$, of the K-L decomposition of Laser 2, (read left to right), (b) first 4 time coefficients, $\alpha(t)$ of the K-L decomposition of Laser 2, (read left to right).

and (d). These are the spatiotemporal representations of Lasers 1 and 2, respectively with a coupling strength of $\kappa = 2.28\%$. Though they are qualitatively similar, the lasers are not synchronized, which is not surprising. The points that are eliminated in the space-time subtraction plot due to the offset make the two spatiotemporal time series linearly independent. Therefore, the eigenvalues and eigenmodes calculated from the corresponding covariance matrices should be different, and therefore, not synchronized. Figures 6.17(b) and 6.18(b) are the temporal coefficients for Laser 1 and 2, respectively. These are slowly varying and are similar for both lasers due to the similar environmental factors affecting them.

6.7.2   Preliminary Results for K-L Analysis of the Mutually Coupled EDFRL's

Even though the K-L modes of the individual laser are not synchronized when calculated independently, K-L analysis can be used to better understand and identify the switches between the leader and follower laser. Through a K-L decomposition of the space-time subtraction plots, the variation of the energies in each eigenmode as a function of time can be analyzed. Figure 6.19(a) shows the temporal coefficients for the space-time subtraction if Laser 1 is leading and Fig. 6.19(b) shows the temporal coefficients for the spacetime subtraction if Laser 2 is leading. In this analysis, a large value for the temporal coefficient intensity corresponds to a large amount of spatial structure. Therefore, when the two lasers are synchronized, the coefficient intensity will be low for all of the modes. A shift is detected when there is a sudden shift in the intensity of the temporal coefficients. Therefore, Fig. 6.19 shows that shifts occur at approximately round trip number 250 and round trip number 1700.
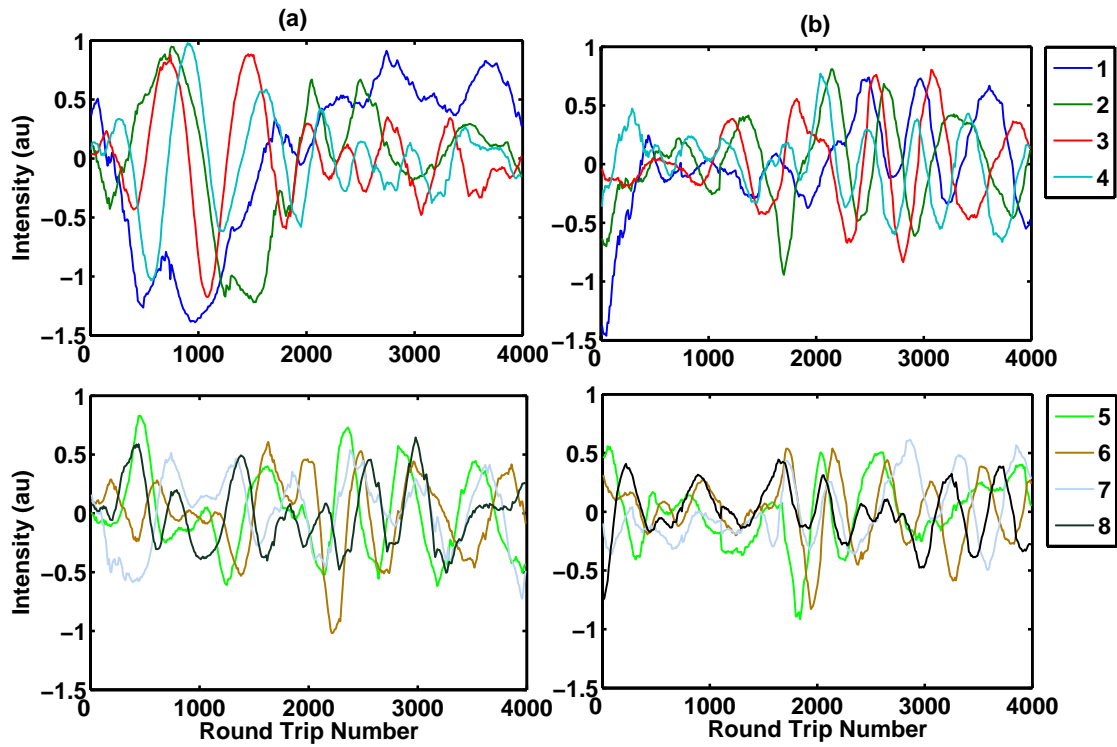
Figure 6.19: Temporal coefficients 1-8 of the K-L decomposition of the difference plots in Fig.6.13. (a) are the temporal coefficients of Fig. 6.13(b) where Laser 1 is leading, and (b) are the temporal coefficients for Fig. 6.13(a) where Laser 2 is leading.

6.8   A Physical Explanation

We hypothesize that the appearance of a leader and follower laser stems from the vast number of optical polarization modes within each cavity. When the two lasers are coupled, there are still over 10,000 optical modes propagating within each cavity. These modes wander in both frequency, over a range of approximately 5 MHz and in their polarization. We assume that each mode couples only to its nearest-neighbor mode in the other laser, but all of the modes are wandering, so that the nearest neighbor mode at one time may be different from the nearest neighbor mode at a later time. This causes modes to couple and uncouple from each other over time. It is also not assumed that all modes have equal intensities and, in fact, they most likely do not, and the distribution of intensities is likely to be different between the two lasers. Since we have seen that the leader/follower symmetry can be broken with unequal coupling strength, we can infer that optical modes with higher intensity will lead those with lower intensities. Therefore, since we observe the interference between all of the modes, as they wander we will see different patterns emerge as they synchronize and unsynchronize. If more high intensity modes in Laser 1 couple to lower intensity modes in Laser 2 than vice versa, we will see that, overall, Laser 1 is leading. If the opposite is true and more high intensity modes of Laser 2 couple to lower intensity modes of Laser 1 than vice versa, we will see that Laser 2 leads overall. As the modes couple and uncouple from each other, we will see switches between the leader and follower laser.

6.9   Conclusions

The methods for determining leader and follower laser presented in this chapter are useful for analyzing data from any high dimensional systems that exhibit dynamics on multiple

time scales. These types of systems are otherwise very difficult to analyze because often they have intrinsic periodicities that impede the use of traditional chaotic analysis. Therefore, new methods, like those presented above, must be developed to analyze these types of systems as data collection techniques evolve to allow us to collect data on multiple time scales.

The method of K-L decomposition as applied to the mutually coupled EDFRL's has application in other cases of high dimensional dynamical systems, the most relevant being the turbulent state of the liquid crystals with optoelectronic feedback presented in Chapter 5. In such systems, K-L decomposition can be used to better identify the degrees of freedom on which synchronization of the dynamics depends. This knowledge can then be used to better control synchronization of the dynamics and to develop lower dimensional models that accurately represent the dynamics.

Chapter 7

Coupled EDFRL Model

Since synchronization of coupled EDFRL's occurs in the fast fluctuations, we cannot use a model that uses mean field approximations like those usually used for laser models[74, 75]. In these models the dependence of the laser variables along the direction of propagation is ignored, an assumption we cannot make in our system. Therefore, we use a delay differential equation model derived from the Maxwell-Bloch equations. In this chapter we will derive the model equations starting with the Maxwell-Bloch equations and present results for synchronization and role switching in simulated mutually coupled fiber ring lasers. In this experiment we are only concerned with a single polarization mode since each polarization mode couples only with a single polarization mode in the other laser.

7.1   Derivation of the Model Equations

The model is based on an Ikeda-style set of delay differential equations[74, 75, 64]. They are derived in the spirit of Loh and Tang in Ref. [76] and have been used to model the dynamics of solitary EDFRL's in various dynamical regimes[66, 64]. This model will differ from that derived in Ref. [61] in that it will only contain a single polarization, and therefore, a single polarization mode. Since the model will simulate an erbium doped fiber laser system, it will be necessary to account for the three level transition of the Er^{3+} ion when pumped at 980 nm, and therefore, the population inversion will be defined as the difference between the number of ions in the intermediate state and the number of ions in the ground state, or $N = N_{int} - N_0$. This model is presented in Ref. [72].

We begin with the wave equation with a time-varying polarization and the Optical Bloch equations for the polarization and population inversion [61, 77](in all equations presented, $c/n \to c$),

$$\frac{\partial^2 \mathcal{E}}{\partial z^2} - \frac{1}{c^2}\frac{\partial^2 \mathcal{E}}{\partial t^2} = \mu_0 \frac{\partial^2 \mathcal{P}}{\partial t^2}, \tag{7.1}$$

$$\frac{dN}{dt} + \gamma_\parallel (N + N_0 + N_t) - \mathbf{P} = \frac{2i}{\hbar}(\mathcal{E}^*\mathcal{P} - \mathcal{E}\mathcal{P}^*), \tag{7.2}$$

$$\frac{d\mathcal{P}}{dt} = -(\gamma_\perp + i\omega)\mathcal{P} + \frac{i|p|^2}{\hbar}\mathcal{E}N, \tag{7.3}$$

where μ_0 is the magnetic permeability of the fiber, $\gamma_\parallel$ is the relaxation time or decay rate, ~ 0.01 s for Er^{3+} ions, $\gamma_\perp$ is the dephasing rate, ω is the center cavity frequency, N_t is the total number of ions per unit length in the medium, and p is the dipole moment of the ions. We can write the electric field and polarization as:

$$\mathcal{E} = E(z,t)e^{i(wt-\beta z)} \tag{7.4}$$

$$\mathcal{P} = P(z,t)e^{i(wt-\beta z)}, \tag{7.5}$$

where $E(z,t)$ and $P(z,t)$ are the complex slowly varying electric field and polarization, respectively.

We can now obtain a new equation for the electric field,

$$\frac{\partial^2 E}{\partial z^2} - 2i\beta\frac{\partial E}{\partial z} - \beta^2 E - \frac{1}{c^2}\frac{\partial^2 E}{\partial t^2} - \frac{2i\omega}{c^2}\frac{\partial E}{\partial t} + \frac{\omega^2}{c^2}E = \mu_0\frac{\partial^2 P}{\partial t^2} - 2i\omega\mu_0\frac{\partial P}{\partial t} - \omega^2\mu_0 P. \tag{7.6}$$

Since $E(z,t)$ and $P(z,t)$ are slowly varying, we can apply the slowly varying wave approximation and obtain a new version of Eq.(7.6),

$$-2i\beta\frac{\partial E}{\partial z} - \frac{2i\omega}{c^2}\frac{\partial E}{\partial t} = -\omega^2\mu_0 P, \tag{7.7}$$

or

$$\frac{\partial E}{\partial z} + \frac{\omega}{\beta c^2}\frac{\partial E}{\partial t} = -\frac{i\omega^2\mu_0}{2\beta}P = -\frac{i\mu_0\omega c}{2}P. \tag{7.8}$$

Since $c = \omega/\beta$, this reduces to,

$$\frac{\partial E}{\partial z} + \frac{1}{c}\frac{\partial E}{\partial t} = \frac{-i\mu_0 c}{2}P, \tag{7.9}$$

which becomes our new equation for the amplitude of the electric field.

We now focus our attention on Eq.(7.3), and substitute our equation for $\mathcal{P}$, or Eq.(7.5), and obtain,

$$\frac{dP}{dt} = -(\gamma_\perp + i\Delta\omega)P + \frac{i|p|^2}{\hbar}EN, \tag{7.10}$$

where $\Delta\omega = \omega - \omega_0$ is the detuning away from the center cavity frequency, and look for the steady state value, or where $dP/dt = 0$. This occurs for

$$P_{eq} = \frac{i|p|^2}{\hbar}\frac{1}{(\gamma_\perp + i\Delta\omega)}EN. \tag{7.11}$$

If we substitute Eq.(7.11) into Eq.(7.9), we find,

$$\frac{\partial E}{\partial z} + \frac{1}{c}\frac{\partial E}{\partial t} = \frac{\mu_0\omega c|p|^2\gamma_\perp}{2\hbar(\gamma_\perp^2 + \Delta\omega^2)}(1 - i\alpha)EN, \tag{7.12}$$

where $\alpha = \Delta\omega/\gamma_\perp$.

We can also substitute Eq.(7.11) into Eq.(7.3) and obtain a new expression for the population inversion,

$$\frac{dN}{dt} + \gamma_\parallel(N + N_0 + N_t) - \mathbf{P} = \frac{2i}{\hbar}|E|^2\left[\frac{2i|p|^2\gamma_\perp}{\hbar(\gamma_\perp^2 + \Delta\omega^2)}\right]N. \tag{7.13}$$

Therefore, the equations now read,

$$c\frac{\partial E}{\partial z} + \frac{\partial E}{\partial t} = \frac{1}{2\epsilon}\frac{\omega|p|^2\gamma_\perp}{\hbar(\gamma_\perp^2 + \Delta\omega^2)}(1 - i\alpha)EN, \tag{7.14}$$

$$\frac{dN}{dt} + \gamma_\parallel(N + N_0 + N_t) = \frac{-4}{\hbar\omega}|E|^2\left[\frac{\omega|p|^2\gamma_\perp}{\hbar(\gamma_\perp^2 + \Delta\omega^2)}\right]N, \tag{7.15}$$

where ϵ is the permittivity of the fused silica medium.

In order to simplify the equations, we define the parameter,

$$a = \frac{\omega|p|^2\gamma_\perp}{\epsilon\hbar c(\gamma_\perp^2 + \Delta\omega^2)}, \tag{7.16}$$

so that the equations become,

$$\frac{\partial E}{\partial t} = -c\frac{\partial E}{\partial z} + \frac{c}{2}a(1 - i\alpha)EN, \tag{7.17}$$

$$\frac{dN}{dt} = \mathbf{P} - \gamma_{\parallel}(N + N_0 + N_t) - \frac{4\epsilon c}{\hbar\omega}|E|^2\,aN. \tag{7.18}$$

We now change our frame of reference into one that rotates with the light circulating in the cavity. Mathematically, this looks like,

$$\tau \equiv t - \frac{z}{c}, \tag{7.19}$$

so that the field equation becomes

$$\frac{\partial E(z, \tau + z/c)}{\partial z} = \frac{ac}{2}(1 - i\alpha)E(z, \tau + z/c)N(z, \tau + z/c). \tag{7.20}$$

Now, we integrate over the length of active fiber, L_A and obtain,

$$E(L_A, \tau + L_A/c) = E(0, \tau)\exp\left[\frac{ac}{2}W(\tau + L_A/c)(1 - i\alpha)\right], \tag{7.21}$$

where $W(\tau + L_A/c) = \int_0^{L_A} N(\tau + L_A/c)dz$. Also, we can write the equation for the integrated population inversion as,

$$\frac{dW(\tau + L_A/c)}{d(\tau + L_A/c)} = \mathbf{P}L_A - \gamma_{\parallel}(W + W_0 + W_t) - \frac{4\epsilon c}{\hbar\omega}|E(0, \tau + L_A/c)|^2\left(\exp[aW(\tau + L_A/c)] - 1\right). \tag{7.22}$$

Since we have a ring cavity, we can relate $E(0, \tau + L_A/c)$ to $E(L_A, \tau - (L - L_A)/c)$, where $L = L_A + L_P$ is the total cavity length, by

$$E(0, \tau + L_A/c) = Re^{i\Delta\phi}E(L_A, \tau - (L - L_A)/c). \tag{7.23}$$

$Re^{i\Delta\phi}$ is the return coefficient in the cavity, accounting for cavity losses, multiplied by a phase factor to account for the net birefringence of the fiber. Therefore, the electric field equation becomes,

$$E(L_A, \tau + L_A/c) = RE(L_A, \tau + L_A/c - L/c)\exp\left[\frac{ac}{2}W(\tau + L_A/c)(1 - i\alpha) + i\Delta\phi\right]. \tag{7.24}$$

We can now redefine $t = \tau + L_A/c$ and define a new delay time, $\tau_R = L/c$, so that the equations become,

$$E(t) = RE(t - \tau) \exp[\frac{ac}{2}(1 - i\alpha)W(t) + i\Delta\phi], \qquad (7.25)$$

$$\frac{dW}{dt} = \mathbf{P} - \gamma_{\parallel}(W + W_0 + W_t) - \frac{4\epsilon c}{\hbar\omega}|E(0, \tau + L_A/c)|^2 (\exp[aW(t)] - 1). \qquad (7.26)$$

We now define,

$$\psi(t) = E(t)\sqrt{\frac{4\epsilon c}{\hbar\omega W_0}} \qquad \text{and} \qquad (7.27)$$

$$\Phi(t) = \frac{W(t)}{\gamma_{\parallel}W_0},$$

where $W_0 = N_0 L_A$.

Therefore, our final equations are,

$$\psi(t) = R\psi(t - \tau) \exp[\frac{ac}{2}(1 - i\alpha)W_0\Phi(t) + i\Delta\phi] \qquad \text{and} \qquad (7.28)$$

$$\frac{d\Phi}{dt} = q - 1 - \Phi(t) - |\psi(t)|^2 \left\{\exp(\gamma_{\parallel}aW_0\Phi(t)) - 1\right\}, \qquad (7.29)$$

where $q = \frac{\mathbf{P}L_A}{\gamma_{\parallel}W_0} - \frac{W_t}{W_0}$.

These are the basic equations that simulate a single polarization mode in a single ring laser. In order to simulate two coupled ring lasers, we must utilize two sets of these equations and an electric field coupling term. For ease of presentation, we will redefine $\psi(t)$ as $E(t)$ and $\Phi(t)$ as $W(t)$. Therefore, our model equations, including coupling, are,

$$E_{1,2}(t) = R\exp[\Gamma(1 - i\alpha)W_{1,2} + i\Delta\phi] E_{1,2}^{\text{fdb}}(t) + \xi_{1,2}(t), \qquad (7.30)$$

$$\frac{dW_{1,2}}{dt} = q - 1 - W_{1,2}(t) - |E_{1,2}^{\text{fdb}}(t)|^2 \left\{\exp[2\Gamma W_{1,2}(t)] - 1\right\}. \qquad (7.31)$$

The feedback term $E_{1,2}^{\text{fdb}}(t)$ is given by

$$E_{1,2}^{\text{fdb}}(t) = E_{1,2}(t - \tau_R) + \kappa_{1,2}E_{2,1}(t - \tau_c), \qquad (7.32)$$

symbol	parameter	value
α	normalized detuning	0.0352
a	material gain	$2.03 \times 10^{-23}\ m^2$
N_0	Transparency inversion	$10^{23}\ m^{-3}$
n	index of refraction	1.44
λ	center lasing wavelength	$1.55 \times 10^{-6}\ \mu m$
L_A	length of active fiber	15 m
L_p	length of passive fiber	27 m
D	intensity of white Gaussian noise	10^{-5}
R	return coefficient	0.4
q	normalized pump parameter	100

Table 7.1: Parameter values common to both transmitter and receiver.

where the subindices 1 and 2 denote Laser 1 and Laser 2, respectively, τ_R is the round trip time of the cavity, and τ_c is the travel time between the two lasers, $\Gamma = \frac{1}{2}aW_0$, and $\Delta\phi = 2\pi n L_P/\lambda$. Time is measured in units of the decay time of the atomic transition, $\gamma_\parallel \sim 0.01$s. $\xi(t)$ is white Gaussian noise with zero mean and intensity D. The feedback term [Eq.(7.32)] contains two contributions, one coming from the same laser and delayed by the cavity round-trip time τ_R, and another coming from the other laser, delayed by the travel time between the two lasers τ_c and quantified by the coupling strength $\kappa_{t,r}$, as defined in Chapter 7. However, phase modulation and birefringence defects in the fiber are not accounted for in the simulated coupling term. The delay times correspond to their experimental values $\tau_R = 220$ ns and $\tau_c = 45$ ns and the coupling strength, κ, was varied from 0.114% to 2.28%. The values of the parameters common to both lasers can be found

in Table 7.1. A detailed description and derivation of the model can be found in Refs. [64, 72].

7.2   Model Results

With the parameters set as shown in the previous section, we see very good correspondence between the model and the experiment. The pump rate used in all simulations presented is approximately five times threshold as it is in the experiment. The noise parameter was adjusted so that the threshold for synchronization in the model matched that in the experiments. Time series were recorded at different coupling strengths and were compared to experimental time series at the same coupling strength.   Figure 7.1 is a comparison of the model and experimental time series at two different coupling strengths. The ratio of the standard deviation of the fluctuations to the mean is similar for both cases. This can be better seen in Fig. 7.2, where the standard deviation normalized to the mean is shown for both the experiment and the simulations. The simulations match very closely to the experiment, except at the extreme lowest coupling strengths.

As in the experiment, the simulation shows a threshold for synchronization around $\kappa = 1.14\%$.   Figure 7.3 shows the synchronization error as a function of the coupling strength for both the model and the experiment. They are in agreement except for at the lowest coupling strengths. The model was also tested with delays that were much longer than the round trip time and the results were again in agreement with the experiment.

Figures 7.4 and 7.5 are the spatiotemporal representations of the numerical simulation time series uncoupled and with 2.28% coupling. The number of round trips plotted spatiotemporally is 200, which is one tenth of the number plotted on the experimental plots. The number of round trips is limited in the simulation by the computational time.
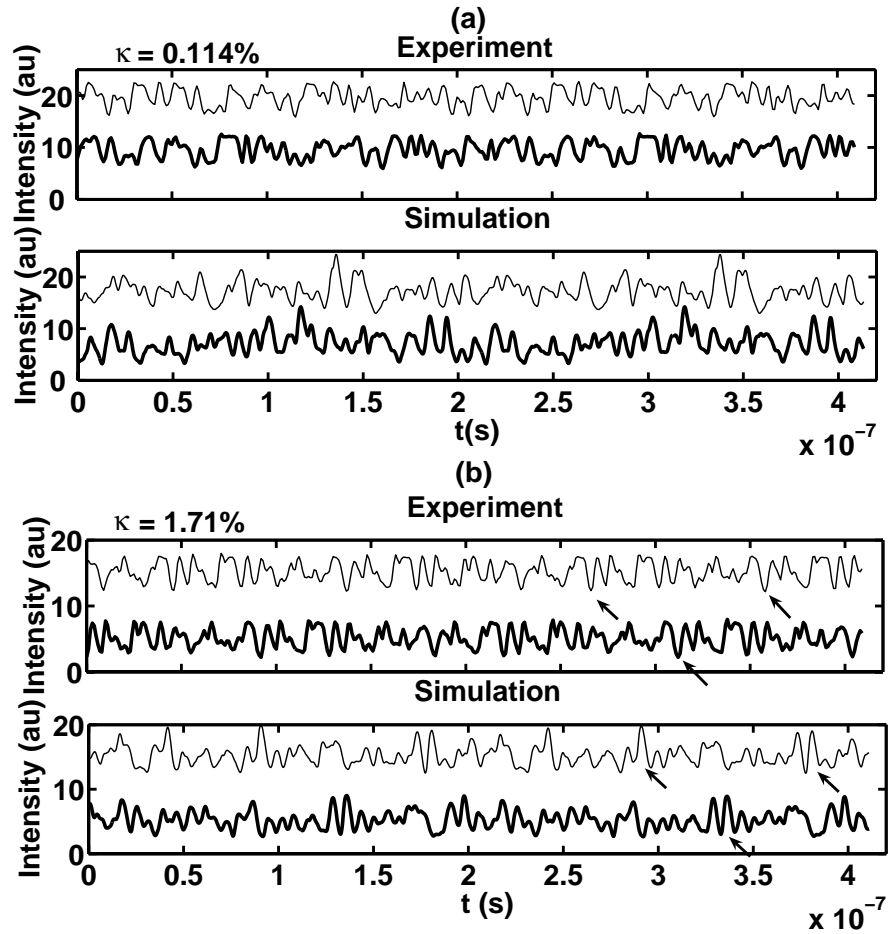
Figure 7.1: Intensity time series for approximately two round trips of two mutually coupled fiber ring lasers. Laser 1 is the thick line and Laser 2 is the thin line. (a) The experimental and numerical time series for coupling strength, $\kappa = 0.114\%$. The time series are not synchronized. (c) The experimental and numerical time series for $\kappa = 1.17\%$. The time series are synchronized with a 45 ns offset. The arrows represent where the time series line up with a 45 ns offset in either direction
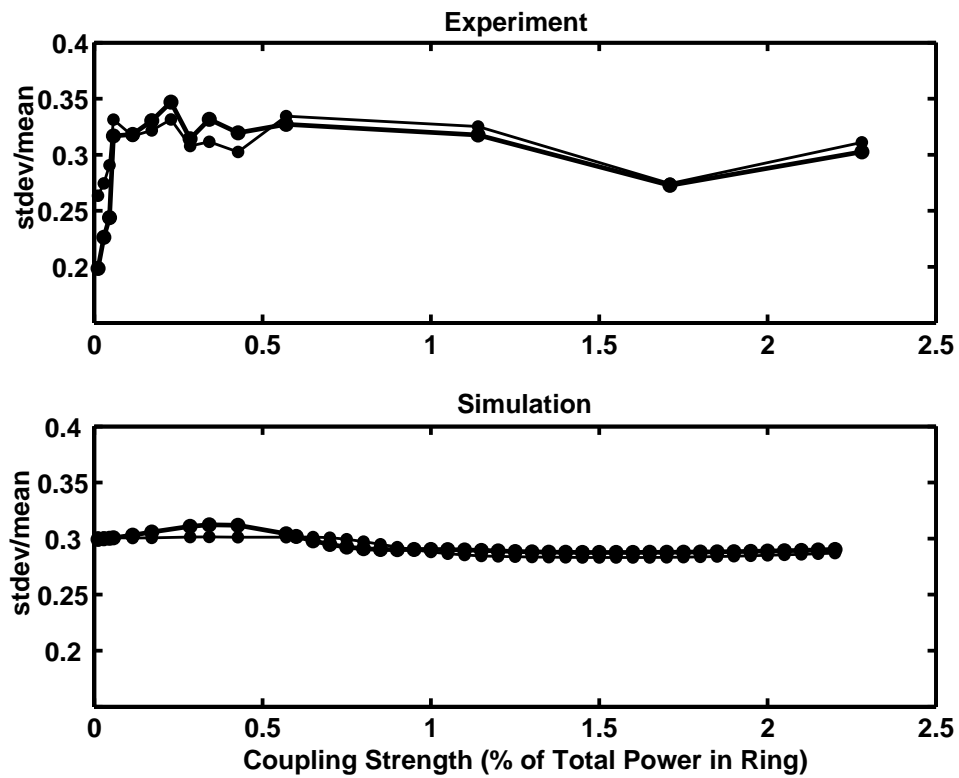
Figure 7.2: Standard deviation normalized to the mean for both the experiment and numerical simulations. Note the agreement for all but the extreme lowest coupling strengths.
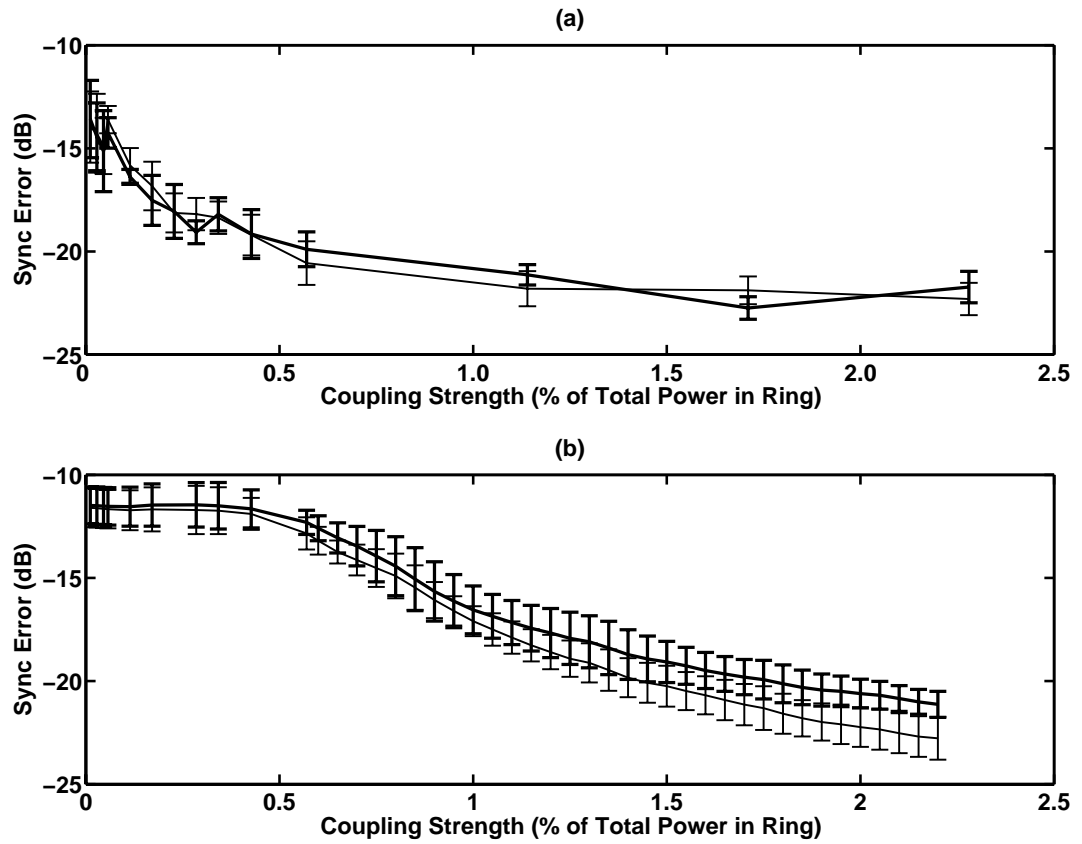
Figure 7.3: Synchronization error vs coupling strength for (a) experiment and (b) numerical simulations. Each point was averaged over 10 runs and the error bars represent one standard deviation from the mean
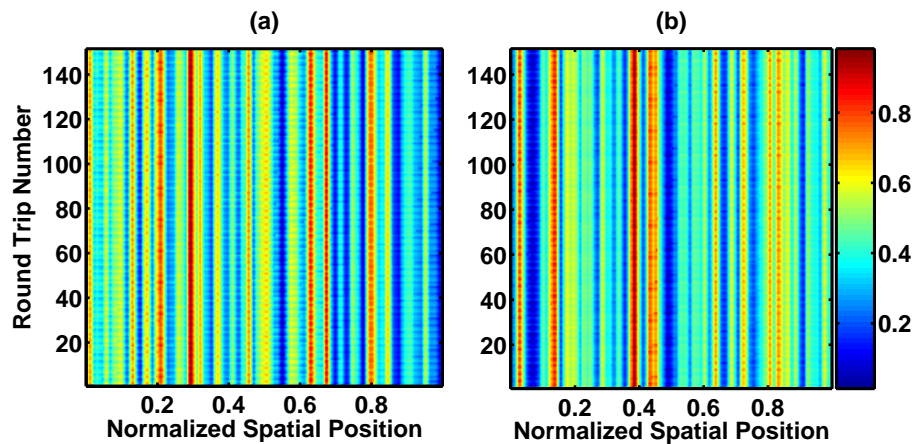
Figure 7.4: Spatiotemporal representation of the numerical time series; the color represents intensity in arbitrary units, the spatial position is normalized to one round trip in the fiber ring. (a) Uncoupled Laser 1 (b) Uncoupled Laser 2
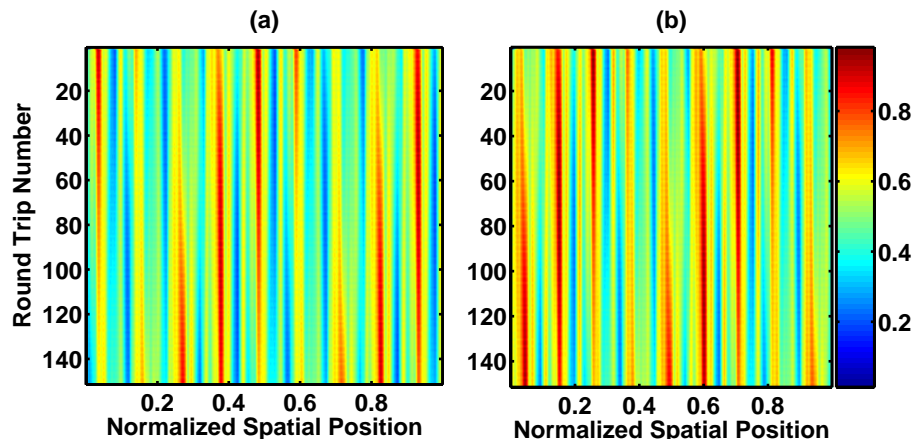
Figure 7.5: Spatiotemporal representation of the experimental time series; the color represents intensity in arbitrary units, the spatial position is normalized to one round trip in the fiber ring. (a) Mutually coupled Laser 1, $\kappa = 2.28\%$ (b) Mutually coupled Laser 2, $\kappa = 2.28\%$[72].

Figs. 7.4(a) and (b) are solitary Lasers 1 and 2, respectively. Figs. 7.5(a) and (b) are coupled Lasers 1 and 2, respectively, with a coupling strength of $\kappa = 2.28\%$.

It is difficult to determine which laser is leading and which laser is following, as shown in Fig. 7.3, like it is in the experiment. The arrows in Fig. 7.1 show where the two time series line up with two offsets corresponding to the travel time, in both the experimental and numerical results. However, if we view the model in the same spatiotemporal configuration as the experiment, we again observe switching.

7.3 Conclusions

A delay-differential equation model has successfully been developed to simulate the behavior of coupled EDFRL's. There is qualitative agreement in the intensity output between the experiment and the numerical simulations. The simulations display synchronization at the same coupling strength as in the experiment. This model can now be used to investigate dynamics unique to coupled ring laser systems.

Chapter 8

Communicating with the EDFRLs

Communicating with chaos has been a popular area of study since the early 1990's. Generally, two identical dynamical systems are coupled together and their synchronized chaotic output is used as a carrier wave for communications. This scheme was tested on a variety of systems with coupled electronic chaotic circuits[20] and with coupled lasers, including optically unidirectionally coupled fiber ring lasers[52, 53, 54]. However, it was found in those experiments, as in the present one, that two closed loop EDFRLs are very difficult to synchronize. In fact, in order to make a system for communications, a closed loop EDFRL was coupled unidirectionally to an open loop amplifier with a proper time delay[52, 53, 54]. In this experiment, we make use of the synchronization achieved through mutual coupling to use two closed loop EDFRLs for chaotic communication. Though the signals are now sent in both directions, no longer allowing the system to be secure, this type of system lends great insight into how high dimensional systems communicate.

8.1 Message Injected into the Ring

8.1.1 Experimental Setup

The experimental setup for the communications experiments was the same as for the synchronization experiments with a few additions. Unless otherwise indicated, the coupling strength is 2.28% for each laser. In all experiments, a JDS Uniphase Mach-Zender type electro-optic modulator was driven by an Agilent B1130A Pulse-Pattern generator and used to control the output of an optical source. The optical source used in this experi-

ment was a Photonetics Tunics-BT narrow linewidth tunable laser. After passing through the EOM, the bits were amplified by a JDS Uniphase optical amplifier which consists of an EDFA pumped at 980 nm, similar to the active medium in the ring lasers. The mutually coupled EDFRLs were adjusted to fluctuate around the a center peak near 1550 nm using the polarization controllers. The bit amplitude, width, wavelength and frequency were varied. The experimental setup is shown in Fig. 8.1.

In the first experiment presented herein, the bits were injected directly into the laser cavity of Laser 2 through the 95/5 evanescent coupler as shown in Fig. 8.1. In this configuration, when a single bit is injected into the ring, it propagates through the cavity multiple times as it rings down. The message then propagates through the coupling lines into the second ring laser where it is immediately filtered out, and we can decode the messages through simple subtraction. It should be noted that in all of the experiments presented in this chapter, we use simple time series subtraction with a correct offset to decode the messages rather than filtering techniques that have been used previously in ring lasers[52, 53, 54, 55]. Therefore, we can in principle use a very fast bit rate. However, the detectors that we are using filter out bit rates greater than 125 MHz and sets the upper limit in these experiments.

8.1.2 Experimental Results

ASCII bit streams of four and five characters were tested, and in this configuration single bits will also be presented to illustrate the issue of the slow cavity ring down. Figure 8.2(a) shows the time series with the bit injected into Laser 2, where the blue curve is the transmitter and the red curve is the receiver. It is not obvious where the bits are in this figure, however. Figure 8.2(b) shows the subtraction of the transmitter and receiver
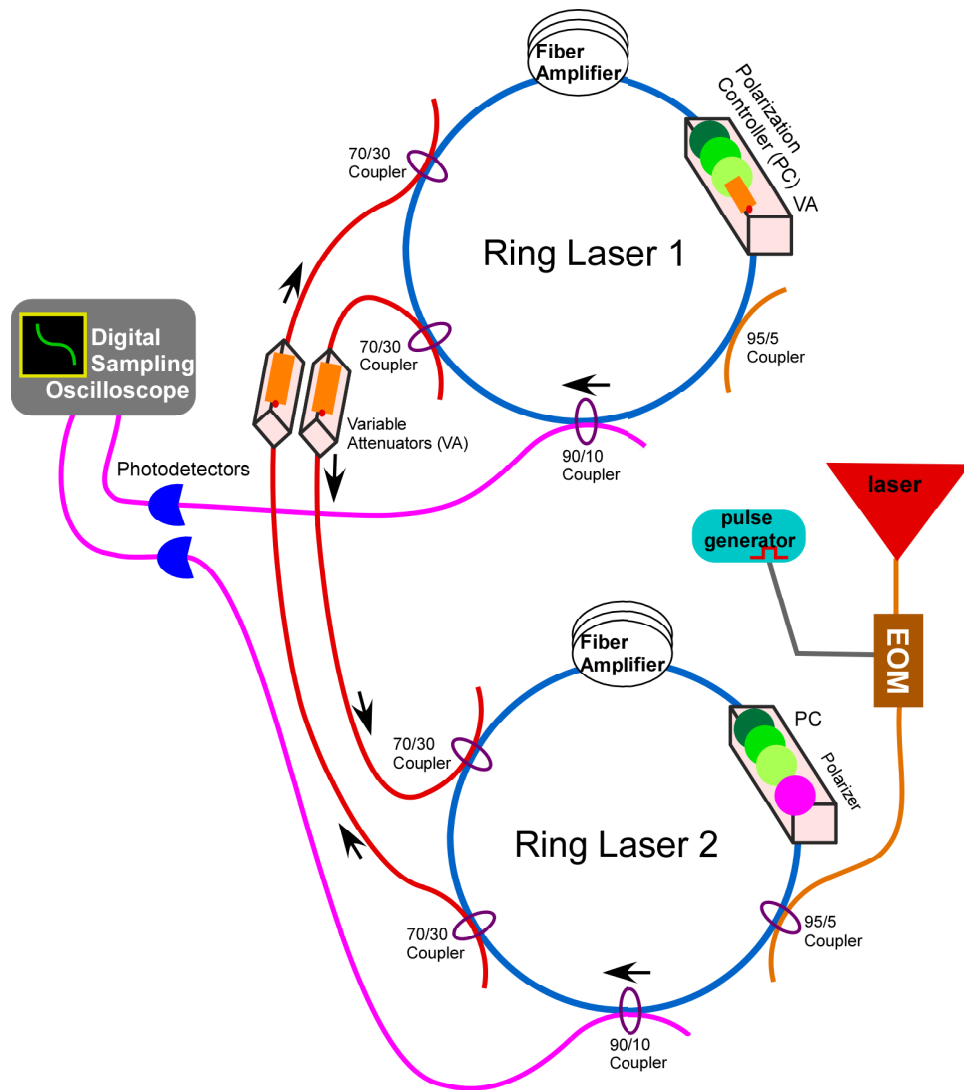
Figure 8.1: Experimental setup for the injection of bits into the cavity, the order of the components has been rearranged from the synchronization experiments for convenience, and the EOM is the electro-optic modulator.[79]
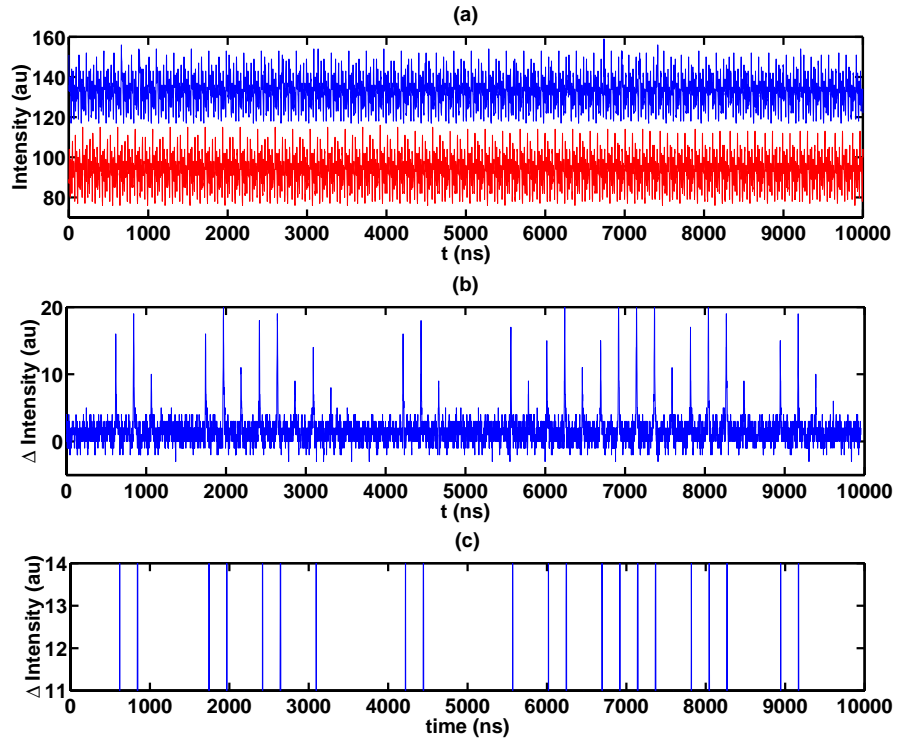
Figure 8.2: Experimental data showing full message masking and recovery when the bits are injected into the cavity. (a) are the intensity time series of the transmitter (blue) and receiver (red) lasers. The bit stream is not visible in this time series. (b) is the subtraction with the correct offset of the receiver intensity from the transmitter intensity, both bits and ring down are visible, they are not with any other offset. (c) At intensities higher than the cutoff, the bits alone are visible and the message can be recovered.[79]
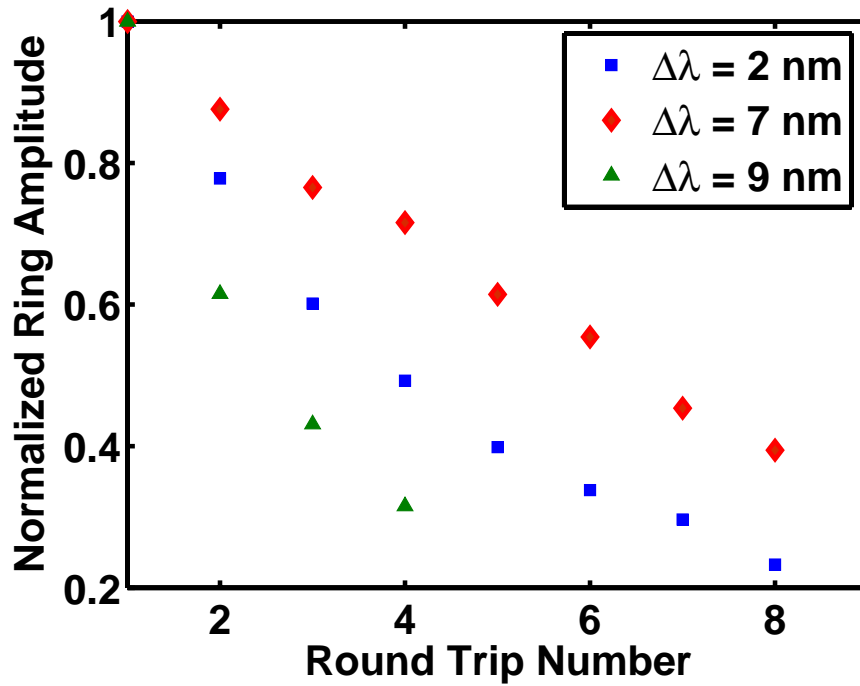
Figure 8.3: Ring down amplitude versus number of round trips for various detunings of the message wavelength to the center lasing wavelength.[79]

laser. The bits are now evident in the subtracted time series. We now assign a threshold for message recovery, above which we assume the fluctuations are bits, and below which we assume the fluctuations are due to the chaotic carrier or the ring down of previous bits. In Fig. 8.2(b) this threshold is at an intensity value of 11[80]. Figure 8.2(c) shows the bits after the cutoff. The ASCII word represented here is Chaos. Even though we can recover the message, the threshold is relatively high due to the ring down.

The ring down was characterized as a function of time, measured in units of one round trip, and shown in Fig. 8.3. It was found that the decay follows a power law rate that depends on the proximity of injected wavelength to the center lasing wavelength of the coupled EDFRLs. This is intuitive because the further away from the center lasing wavelength it is, the less the amount of power the cavity gives to it, and the more quickly
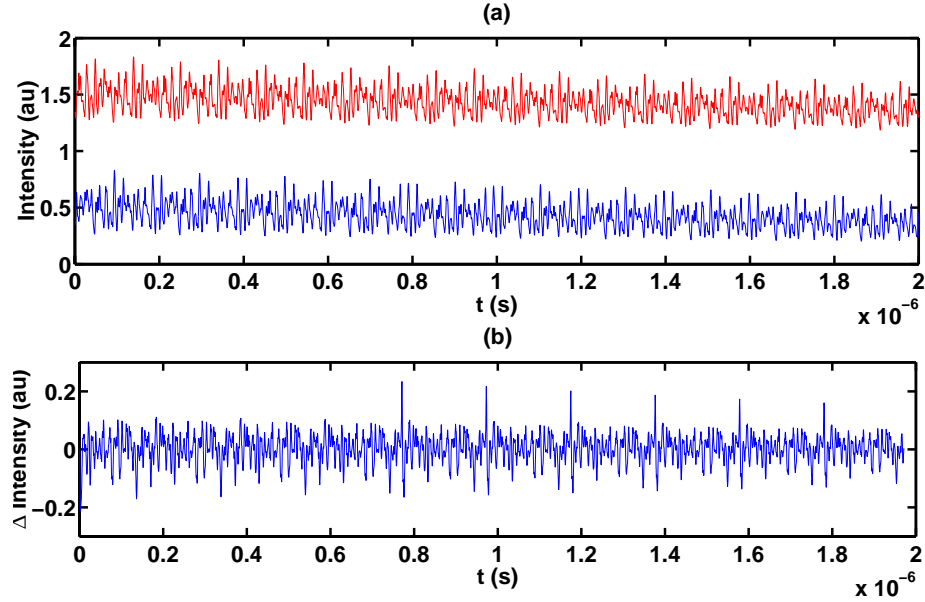
Figure 8.4: Simulated injection into the cavity. (a) are the intensity time series of the transmitter (blue) and receiver (red) lasers. The bit is not visible in the time series. (b) Subtraction of the receiver time series from the transmitter, the bit and the ring down are both visible. The ring down occurs with a period of the round trip time.[79]

it is damped out. In Fig. 8.3 we see the difference in the power law decays for three injection wavelengths with different detunings from the EDFRL lasing peaks, which are at ∼1550 nm.

8.1.3 Numerical Results

The message injection into the ring was also simulated using the numerical model described in Chapter 8. In these simulations, bits were injected into the ring as in the experiments. Figure 8.4(a) shows the simulated time series with a single bit injected into the transmitter laser cavity. Again, the bit is completely masked by the chaos and does not appear in the receiver time series. Figure 8.4(b) shows the subtraction of the time series. The bit and the ring down are now visible, like they were in the experiment. The period of the ring

down bits is equal to the cavity round trip time of the laser in both the experiment and the simulations.

8.2 Message Injection into the Coupling Lines

8.2.1 Experimental Setup

In the second communications experiment, the bit was injected into the coupling line rather than into the ring, and was masked by the chaos. This allowed us to use a smaller bit amplitude and greater bit frequency because there was no ring down. Figure 8.5 shows the experimental setup for injection into the coupling line. The same setup was used to generate the bits, however, now they are injected into the input ports of the couplers that are used for monitoring the power in the coupling lines. Bits were created in the manner explained above, and injected into the fiber that sends light from Laser 2 into Laser 1.

The setup was then modified to include only a single injection line with counter-propagating light. This does not affect the synchronization of the lasers or communication between them.   The experimental setup for this is shown in Fig. 8.6. Since an additional evanescent coupler was necessary, the travel time between the two lasers increased to $\sim$70 ns. The experiments presented in this section were performed with a single coupling line.

8.2.2 Experimental Results

Figure 8.7(a) shows both the coupling line with the message masked and the receive laser time series. The difference in the standard deviations is due to the coupling line only carrying 30% of the light circulating within Laser 2. The bits are not visible in the time series. The second panel, Fig. 8.7(b) shows the two time series with normalized standard
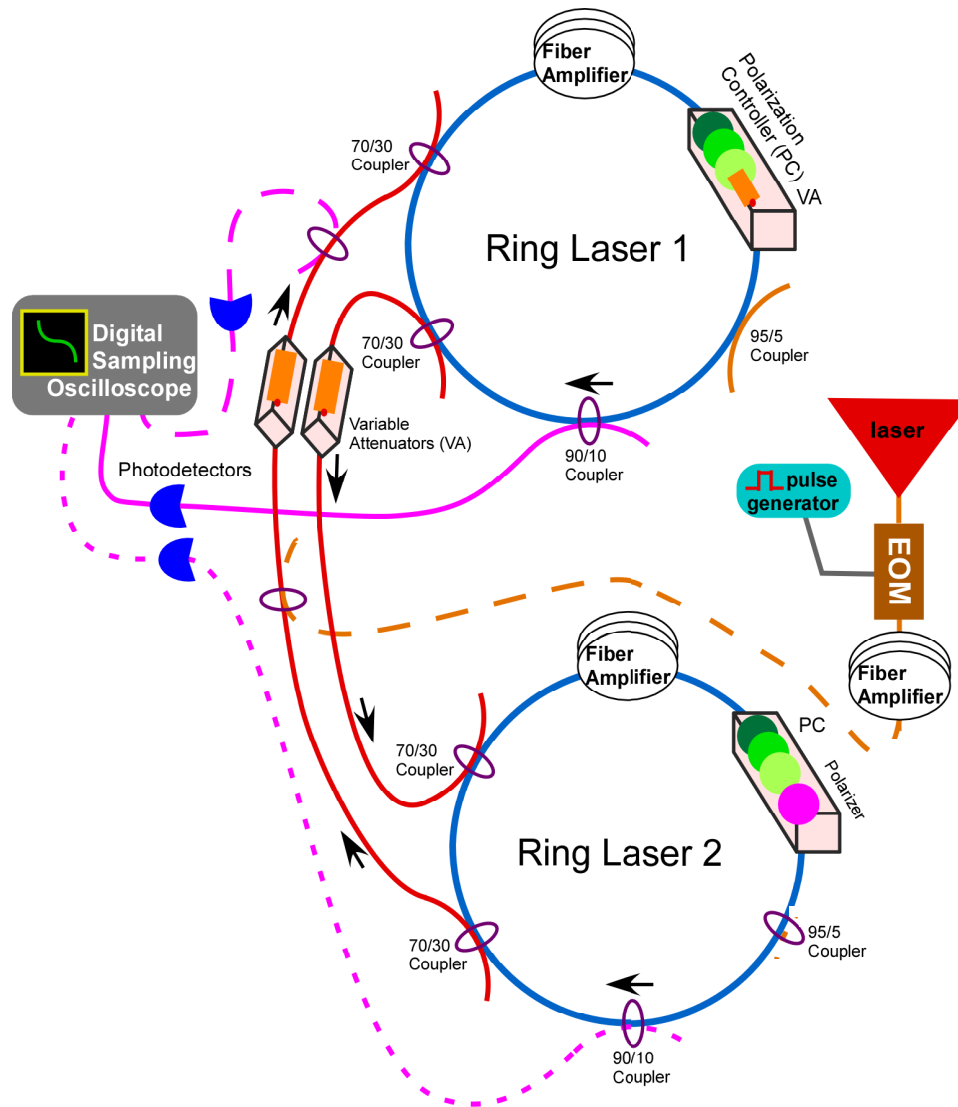
Figure 8.5: Experimental setup of injection of bits into the coupling lines, EOM is the electro-optic modulator.[79]
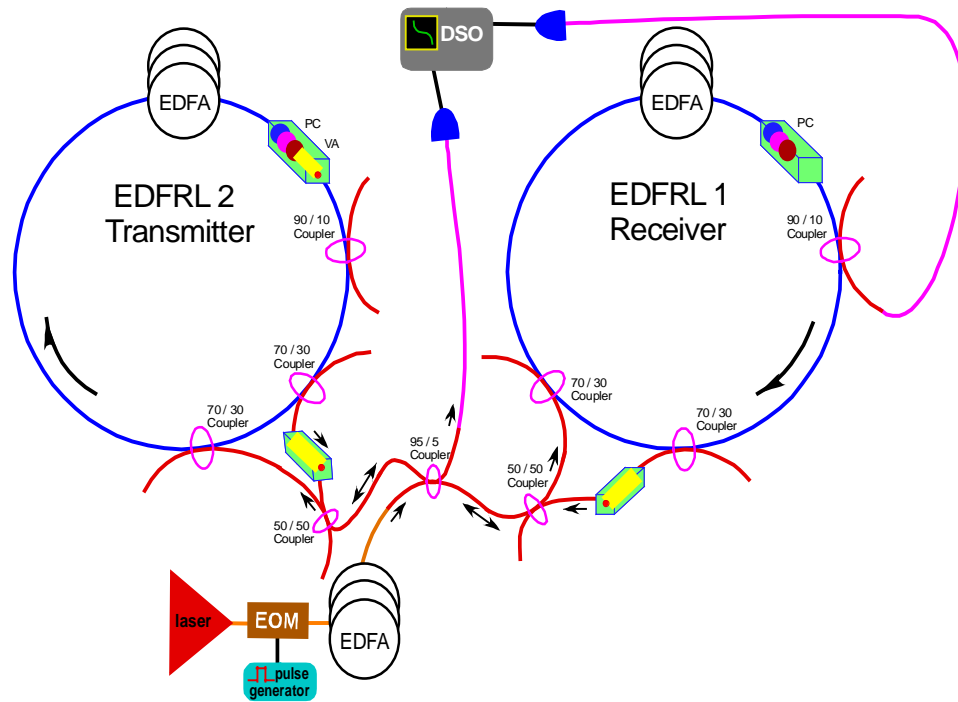
Figure 8.6: Experimental setup with a single coupling line, light travels in both directions through the same fiber, EOM is the electro-optic modulator. Bits are injected into the coupling line. Again, without the correct offset, the bits are not visible.[79]
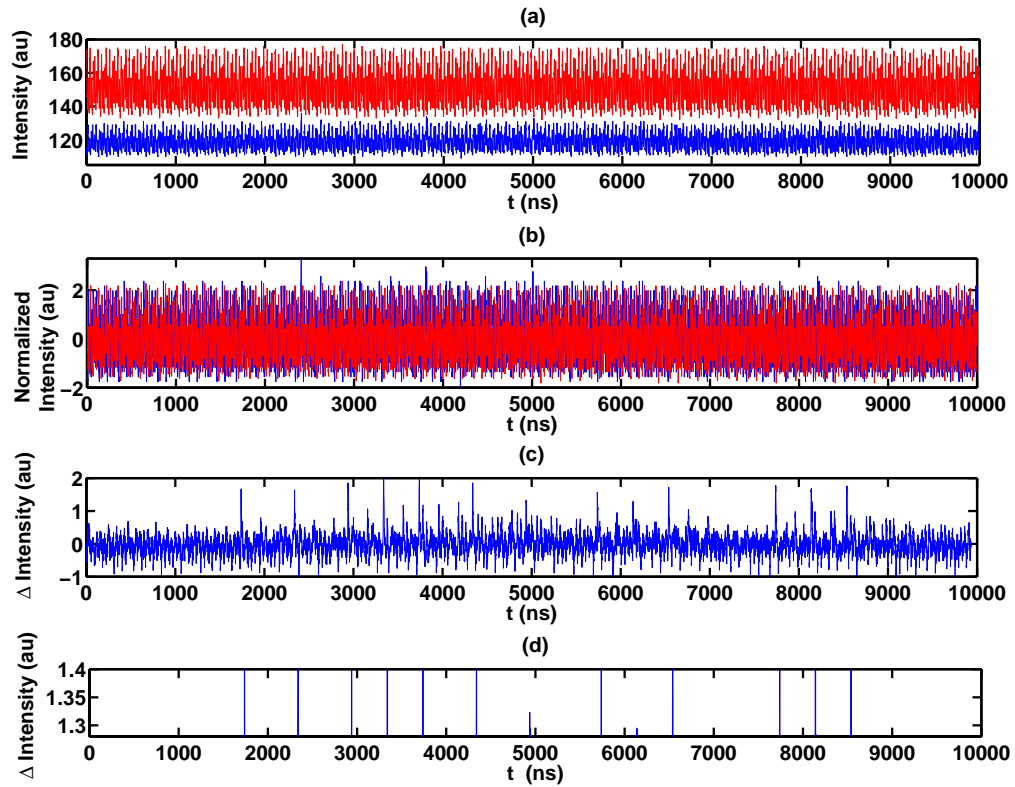
Figure 8.7: Experimental injection of bits into the coupling line. (a) Time series of the injection line from the transmitter (blue) and the receive laser (red). (b) Injection line intensity (blue) and receiver laser intensity (red) normalized, the bits are not visible in the transmitter. (c) Subtraction of the receiver laser intensity from the normalized injection line intensity, the bits are now visible. (d) The subtracted bits above the cutoff intensity. The word IREAP is now visible.[79]
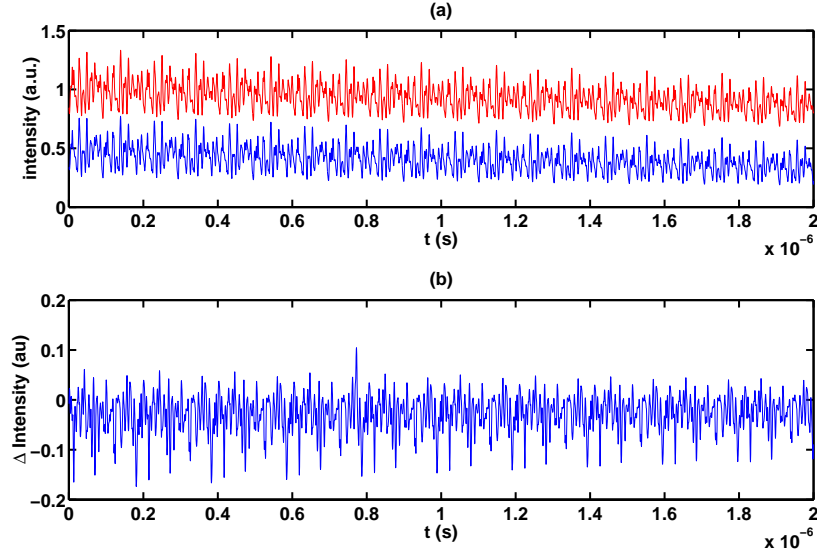
Figure 8.8: Numerical simulation of bits injected into the coupling line. (a) blue is the coupling line and red is the receiver, No bits are visible in the coupling line. (b) is the subtraction of the receiver signal from the normalized coupling line signal. The bit is now visible at $\sim 0.799 \times 10^{-2}$s.[79]

deviations. Again, the bits are not visible. Figure 8.7(c) shows the difference taken now with an appropriate time delay, and the bits are clearly visible. Figure 8.7(c) shows the bits when viewed above the threshold, which is 1.3 au, and since we are all familiar with ASCII, it is obvious that it says IREAP. The drawback to this method is that the injected bits must have a very small amplitude because the amount of light propagating within the coupling line is much less than the amplitude of the light within the cavity. Therefore, when we recover the message, we are very near the noise level of the signal.

8.2.3 Numerical Simulations

This scheme was also tested in the numerical simulations. Once again, a single bit was injected into the coupling line as was done in the experiment. Figure 8.8 shows the normalized intensity time series of the injection line and the receive laser. The bit is not visible in the injection line time series. Fig. 8.8 is the subtraction of the two time series,
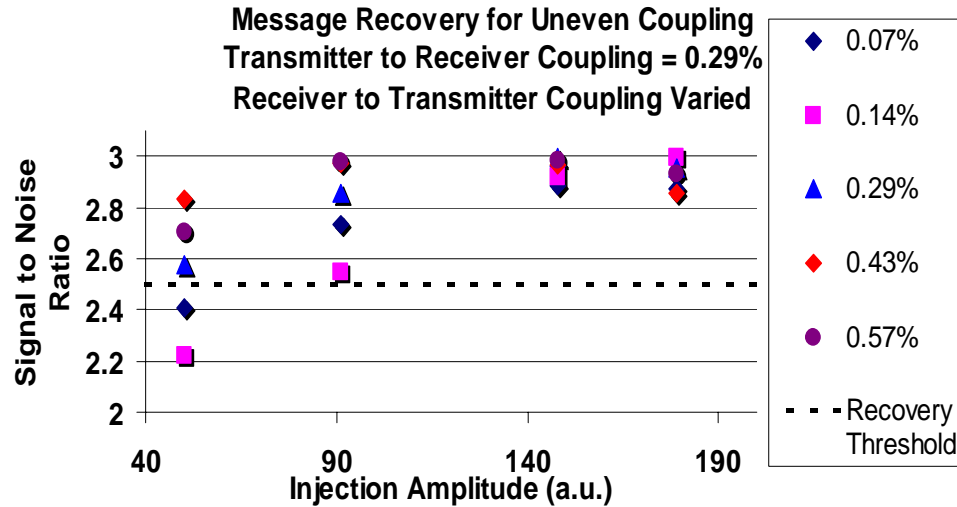
Figure 8.9: Signal to noise ratio versus injection amplitude for various coupling strengths. The dashed line is the threshold for message recovery. As the coupling strength increases, the signal to noise ratio improves for smaller injection amplitudes.[79]

again with an offset, and the bit is now visible. There is no ring down in this situation.

8.3   Discussion and Conclusions

We have demonstrated several chaotic communications schemes with mutually coupled EDFRLs. Uneven mutual coupling was also tested.   Figure 8.9 shows the signal to noise ratio as a function of injection strength for different ratios of coupling strengths using the last injection method described. We see that even for uneven mutual coupling, we can easily recover messages sent from one laser to the other.

We have shown that message masking is possible in three coupling schemes and that the messages can be extracted via a simple subtraction of the two intensity-time series. This is a dramatic improvement over previous techniques that involved various methods of filtering to recover the message and does not limit the bit rate.

We have also shown the robustness of the mutually coupled ring lasers. The subtraction technique is only possible because the bit is not incorporated into the dynamics of the

receive laser. This property may lend insight into the dynamics of biological systems that rely on subtraction of signals to obtain information (i.e., neuronal signals) and mutually coupled EDFRLs may be a useful tool in studying the behavior of such systems.

Chapter 9

Spatiotemporal Chaos and Synchronization

Systems displaying high-dimensional dynamics are often difficult to control, perturb and analyze. These types of systems range from multimode laser systems to fluid systems to liquid crystals with optoelectronic feedback. All of these systems have a large number of degrees of freedom which lead to their complex dynamics. When these systems are coupled, often not enough information can be passed between them for identical synchronization to occur. This is especially true for systems with unidirectional coupling. The degrees of freedom that are not coupled from one system to the other are called hidden variables. Often these hidden variables are responsible for obtaining generalized synchronization, where there is a functional relationship between the drive and response system[81, 82, 83, 84, 85]. An example of this phenomenon occuring in a multimode laser system can be found in Ref.[4]. In this experiment the intensity from a laser was used to modulate the cavity loss of the laser system. Because the laser had two modes and the intensity of the laser was being used in the feedback loop, the actual modal information was lost, and they achieved generalized rather than identical synchronization.

The SLM allows us to investigate this property further. Because we are able to control the voltages placed across the SLM, we are able to construct a feedback loop that can perturb the system. However, because we are only able to observe the holograms using a laser, precise information about the position and momentum of the molecules in the LC is unknown. This leads to hidden degrees of freedom, or "hidden variables", in this experiment.
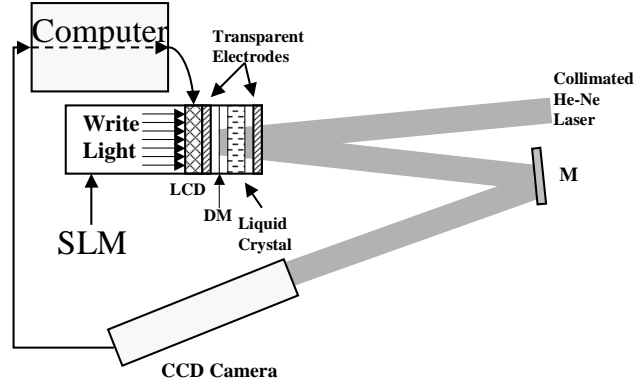
Figure 9.1: Experimental setup for generalized synchronization of spatiotemporal chaos. SLM, Spatial Light Modulator; M, mirror; LCD, Liquid Crystal Display; DM, Dielectric Mirror[86]

9.1 Generating Chaos with Liquid Crystals

We generate chaos in the liquid crystal with an experimental setup similar to that for the holography experiments with an optoelectronic feedback loop. The linearly polarized light at 633 nm from a helium-neon laser is incident on the SLM as shown in Fig. 9.1. After reflecting off of the phase grating, the beam propagates for approximately 2.5 m before it is incident on a Pulnix TM-72EX CCD camera. As described in Chapter 3, the SLM uses the VGA output to make a gray-scale pattern on the internal LCD. Though the liquid crystal is not pixilated, the LCD consists of an array of 480×480 active pixels of which the central 244×360 are used in this experiment. The image from the camera is then displayed on a computer monitor and also transferred to the SLM. The camera detects 114×180 pixels from the center of the diffracted beam and the inverted image is displayed on the array of 244×360 pixels in the center of the LCD. Therefore, we use an inverted stretched image of the central portion of our beam as the feedback signal over the utilized area of the SLM. This image is illuminated and creates a new phase grating on the liquid crystal in the same manner as was described in the previous chapters. This process is illustrated in

Fig. 9.1. The intensity pattern, created by the initial phase grating and displayed on the monitor, transforms the liquid crystal into a new phase grating which, in turn, modulates the laser beam and the process repeats, again as shown in Fig. 9.1 including the dashed arrow. This process will be referred to as the closed-loop configuration.

The closed-loop intensity patterns are recorded for approximately 17 s on a Silicon Graphics Inc. O_2 Media Recorder in Apple Quicktime formate at a rate of 30 frames/s. The resulting sequence of patterns (a movie) that is generated from the closed loop is spatiotemporally chaotic and serves as the drive signals in the unidirectionally coupled synchronization experiments.

9.2   Characterization of the Chaos and Parameters

The characteristics of the chaos that we generate depend on the bias voltage. Drive movies were recorded at bias voltages between 1.50 and 5.0 V at 0.25 V increments. If we refer to the routes to chaos presented in Chapter 3, we recall that the bias voltage plays an important role in determining the properties of the optical turbulence in liquid crystals with feedback.   Figure 9.2(a) shows a typical picture of the images that appear when the SLM is run in a closed loop. The average grain size, or the average size of the light spots on the dark background, depends on the applied bias voltage, the smallest grain size appearing at the middle bias voltage levels and the largest appearing at bias voltages closer to the minimum and maximum values. The grain sizes were determined using a two-dimensional autocorrelation function after subtracting the mean value of each image. The full width at half maximum (FWHM) was then calculated and an average grain size was extracted. The autocorrelation function and average grain size as a function of bias voltage for a variety of drive signals can be seen in Fig. 9.2(b,c), respectively.
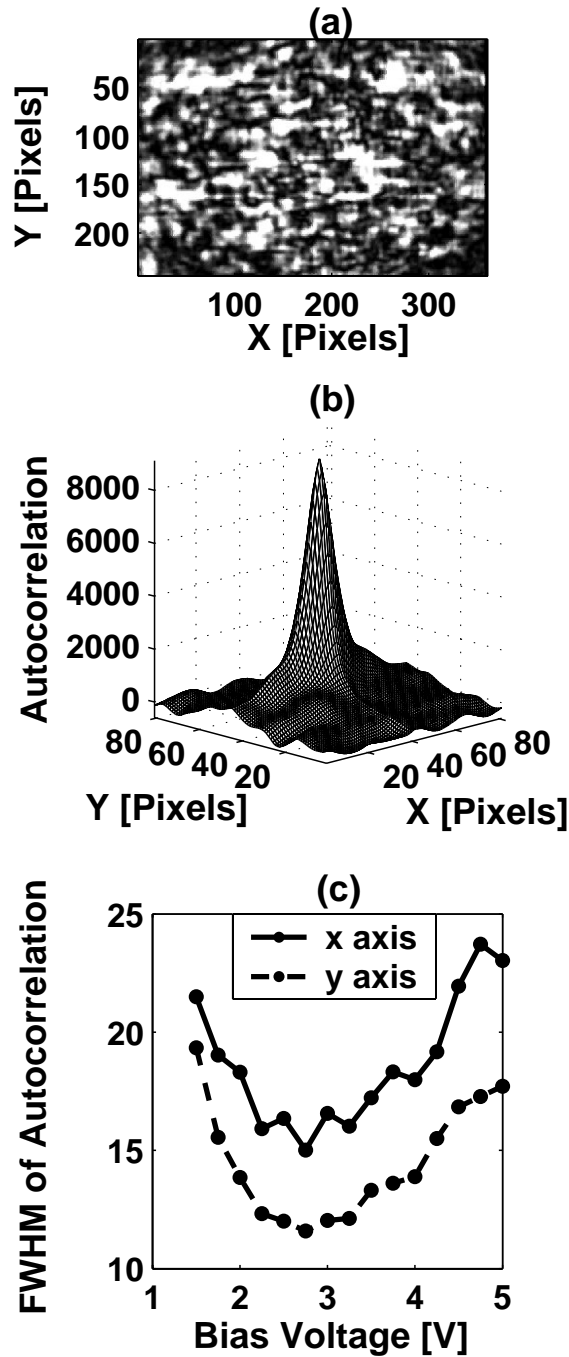
Figure 9.2: (a) is a typical far field chaotic pattern generated by the SLM in the closed loop feedback system. (b) is a 3-D plot of the autocorrelation from which we take 2-D slices at the peak in the x and y direction. We calculate the FWHM of the slices and, from this, the grain size. (c) is a plot of the average grain size in the x and y direction versus the bias voltage[86].

The time scales for the liquid crystal are approximately 30 ms for turn on (depending on the bias voltage) and approximately 40 ms for relaxation into the off state. The LCD refresh rate is 30 Hz. The pattern evolution time scale depends on the bias voltage and the refresh rate of the LCD. These time scales are all roughly comparable in the regime of operation of the experiments.

9.3 Synchronization of Chaos

In order to test for generalized synchronization using the auxiliary method, multiple copies of a system are connected through one or more degrees of freedom[16, 17, 18, 19]. Since we cannot make multiple identical copies of the experiment, we have to use a different way to test for synchronization. In our method, we record the images that are generated in the closed loop on the computer. We then break the closed loop feedback by breaking the connection in the computer, represented by the dashed line in Fig. 9.1, and a second computer is connected to the SLM. The drive movies stored on the original computer is "played" into the SLM by the second computer and the SLM response to the drive movie is recorded on the original computer.

When we compare the response movies to the drive movies we see that they are not the same, therefore, we do not see identical synchronization. In order to test for generalized synchronization we must determine if there exists a functional relationship between the drive and response. We see this experimentally buy looking at the responses of two identical systems to a drive system. In our case, several responses to the drive were recorded, each with different initial conditions. The initial conditions of each response movie were made to differ by placing a different initial frame on the drive movie each time is was played. The intensity patterns or the response movies were then compared with

(a) Drive

(b) Response 1   **(c) Response 2**
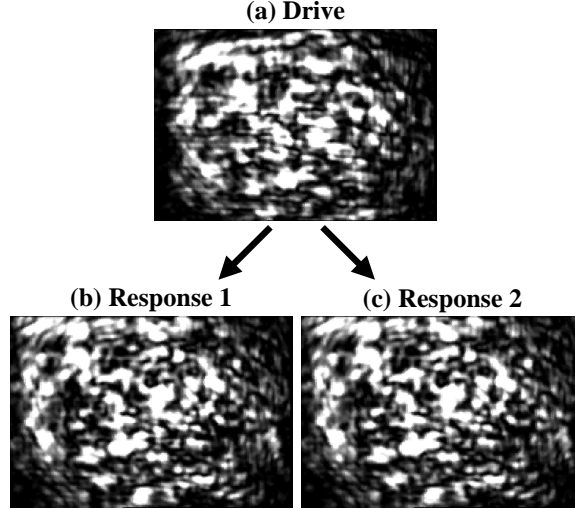
Figure 9.3: Typical far field chaotic patterns generated by the SLM in the closed loop drive system (a) and the open loop response system (b),(c), at 1.5 V bias voltage. The chaotic patterns for the two responses are well synchronized both spatially and temporally[86].

each other, frame-by-frame and pixel-by-pixel, in order to see if they were similar. The experiment was repeated for different values of the SLM bias voltage. Since all of the movies are recorded on the same setup, all images undergo the same transformations.

9.4   Results

Figure 9.3 shows typical snapshots of the drive and two response movies at the same frame number. It is evident that the drive and response images look very dissimilar but that response 1 and response 2 are nearly identical. This is consistent with generalized synchronization. The quality of the synchronization is quantified by the synchronization error. In this case, we define the synchronization error as the difference of the gray-scale values at each two-dimensional spatial location (pixel) between the images of the two response movies,

$$\langle e(x,t) \rangle = 10 \times \log_{10} \langle |[I_A(x,t) - I_B(x,t)]| \rangle \tag{9.1}$$

where the angle brackets denote space and time averaging. $I_A(x, y, t)$ and $I_B(x, y, t)$ are the normalized intensities of the two response images at the position (x,y) and the time t of the two response movies. To normalize the intensities, each frame was demeaned, and each pair that was being compared was normalized to the minimum and maximum of one of the frames in the pair. For calibration, the synchronization error was computed for the response of the SLM to the same static image at two different times and was found to be approximately -30 dB. Therefore a synchronization error of less than -25 dB is defined as the threshold for generalized synchronization.

Figure 9.4 shows the synchronization error analysis and the effect of the bias voltage on the transient time. The transient period before synchronization is a result of the mismatched initial conditions, and time is represented by the frame number of the movie. The movies analyzed were responses to a drive movie taken at a bias voltage of 1.5 V. Initially, the responses are unsynchronized, but the synchronization level increases (error decreases) with time and converges to an error of -30 dB.

The time scales of the transient behavior depend on the bias voltage. The first frame of the drive movie was changed each time the drive movies were played to the response system, but the changes in initial conditions were identical for each bias voltage. However, the system response to these changes varied depending on the bias voltage of the response system. Figures 9.4(b) and (c) show how the synchronization error depends on the bias voltage of the response system. Transient time monotonically decreases as the bias voltage increases, indicating that responses taken at high bias voltages synchronize to the drive signal more quickly than those at low bias voltages.

Generalized synchronization error after the transients was also investigated as a function of bias voltage. Figure 9.4(c) demonstrates that the synchronization error is
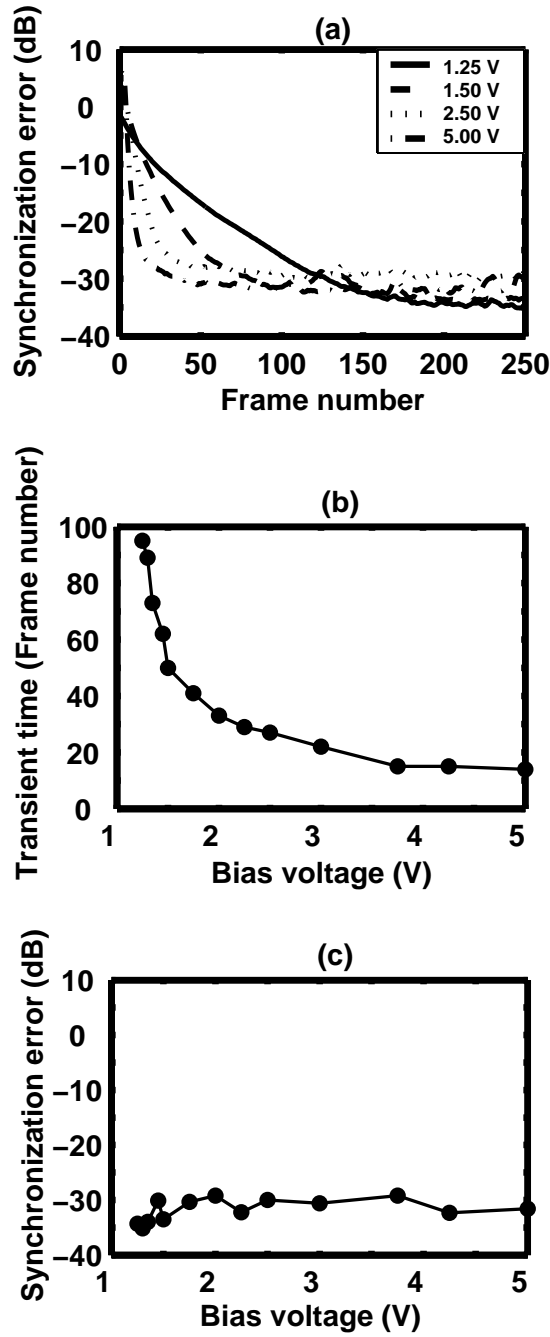
Figure 9.4: Characteristics of generalized synchronization. (a)Transients of generalized synchronization error at different bias voltages of the SLM. (b)Transient time (frame number) of generalized synchronization as a function of bias voltage. The threshold for synchronization is set at -25 dB. (c)The synchronization error at different bias voltages after the transient period[86].

approximately constant for all values of the response bias voltage once synchronization occurs. The system, therefore, reacted to the change in initial conditions differently for each bias voltage.

9.5   Discussion

Since the dynamics of the response system are repeatable, reproducible and independent of the initial conditions, generalized synchronization is stably achieved in this system. Recalling the results of the holography experiments, we know that the effect of the bias voltage on static images is one of only clarity. It does not change the overall hologram, only the clarity of it, or how much phase shift is associated with a certain gray scale level. However, when placed in the optoelectronic feedback loop, the bias voltage plays a much more active role. Tuning the bias voltage results in changes in both the quantitative and qualitative characteristics of the images formed in response to the drive movies. In the feedback experiment, changing the bias voltage also changes the speed at which the molecules respond to voltages. Therefore, the patterns obtained at each bias are dramatically different at each voltage.

This different bias voltage response also manifests itself in the varying responses of the transients at different bias voltages. These responses are evidence that the SLM is not acting as a passive filtering device, but that the generalized synchronization is a product of dynamics internal to the device. Though the liquid crystal molecules are responsive to the bias voltage, in parallel aligned liquid crystals, the molecules are only aligned along a single axis. Also, the bias voltage does not have full control over their orientation and momentum. They also feel forces from other molecules and the container. Therefore, the internal conditions that produced the drive movies are not reproducible using only

the intensity patterns formed by the phase shifts. This is one of the reasons that we see generalized synchronization and not identical synchronization. There is also a loss of information in the recorded movies at each iteration of the feedback loop due to the transformations inherent in the experimental setup. Feeding back only the center portion of the diffracted beam leads to significant loss of resolution in the spatial pattern. The final result is a recorded movie that has lost information about various spatiotemporal degrees of freedom, corresponding to "hidden" variables in the system. This is analogous to loss of modal information corresponding to hidden degrees of freedom in the experiment presented in Ref.[4].

9.6   Conclusions

In summary, we observed generalized synchronization of spatiotemporal chaos in an optoelectronic feedback system with a liquid crystal SLM. The transient characteristics of generalized synchronization depend on the bias voltage of the SLM, whereas the generalized synchronization error is almost constant at various bias voltages after a transient period.

Chapter 10

Summary and Future Work

Two high-dimensional dynamical systems have been presented in this thesis, coupled erbium doped fiber ring lasers and a spatial light modulator with optoelectronic feedback. Depending on the complexity of the system and the type of coupling, each system displayed a different type of synchronization. The methods that were developed to analyze the synchronization in these systems can be applied to other coupled high-dimensional dynamical systems.

10.1   Fiber Ring Lasers

Weakly mutually coupled erbium doped fiber ring lasers provide a means to study a dynamical system with a very large number of degrees of freedom. Once the coupling between the lasers was initiated, the changes in the optical spectra were characterized as a function of the detuning. The synchronization error was studied as a function of coupling strength, and a threshold for synchronization was determined. However, through traditional chaotic time series analysis, i.e., the calculation of the average synchronization error, a leader and follower laser could not be determined. Several methods for the determination of leader and follower laser were tested. The first method was the calculation of a running synchronization error, where the synchronization error was averaged over each round trip, rather than over the entire time series. This did not provide conclusive evidence for a leader and follower laser or a way to detect switches in which laser was leading. Though the synchronization error averaged over each round trip did not produce conclusive evidence

of a leader and follower laser, the switches could be extracted from its derivatives.

Since the intracavity dynamics of the ring laser can be resolved and recorded, we are able to reshape the one dimensional intensity-time series into a two-dimensional plot. With this spatiotemporal time series, we are able to use subtraction with offsets corresponding to each laser leading the dynamics and we are able to determine the leader and follower laser, as well as determine where the lasers switch roles as leader and follower.

We are able to perform a decomposition of these spatiotemporal time series into an orthogonal basis of intrinsic modes using Karhunen-Loeve decomposition. With this method, we are able to extract the most energetic modes of each laser. From the K-L analysis of the spatiotemporal subtraction data, and the leader and follower laser as well as the role switches were able to be determined.

A delay-differential equation model was develop based on the Maxwell-Bloch equations for the weakly coupled fiber ring laser system. The model showed similar dynamics as the experiment as well as a similar threshold for synchronization. A leader and follower laser were not able to be determined using the synchronization error averaged over the entire time series. The numerical simulation data was represented in the same spatiotemporal fashion as the experiment and leader and follower lasers were evident as were role switches.

The mutually coupled EDFRL's were configured in several chaotic communications schemes. In the first, bits were injected directly into one of the ring cavities, both numerically and experimentally. Bits were able to be recovered through simple subtraction of the synchronized receiver signal from the transmitted signal. However, it took several round trips before the bits that were injected into the cavity were no long visible in the transmitter's intensity time series. This ring down was characterized as a function of the

difference between the injection wavelength and the center lasing wavelength.

In order to eliminate the ring down, the bits were then injected into the coupling line and masked by the chaos of the transmitter laser. The experimental setup was modified so that there was only a single coupling line. Therefore, the electric fields of both lasers were traveling in opposite directions down a single piece of optical fiber. This did not affect synchronization between the two lasers. The injection of the bits into the coupling line eliminated the ring down, but the bit amplitude had to be significantly smaller in order to be masked by the chaos because the amplitude of the light in the injection line is 70% less than it is in the ring cavity. However, bits were recovered in both the experiment and simulations in this injection scheme.

10.2   Spatial Light Modulator

A spatial light modulator was investigated as a dynamic holographic grating. Several different laser intensity patterns were created from a single Gaussian beam, including multiple Gaussian beams in patterns, optical holographic billiards, and Bessel beams. The Gaussian profile beams can be used as optical tweezers to trap charged particles and atoms in a point on a plane. Possible applications of the holographic billiards is the confinement of Bose-Einstein condensates. The Bessel beams are used as all light atom guides[32].

When configured in an optoelectronic feedback loop, the SLM displays spatiotemporal chaos. This chaos was characterized and it was found that the average grain size and speed with which the pattern changes depends on the bias voltage. The auxiliary method was used to detect generalized synchronization in this system when the closed loop drive movie was fed multiple times into the system in an open loop configuration with different

initial conditions. The transients to synchronization were calculated as a function of the bias voltage, and it was found that the synchronization error of the responses after the transients was independent of bias voltage.

10.3   Applications and Future Work

The holographic images created with the SLM have applications to atomic physics and the origins of chaos and Brownian motion. Using the holographic billiards and a Bose-Einstein condensate (BEC) with an initial momentum, one should be able to track the BEC as it collides with the walls. Since the billiards can be made in the shape of a stadium, it should be possible to view a BEC in a chaotic trajectory. By tracking the BEC, one should be able to observe Brownian motion and possibly see the microscopic origins of chaos[87].

The Bessel beams are already being used to guide atoms. Work is ongoing in the laboratory of Dr. Wendell T. Hill, III, to guide atoms into magneto-optic atom traps using these beams, and to guide the Bessel beams down hollow core optical fiber in order to create a fiber optic atom guide. The evidence for the first atoms guided through these holographic Bessel beams in the Hill laboratory can be found in Ref. [32].

The K-L decomposition used to determine leader/follower laser and role switching in the coupled fiber ring lasers may have more fundamental applications in the analysis of high-dimensional dynamics. Future work on the mutually coupled EDFRL's includes a study of the synchronization of the modes as a function of the coupling strength. This could lend tremendous insight into whether synchronization occurs in the low frequency modes first and modes synchronize from low frequency to high frequency with increasing coupling strength, or whether the high frequency modes synchronize first and the opposite occurs. Through K-L decomposition, we may be able to determine whether this also

applies to high-dimensional systems such as fiber ring lasers.

The SLM configured in an optoelectronic loop can be thought of as a system of oscillators connected through the feedback. Through the use of an field programmable gate array, it should be possible to control the connections between the oscillators, or nodes, and create a very large network. The connections between the nodes can be made in a static, dynamic, or stochastic fashion. A network of this kind would allow for the exploration of a very wide parameter space. Once data is collected on this network, it may be analyzed using K-L decomposition. If the systems possess enough coherence, K-L analysis may be used to find a series of coupled ordinary differential equations to model the most important dynamics in the network. In principle, this model should be more computationally tractable than a model of the entire network.

BIBLIOGRAPHY

[1] U. Frisch, *Turbulence: The Legacy of A.N. Kolmogorov*, (Cambridge University Press, Camebridge, UK, 1995).

[2] E.W. Justh and P.S. Krishnaprasad, Pattern-Forming Systems for Control of Large Arrays of Actuators, *J. Nonlinear Sci.*, **11**: 239-77, (2001).

[3] L.S. Liebovitch and I.B. Schwartz, Migration Induced Epidemics: Dynamics of Flux Based Multipatch Models,

[4] A. Uchida, R. McAllister, R. Meucci, R. Roy, Generalized Synchronization of Chaos in Identical Systems with Hidden Degrees of Freedom, *Phys. Rev. Lett.*, **91**(17): 174101, (2003).

[5] H.D.I. Abarbanel, M.B. Kennel, M. Buhl, and C.T. Lewis, Chaotic dynamics in erbium-diped fiber ring lasers, *Phys. Rev. A*, **60**(3): 2360-74, (1999).

[6] D.S. Morgan and I.B. Schwartz, Karhunen-Loeve mode control of chaos in a reaction-diffusion process, *Ohys. Rev. E*, **11**: 204, (1997).

[7] I. Triandaf and I.B. Schwartz, Karhunen-Loeve mode control of chaos in a reaction-diffusion process, *Phys. Rev. E*, **56**(1): 204-12, (1997).

[8] A. Pikovsky, M. Rosenblum and J. Kurths, *Synchronization: A Universal Concept in Nonlinear Science* (Cambridge University Press, Cambridge, UK, 2001), Chap. 1,10.

[9] E. Ott, *Chaos in Dynamical Systems, 2nd Ed.*, (Cambridge Univerisy Press, Cambridge, UK, 2002).

[10] S.H. Strogatz, *Nonlinear Dynamics and Chaos*, (Perseus Books, Cambridge, MA, 1994).

[11] L.M. Pecora, T.L. Carroll, G.A. Johnson, D.J. Mar and J.F. Heagy, Fundamentals of Synchronization in Chaotic Systems: Concepts and Applications, *Chaos*, **7**(4): 520-43, (1997).

[12] T. Yanada and H. Fujisaka, Stability Theory of Synchronized Motion in Coupled Oscillator Systems, II, *Progress Theor. Phys*, **70**: 1240, (1983).

[13] V.S. Afraimovich, N.N. Verichev and M.I. Rabinovich, Stochastic Synchronization of Oscillators in Dissipative Systems, *Inv.VUZ Radiofiz*, **29**: 795, (1986).

[14] L.M. Pecora and T.L. Carroll, Synchronization in Chaotic Systems, *Phys. Rev. Lett.*, **64**(8): 821-4, (1990).

[15] Private communication with Atsushi Uchida.

[16] H.D.I. Abarbanel, N.F. Rulkov and M.M. Sushchik, Generalized synchronization of chaos, The auxiliary system approach, *Phys. Rev. E*, **53**(5): 4528-35, (1996).

[17] L. Kocarev and U. Parlitz, Generalized Synchronization, Predictability, and Equivalence of Unidirectionally Coupled Dynamical Systems, *Phys. Rev. Lett.*, **76**(11): 1816-19, (1996).

[18] K. Pyragas, Weak and strong synchronization of chaos, *Phys. Rev. E*, **54**(5): R4508-11, (1996).

[19] D.Y. Tang, R. Dykstra, M.W. Hamilton, and N.R. Heckenberg, Observation of generalized synchronization of chaos in a driven chaotic system, *Phys. Rev. E*, **57**(5): 5247-51, (1998).

[20] K.M. Cuomo and A.V. Oppenheim, Circuit Implementation of Synchronized Chaos with Applications to Communications, *Phys. Rev. Lett*, **71**(1): 65-8, (1993).

[21] H.D.I. Abarbanel, *Analysis of Observed Chaotic Data* (Springer-Verlag, New York, NY, 1996).

[22] B.E.A. Saleh and M.C. Teich, *Fundamentals of Photonics* (John Wiley and Sons, New York, NY, 1991).

[23] O. Svelto, *Principles of Lasers, 4th Ed.* (Plenum Press, New York, NY, 1998).

[24] R. Loudon, *The Quantum Theory of Light, 3rd Ed.* (Oxford University Press, New York, NY, 1973), Chap. 1.

[25] C.C. Davis, *Lasers and Electro-optics: Fundamentals and Engineering* (Cambridge Universiy Press, New York, NY, 1996), Chap. 16.

[26] J. Durnin, Exact solutions for nondiffracting beams. I. The scalar theory. *J. Opt. Soc. Am. A*, **4**(4):651-4, (1987).

[27] A. Vasara, J. Turunen, and A.T. Friberg, Realization of general nondiffracting beams with computer-generated holograms, *J. Opt. Soc. Am. A*, **6**(11):1748-54, (1989).

[28] A. Papoulis, *Systems and Transforms with Applications in Optics* (McGraw-Hill, New York, NY, 1968), Chap. 7.

[29] J.W. Goodman, *Introduction to Fourier Optics, 2nd Ed.* (McGraw-Hill, New York, NY, 1996), Chap 7,9.

[30] J.E. Curtis, B.A. Koss, and D.G. Grier, Dynamic holographic optical tweezers, *Opt. Comm.*, **207**:169-175, (2002).

[31] S. Bergamini, B. Darquie, M. Jones, L. Jacubowiez, A. Browaeys, and P. Grangier, Holographic generation of microtrap arrays for single atoms by use of a programmable phase modulator, *J. Opt. Soc. Am. B.*, **21**(11):1889, (2004).

[32] N. Chattrapiban, E.A. Rogers, I.V. Arakelyan, R. Roy, and W.T. Hill, III, Laser beams with embedded vortices: Tools for atom optics, submitted to *J. Opt. Soc. Am. B*, (2005).

[33] I.C. Khoo and S.T. Wu, *Optics and Nonlinear Optics of Liquid Crystals* (World Scientific Publishing, River Edge, NJ, 1993) Chaps. 1,2.

[34] Hamamatsu PAL-SLM X7550 Instruction Manual.

[35] Private Communication with Hamamatsu Corporation.

[36] G. D'Alessandro and W. K. Firth, Hexagonal spatial patterns for a Kerr slice with a feedback mirror, *Phys. Rev. A*, **46**(1):537, (1992).

[37] R. Neubecker, G. L. Oppo, B. Thuering, and T. Tschudi, Patter Formation in a liquid-crystal light valve with feedback, including polarization, saturation, and internal threshold effects, *Phys. Rev. A*, **52**(1): 791, (1995).

[38] B. Thuring , R. Neubecker and T. Tschudi, Transverse pattern formation in liquid crystal light valve system, *Opt. Comm.*, **102**: 111-115, (1993).

[39] M. A. Vorontsov, J. C. Ricklin, and G. W. Carhart, Optical simulation of phase-distorted imaging systems: nonlinear and adaptive optics approach, *Opt. Eng.*, **34**: 3229, (1995);

[40] P. L. Ramazza, S. Ducci, S. Boccaletti, and F. T. Arecchi, Localized versus delocalized patterns in a nonlinear optical interferometer, *L. Opt. B: Quant. Semiclass. Opt.*, **2**: 399, (2000).

[41] Private Communications with R. Neubecker

[42] A. Ashkin, J.M. Dziedzic, J.E. Bjorkholm, and S. Chu, Observation of a single-beam gradient force optical trap for dielectric particles, *Opt. Lett.*, **11**:247, (1986).

[43] M. Reicherter, T. Haist, E.U. Wagemann, and H.J. Tiziani, Optical particle trapping with computer-generated holograms written on a liquid crystal display, *Opt. Lett.*, **24**(9):608-10, (1999).

[44] J. Leisener, M. Reicherter, T. Haist, and H. J. Tiziani, Multi-functional optical tweezers using computer-generated holograms, *Opt. Comm*, **185**: 77, (2000).

[45] N.R. Heckenberg, R. McDuff, C.P. Smith, H. Rubinsztein-Dunlop, M.J. Wegner, Laser beams with phase singularities, *Optical and Quantum Electronics*, **24**: S951-62, (1992).

[46] Private Communication with Andrew Pomerance and Jennifer Curtis.

[47] J.R. Fineup, Phase retrieval algorithms: a comparison, *Applied Optics*, **21**(15): 2758-69, (1982).

[48] W.O. Saxton, *Computer Techniques for Image Processing in Electron Microscopy* (Academic Press, New York, NY, 1978), Chap 6.

[49] H. Akahori and Y. Seki, Estimation of a Phase-Recording Characteristic of System for Synthesizing a Kinoform, *Elec. and Comm. in Jap. Part 2*, **76**(9): 223-39, (1993).

[50] N. Chattrapiban, E.A. Rogers, D. Cofield, W.T. Hill, III, and R. Roy, Generation of nondiffracting Bessel beams by use of a spatial light modulator, *Opt. Lett*, **28**(22): 2183-85, (2003).

[51] M. S. Soskin, V. N. Gorshkov, M. V. Vasnetsov, J. T. Malos, and N. R. Heckenberg, Topological charge and angular momentum of light beams carrying optical vortices, *Phys. Rev. A* , **56**: 4064-4075 (1997).

[52] G.D. Vanwiggeren and R. Roy, Chaotic Communication using Time-Delayed Optical Systems, *Int. Journ. Bif. Chaos*, **9**(11): 2129-56, (1998).

[53] G.D. Vanwiggeren and R. Roy, Optical Communication with Chaotic Waveforms, *Phys. Rev. Lett.*, **81**(16): 3547-50, (1998).

[54] G.D. Vanwiggeren, *Chaotic Communication with Erbium-Doped Fiber Ring Lasers*, Ph.D. Thesis, Georgia Institute of Technology, (2000).

[55] G.D. VanWiggeren and R. Roy, Communication with dynamically fluctuating states of light polarization, *Phys. Rev. Lett.*, **88**: 097903-1-4, (2002).

[56] G.P. Agrawal, *Fiber Optic Communication Systems, 2nd Ed.*, (John-Wiley & Sons, Inc., New York, NY, 1997).

[57] G. Keiser, *Optical Fiber Communications, 3rd Ed.*, (McGraw-Hill, Boston, MA, 2000).

[58] G. P. Agrawal, *Nonlinear Fiber Optics, 2nd Ed.*, (Academic Press, San Diego, CA, 1995).

[59] G.D. VanWiggeren and R. Roy, Transmission of linearly polarized light through a single-mode fiber with random fluctuations of birefringence, *App. Opt.*, **38**(18): 3888-92, (1999).

[60] E. Desurvire, *Erbium Doped Fiber Amplifiers: Principles and Applications*, (John-Wiley & Sons, Inc., New York, NY, 1994).

[61] Quinton L. Williams, *Fast Temporal Dynamics of the Erbium-Doped Fiber Ring Laser*, Ph.D. Thesis, Georgia Institute of Technology, 1992.

[62] D.J. Deshazer, *Synchronization of Chaotic Lasers*, Ph.D. Thesis, University of Maryland, College Park, 2002.

[63] J. Garcia-Ojalvo and R. Roy, Intracavity chaotic dynamics in ring lasers with an injected signal, *Phys. Rev. A*, **229**: 362-66, (1997).

[64] Q.L. Williams, J. Garcia-Ojalvo, and R. Roy, Fast intracavity polarization dynamics of an erbium-doped fiber ring laser: Inclusion of stochastic effects, *Phys. Rev. A*, **55**(3): 2376-86, (1999).

[65] D.J. DeShazer, J. Garcia-Ojalvo, and R. Roy, Bursting Dynamics of a fiber laser with an injected signal, *Phys. Rev. E*, **67**(3): 36602, (2003).

[66] C.T. Lewis, H.D.I. Abarbanel, M.B. Kennel, M. Buhl, and L. Illing, Synchronization of chaotic oscillations in doped fiber ring lasers, *Phys. Rev. E*, **63**: 016215, 2000.

[67] T. Schreiber, Measuring Information Transfer, *Phys. Rev. Lett.*, **85**(2): 461-4, (2000).

[68] D. Merbach, O. Hess, H. Herzel and E. Scholl, Injection-induced bifurcations of transverse spatiotemporal patterns in semiconductor laser arrays, *Phys. Rev. E*, **52**(2): 1571-8, (1995).

[69] H.D.I. Abarbanel, M.B. Kennel, Synchronizing High-Dimensional Chaotic Optical Ring Dynamics, *Phys. Rev. Lett.*, **80**(14): 3153-6, (1998).

[70] H. Kantz and T. Schreiber, *Nonlinear Time Series Analysis* (Cambridge University Press, Cambridge, UK, 1997), Chap. 14.

[71] F.T. Arecchi, G. Giacomelli, A. Lapucci, and R. Meucci, Two-dimensional representation of a delayed dynamical system, *Phys. Rev. A*, **45**(7): 4225-8, (1992).

[72] E.A. Rogers, J. Garcia-Ojalvo, D.J. DeShazer, and Rajarshi Roy, Spatiotemporal Representation of High Dimensional Dynamics: Synchronization and Symmetry Breaking in Mutually Coupled Fiber Ring Lasers, submitted to *Phys. Rev. Lett.*, (2005).

[73] T. Heil, I. Fischer, W. Ealsser, J. Mulet, C.R. Mirasso, Chaos Synchronization and Spontaneous Symmetry-Breaking in Symmetrically Delay-Coupled Semiconductor Lasers, *Phys. Rev. Lett.*, **86**(5): 795-8, (2001).

[74] K. Ikeda, Multiple-valued stationary state and its instability of the transmitted light by a ring cavity system, *Opt. Comm.*, **30**(2): 257-61, (1979).

[75] K. Ikeda, H. Daido, and O. Akimoto, Optical Turbulence: Chaotic Behavior of Transmitted Light from a Ring Cavity, *Phys. Rev. Lett.*, **45**: 709, (1980).

[76] W.H. Loh and C.L. Tang, Numerical Investigation of Ultrahigh Frequency Polarization Self-Modulation in Semiconductor Lasers, *IEEE Journ. Quant. Elect.*, **27**(3):389:95, (1991).

[77] A. Yariv, *Quantum Electronics, 3rd Ed.* (John-Wiley & Sons, New York, NY, 1967), Chap. 8.

[78] J. Garcia-Ojalvo and R. Roy, Noise amplification in a stochastic Ikeda model, **224**(1): 51-6, (1996).

[79] E.A. Rogers, A.B. Cohen, and R. Roy, Communication with mutually coupled synchronized fiber ring lasers. In preparation.

[80] *This is Spinal Tap*, Director R. Reiner, producer K. Murphy, writers C. Guest, M. McKean, H. Shearer, and R. Reiner, Embassy Pictures, (1984).

[81] R. Brown, Approximating the Mapping between Systems Exhibiting Generalized Synchronization, *Phys. Rev. Lett*, **81**(22): 4835, (1998).

[82] J. Arnhold, P. Grassberger, K. Lehnertz, C.E. Elger, A robust method for detecting interdependences: application to intracranially recorded EEG, *Physica D*, **134**: 419-30, (1999).

[83] C.L. Goodridge, L.M. Pecora, T.L. Carroll, and F. J. Rachford, Detecting functional relationships between simultaneous time series, *Phys. Rev. E*, **64**: 026221, (2001).

[84] V. Afraimovich, A. Cordonet, and N.F. Rulkov, Generalized synchronization of non-invertible maps, *Phys. Rev. E*, **66**: 016208, (2002).

[85] B.R. Hunt, E. Ott, J.A. Yorke, Differentiable generalized synchronization of chaos, *Phys. Rev. E*, **55**(4): 4029-34, (1997).

[86] E.A. Rogers, R. Kalra, R.D. Schroll, A. Uchida, D.P. Lathrop, and R. Roy, Generalized synchronization of spatiotemporal chaos in a liquid crystal spatial light modulator, *Phys. Rev. Lett.*, **93**(8): 084101, (2004).

[87] P. Gaspard, M.E. Briggs, M.K. Francis, J.V. Sengers, R.W. Gammon, J.R. Dorfman, and R. V. Calabrese, Experimental evidence for microscopic chaos, *Nature*, **394**: 865-8, (1998).